

# **Materials behavior under dynamic shock loading using high power lasers**

*By*

**VINAY RASTOGI**

**Enrolment No. PHYS01201204019**

**Bhabha Atomic Research Centre, Mumbai, India**

*A thesis submitted to the*

*Board of Studies in Physical Sciences*

*In partial fulfillment of requirements*

*for the Degree of*

**DOCTOR OF PHILOSOPHY**

*of*

**HOMI BHABHA NATIONAL INSTITUTE**



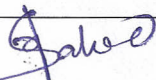
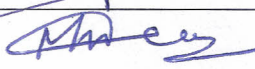
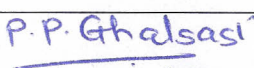
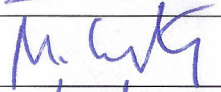
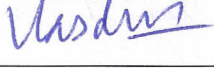
**May, 2018**



# Homi Bhabha National Institute<sup>1</sup>

## Recommendations of the Viva Voce Committee

As members of the Viva Voice Committee, we certify that we have read the dissertation prepared by Vinay Rastogi entitled Materials behavior under dynamic shock loading using high power lasers and recommend that it may be accepted as fulfilling the thesis requirement for the award of Degree of Doctor of Philosophy.

Chairman – Dr. N. K. Sahoo		Date: 28/5/18
Guide / Convener – Dr. M. N. Deo		Date: 28/05/2018
Examiner - Prof. Pallavi Ghalsasi		Date: 28/5/18
Member 1- Dr. M. Krishnamurthy		Date:
Member 2- Dr. Vas Dev		Date: 28/5/18
Technology Advisor- Dr. S. Chaurasia		Date: 28/5/18

Final approval and acceptance of this thesis is contingent upon the candidate's submission of the final copies of the thesis to HBNI.

I/We hereby certify that I/we have read this thesis prepared under my/our direction and recommend that it may be accepted as fulfilling the thesis requirement.

Date: 28/05/18

Place: Mumbai



<Signature>

Guide

<sup>1</sup> This page is to be included only for final submission after successful completion of viva voce.



## **STATEMENT BY AUTHOR**

This dissertation has been submitted in partial fulfillment of requirements for an advanced degree at Homi Bhabha National Institute (HBNI) and is deposited in the Library to be made available to borrowers under rules of the HBNI.

Brief quotations from this dissertation are allowable without special permission, provided that accurate acknowledgement of source is made. Requests for permission for extended quotation from or reproduction of this manuscript in whole or in part may be granted by the Competent Authority of HBNI when in his or her judgment the proposed use of the material is in the interests of scholarship. In all other instances, however, permission must be obtained from the author.

(Vinay Rastogi)



## **DECLARATION**

I, hereby declare that the investigation presented in the thesis has been carried out by me. The work is original and has not been submitted earlier as a whole or in part for a degree /diploma at this or any other Institution /University.

(Vinay Rastogi)



## List of Publications

### In Refereed Journals:

#### Related to Thesis

1. Time resolved Raman spectroscopy of polytetrafluoroethylene under laser shock compression.

**Vinay Rastogi**, Usha Rao, S. Chaurasia, C. D. Sijoy, V. Mishra, S. Chaturvedi and M. N. Deo

*Appl. Spec. 71 (2017) 2643-2652*

2. In-situ Raman spectroscopic studies of poly-vinyl-toluene under laser-driven shock compression and comparison with hydrostatic experiments

**Vinay Rastogi**, S. Chaurasia, U. Rao, C. D. Sijoy, H. K. Poswal, V. Mishra, M. Kumar and M. N.

Deo

*Journal of Raman Spectroscopy 48 (2017) 1300-1306*

3. Time-resolved Raman spectroscopy of polystyrene under laser driven shock compression

**Vinay Rastogi**, S. Chaurasia, Usha Rao, C. D. Sijoy, V. Mishra, M. Kumar, S. Chaturvedi and M.

N. Deo

*Journal of Raman Spectroscopy 48 (2017) 1007-1012*

4. Laser Induced Damage Studies in Borosilicate Glass Using nanosecond and sub nanosecond pulses

**Vinay Rastogi**, S. Chaurasia, D. S. Munda

*Journal of Non-Crystalline Solids 463 (2017) 138–147*

5. Raman spectroscopy of laser shocked polystyrene.

**Vinay Rastogi**, S. Chaurasia, U. Rao, C. D. Sijoy, V. Mishra, M. Kumar, M. N. Deo, S.

Chaturvedi and S. M. Sharma

*Journal of Raman Spectroscopy 48 (2017) 458-464.*

6. Development of in situ time-resolved Raman Spectroscopy facility for dynamic shock loading in materials

S. Chaurasia, **Vinay Rastogi**, Usha Rao, M. N. Deo.

*Journal of Instrumentation 12 (2017) P11008*

7. Raman Spectroscopy of Poly (Methyl Methacrylate) under laser shock compression

**Vinay Rastogi**, S. Chaurasia, C. D. Sijoy, V. Mishra, M. Kumar, S. Chaturvedi and M. N. Deo.

*(Manuscript under Preparation)*

### **Publications other than thesis:**

1. In situ measurement of ions parameters of laser produced ion source using high resolution Thomson Parabola Spectrometer.

S. Chaurasia, C. Kaur, **V. Rastogi**, A. K. Poswal, D. S. Munda, R. K. Bhatia and V. Nataraju.

*Journal of Instrumentation 11, August 2016.*

2. Nanosecond time resolved vibrational spectroscopy of laser shocked polyethylene

**Vinay Rastogi**, S. Chaurasia, C. D. Sijoy, V. Mishra, M. Kumar, S. Chaturvedi and M. N. Deo. *(Manuscript under Preparation)*

### **In Conference Proceedings/News Letters:**

#### **Related to thesis**

1. High pressure Raman study polyvinyl-toluene (PVT)

**Vinay Rastogi**, Usha Rao, S. Chaurasia, H. K. Poswal, Manmohan Kumar and S. M. Sharma

*54th European High Pressure Research Group Meeting Bayreuth, Germany (2016)*

2. Pump probe based Raman spectroscopic studies of PTFE under laser driven shock compression.

**Vinay Rastogi**, Usha Rao, S. Chaurasia, A. K. Mishra, H. K. Poswal, M. N. Deo and S. M. Sharma

*AIP Conf. Proc. 1731, 060025 (2016).*

3. Vibrational spectroscopy of polyvinyl-toluene under laser- driven shock compression

**V. Rastogi**, U. Rao, S. Chaurasia, H. K. Poswal, M. Kumar, M. N. Deo, S. M. Sharma

*34th European Conference on Laser Interaction with Matter (ECLIM 2016) Moscow, Russia.*

4. Vibrational Spectroscopy of Aromatic Scintillating Polymer under Laser-Driven Shock Compression

**Vinay Rastogi**, S. Chaurasia, Usha Rao, C. D. Sijoy, V. Mishra, Manmohan Kumar, S. Chaturvedi, Surinder M. Sharma

*6th International Conference on Perspectives in Vibrational Spectroscopy, 5-8 November 2016, Lucknow, India.*

5. Laser shocked high pressure and time resolved Raman spectroscopy of Polystyrene

**Vinay Rastogi**, Usha Rao, S. Chaurasia, Manmohan Kumar, M. N. Deo and Surinder M. Sharma.

*DAE-BRNS Symposium on Condensed Matter Physics under Extreme Conditions (CoMPEC 2016).*

6. Spectroscopic studies of polytetrafluoroethylene under laser driven shock compression.

**Vinay Rastogi**, Usha Rao, S. Chaurasia, M. N. Deo and S. M. Sharma.

*International conference on Photons: Multiple and creative solutions to challenges (ICPMCSC) Ratnam College, Mumbai India (2015).*

7. Study of laser induced damage mechanism on the surface of BK7 glass using nanosecond and sub nanosecond pulses.

**Vinay Rastogi**, Channprit Kaur, P. Leshma, D. S. Munda, S. Chaurasia,

*4th International conference on Current development in Atomic, Molecular, Optical & Nanophysics with applications, University of Dehli, Dehli, India (2015).*

8. Facility for Time Resolved Raman Spectroscopy of Materials Under Shocks

*Brief Communication, BARC News Letter, July-August 2015.*

(Vinay Rastogi)

*Dedicated*

*to*

*My Parents*



## Acknowledgements

I would first like to express my sincere gratitude to my guide Dr. M. N. Deo, High Pressure & Synchrotron Radiation Physics Division (HP&SRPD), Bhabha Atomic Research Centre (BARC), for his guidance, constant support, motivation, constructive criticism and valuable advices. I am very pleased to express my gratitude to my technical advisor Dr. S. Chaurasia, HP&SRPD, BARC, for his invaluable guidance and supervision during course of the thesis. He encouraged me to develop a better understanding of the field of laser plasma interaction, fundamental of shock physics and setting up the experiments. His guidance helped me in all the time of research and writing of this thesis. During tough times and whenever I stuck in any way, he was always besides me.

I am also very grateful to Honorable Dr. R. Chidambaram, Principal scientific advisor, Government of India and Honorable Dr. S. K. Sikka, Scientific advisor to PSA, for assigning us the project to develop the time resolved Raman spectroscopy (TRRS) experimental facility for the dynamically shocked material at HP&SRPD, BARC. Their personal interest and guidance has led us in the successful development of the TRRS facility.

My sincere thanks to Dr. S. M. Sharma, Former Director Physics Group, BARC, for his continuous support and moral encouragement throughout this journey. He always managed to spare his time amidst of his very busy schedule to review my work. He used to visit the laboratory time to time to see the progress on the development of the experimental facility and the main experiments. His fruitful suggestions, expertise and interest always motivate us to do better. I have learnt a lot from him.

Along with my Guide and technical advisor, I would like to thank the rest of my doctoral committee members: Chairman of the committee Dr. N. K. Sahoo (Head HP&SRPD and AD

Physics Group), Prof. M. Krishnamurthy (external committee member, TIFR Hyderabad) and Dr. Vas Dev (L&PTD, BARC), for their insightful suggestions, constructive criticism and encouraging comments during the course. The suggestions are also very helpful from various perspectives in understanding the research subject.

I also wish to thank Dr. C. D. Sijoy and Dr. Vinayak Mishra for simulation results and many fruitful discussions during the course of the thesis. My thanks are also attributable to Dr. Himanshu Poswal, Dr. Ajay Kumar Mishra and Dr. K. K. Pandey HP&SRPD, BARC for their help in carrying out static compression experiments and measurements. Thanks are due to Dr. Ashwini Poswal for useful scientific discussions.

Special thanks to Dr. Manmohan Kumar, RPCD, BARC for providing us the polymeric samples for the shock compression experiments. He always manages his time in spite of his busy schedule to review my work and improve the quality of the work. He is always ready to help me in spite of his prior engagements.

I would like to thank Dr. Himal Bhatt, HP&SRPD, BARC and Dr. Rajib Kar, L&PTD, BARC for their precious support at various occasions. They are such a charming, inspiring and cheerful person and always ready to help me whenever I needed them.

Very special thanks to Dr. C. S. Prabhakar, Assistant Prof. at Bihar Agricultural University, Sabour, a wonderful person; he always stood by my side like an elder brother during the tough times. He always keeps pushing me to do work hard.

I am immensely thankful to Mr. Diwakar S. Munda and Mr. Ritesh S. Sabale HP&SRPD, BARC for helping me in instrumentation and technical assistance in all of my experiments. I am also thankful to Mr. Milind (L&PTD, BARC) and his colleagues, for their help on several occasions in making the mechanical parts for the experimental facility.

I am also very thankful to Mrs. P. Leshma, Mr. C. G. Murali, Ms. Channprit Kaur, Mr. Shiv Kumar Mr. Romesh Chandra, Mr. Swayam Keshri, Mr. Subodh Sahoo, Mr. Girish and Ms. Meera Varma who directly or indirectly have helped me in achieving my goals. Special thanks to Ms. Usha Rao, for helping me in all my experiments and stimulating discussions.

I thank to all my fellow mates for their moral encouragements, support and stimulating discussions. My seniors Dr. Rohit Singh Chauhan, Dr. Lokesh Gambhir, Dr. Pankaj kandwal, Dr. Sumit Chillar, Dr. Arvind Kumar, Dr. Debesh Ray, Dr. Naveen Kumar and Dr. Sumit Mehan are always with me during this journey. Their continuous guidance has teaches me a lot. I am also thankful to my friend and roommate Dr. Nitendra Singh, a very hard working person who is able to transmit his passion for work and scientific research in others, for guiding me on several occasions. His passion for work and research is always an inspiration for me. I would also be thankful to my friends Sandeep Joshi, Suryakant Gautam, Prashant Chaudhary, Satish Kumar Verma, Ravi Dhawan, Shankar Rao Chapa, Anuj Sharma, Vinod Belwanshi, Sunil Kumar, Tribeni Roy, Ganesh Maurya, Somnath Chaterji, Abhishek Kaushik, Harshit Jain, Sahar Arjmand, Sapna Singh, Sakshi Mukhija, Paridhi Goel, Rakesh, Sai Rajgopal, Akash, Dr. Ashwani Kumar, Vinit Bajpayee for being always ready to help me.

I would also like to thanks HP&SRPD office staff members, especially Mrs. Modita and Mrs. Megha, for their constant cooperation in all administrative activities related to my PhD.

Last but not the least; I would like to thank my parents and all the family members for being supportive in my endeavor and extending encouragement throughout the work.



# Table of Contents

<b>SYNOPSIS</b> .....	xx
<b>List of Figures</b> .....	xxvii
<b>List of Tables</b> .....	xxxv
<b>Chapter 1. Introduction</b> .....	1
1.1. Shock Waves.....	3
1.2. Shock characterization: Principal Hugoniot .....	6
1.3. Impedance Mismatch technique .....	8
1.4. Practical uses of Impedance Mismatch technique .....	8
1.5. $P-u_P$ curves for materials with $U_s = A + bu_P$ .....	9
1.6. $P-u_P$ diagram for a shock crossing a boundary into a material of higher impedance .....	10
1.7. Rules for impedance matching.....	11
1.8. Impedance matching for four basic cases .....	11
1.9. Physical Properties of Polymers .....	13
1.10. Polymers configuration and conformations .....	13
1.11. Crystalline and Amorphous Polymers .....	17
1.12. Fundamental of Raman Spectroscopy .....	21
1.13. Motivation for the present work .....	27
<b>Chapter 2. Development of in situ time-resolved Raman spectroscopy facility for dynamic shock loading in materials</b> .....	29
2.1. Introduction.....	29

2.2. Laser system for pump and probe beam .....	29
2.2.1. Characterization of laser parameters.....	30
2.3. Confinement geometry target assembly.....	32
2.4. Detection System .....	34
2.5. Static high pressure Measurement .....	36
2.6. Experimental arrangement for time resolved Raman spectroscopy.....	37
2.7. Summary... ..	40
<b>Chapter 3. Investigation of damage mechanism in optical glasses used for making confinement geometry targets.....</b>	<b>42</b>
3.1. Introduction.....	42
3.2. Damage threshold .....	43
3.3. Causes of laser induced damaged phenomena.....	43
3.4. Experimental detail .....	44
3.5. Results and Discussions.....	45
3.5.1. Surface damage investigation .....	45
3.5.2. Damage threshold and thermal effect studies of BK7 and its dependency on pulse duration.....	46
3.5.3. Damage threshold dependency on wavelength.....	48
3.5.4. Effect of convection on glass damage using N <sub>2</sub> gas flow.....	50
3.5.5. Effect of incident Laser energy and number of pulses on damaged area .....	53

3.5.6. Damaged Surface Morphology .....	56
3.5.7. Laser transmission through BK7 glass .....	58
3.5.8. Study of micro structural modifications in Borosilicate glass by laser irradiation using offline Raman spectroscopy .....	60
3.5.9. Optical Spectroscopy for plasma temperature and density calculation .....	61
3.5.10. Plasma Temperature Measurement.....	62
3.5.11. Free electron density Measurement .....	65
3.5.12. Reason for considering plasma in LTE.....	66
3.6. Summary and Conclusions .....	67
<b>Chapter 4. Raman Spectroscopic analysis of Aromatic plastic scintillating polymers under Laser driven Shock Compression.....</b>	<b>69</b>
4.1. Introduction.....	69
4.2. Synthesis and characterization of Polystyrene and PVT .....	70
4.2.1. Polystyrene.....	70
4.2.2. Poly vinyl toluene .....	71
4.3. Shock pressure estimation.....	72
4.3.1. Shock pressure estimation inside polystyrene .....	72
4.3.2. Shock pressure estimation inside PVT .....	74
4.4. Grüneisen parameter and bond anharmonicities .....	74
4.5. Results and Discussion .....	76

4.5.1. Vibrational spectroscopy of polystyrene and PVT under shock compression .....	76
4.5.1.1. Spectroscopic analysis of Polystyrene under shock compression .....	76
4.5.1.2. Pressure dependent Raman line width .....	82
4.5.2. Spectroscopic analysis of PVT under shock compression .....	83
4.5.3. Density independent Grüneisen parameter and bond anharmonicities analysis .....	88
4.5.3.1. Density independent Grüneisen parameters for local modes of polystyrene.....	88
4.5.3.2. Density independent Grüneisen parameters for local modes of PVT .....	90
4.5.4. Time resolved studies of polystyrene and PVT under Shock compression .....	92
4.5.4.1. Time resolved studies of polystyrene under Shock compression .....	92
4.5.4.2. Shock Velocity calculation inside Polystyrene.....	96
4.5.4.3. Time resolved studies of PVT under Shock compression .....	97
4.6. Conclusions.....	99
<b>Chapter 5. High pressure and time resolve Raman spectroscopy of polytetra-</b>	
<b>fluoroethylene (PTFE/Teflon).....</b>	<b>101</b>
5.1. Introduction.....	101
5.2. Shock Pressure calculation .....	103
5.3. Results.....	104
5.3.1. Spectroscopic analysis of PTFE under static compression.....	105
5.3.2. Spectroscopic analysis of PTFE under shock compression .....	107

5.3.3. Time resolved Raman measurement of CF <sub>2</sub> twisting and CF <sub>2</sub> stretching modes under shock compression.....	110
5.3.4. Shock velocity calculation inside PTFE using 287 and 729 cm <sup>-1</sup> modes .....	113
5.4. Discussion.....	114
5.5. Conclusions.....	117
<b>Chapter 6. Raman Spectroscopy of Poly (Methyl Methacrylate) under laser shock compression.....</b>	<b>119</b>
6.1. Introduction.....	119
6.2. Previous studies on PMMA under static and shock compression .....	120
6.3. Shock pressure determination .....	121
6.4. Shock velocity calculation in PMMA.....	122
6.5. Raman Spectrum of PMMA under ambient conditions.....	124
6.6. Results and Discussion .....	126
6.6.1. Raman measurement of PMMA under shock compression.....	126
6.6.2. Bond associated with C–CO–O–CH <sub>3</sub> group .....	129
6.6.3. Bond associated with C–H deformation modes.....	131
6.6.4. Volume independent Grüneisen Parameter for PMMA.....	132
6.7. Conclusion .....	135
<b>Chapter 7. Summary and Conclusions.....</b>	<b>137</b>
7.1. Future Directions .....	143

**References**..... 144

## SYNOPSIS

Polymers under high pressure have attracted an increase level of interest in recent years, especially under dynamic compression. Polymer chain have covalent bonds holding the atoms in a chain and much weaker bonds such as hydrogen bonding or Vander Waals bonds, holding the different chains in a solid. Due to their complexity and adoption of different conformations, polymeric material exhibits several interesting phenomenon. With the increase in pressure, the semi crystalline polymers can also go solid-solid phase transition. In addition, polymers also have potential application as an energetic material. The interactions of energetic materials and polymers have important implications in safety, long-term storage, and performance of explosives and explosive mixtures. Polymers in contact with explosives are used in a number of ways, e.g. “plastic bonded” explosives, particulate encapsulation of explosives. Various measurement have been performed using technique such as infrared and Raman spectroscopy to examine the materials behavior at molecular level under static compression. In recent years, the time resolved spectroscopy has become an attractive experimental tool for investigating atomic and molecular dynamics of materials under shock loading. The intermolecular and intramolecular interactions can be altered under pressure and monomers may undergo phase transitions. These altered properties may provide new pathways to produce novel properties in polymers that are distinct from conventional synthesis methods. Moreover, it is important for the polymer industries to explore pressure induced polymer products with improved, advanced and distinct properties from that obtained using conventional synthetic methods. Understanding of microscopic behavior of polymers at atomic and molecular level could also be useful in order to specify excitation or relaxation processes of these materials under shock compression. Such studies are also very important to study shock responses of energetic materials. Since Raman

spectroscopy is a powerful means to investigate dynamics of the molecules, molecular structural changes, and bond strength etc., because atomic vibrations are directly monitored. Thus, chemical or structural changes can be detected and give direct information of the initiation and decomposition mechanisms occurring at the molecular levels under shock compression. More extensive studies of polymers under dynamic compression would be very helpful to elucidate the fundamental processes these materials undergo.

The thesis consists of seven chapters. The **chapter 1** gives an introduction to the shock waves, impedance mismatch technique, physical properties of polymers and fundamental science of polymers under extreme conditions. The interest in polymers, their usefulness under extreme conditions and objective of thesis is also discussed.

**Chapter 2** gives brief description about in-house developed time resolved Raman spectroscopy facility. The experimental techniques used to study the polymers of interest under shock loading are also described in this chapter. The chapter starts with a brief description of the nanosecond laser system used in present research work. The characterization of the parameters of the driving laser namely: pulse duration, spatial spectral profile etc. is outlined. Most of the work of this thesis is carried out using time resolved Raman spectroscopy at extreme conditions. Experimental set up for confinement geometry targets, high pressure technique including pressure calibration in hydrostatic and shock pressure etc. are also explained in detail.

Front and rear surface damage threshold of borosilicate glass, used for making confinement geometry targets, and their dependency on laser parameters are investigated and presented in **Chapter 3**. The laser induced damage width, geometries and microstructure changes are analyzed with optical microscope, scanning electron microscope and Raman spectroscopy. The results show that at low laser intensities symmetrical damages are found and

these damage width increases nonlinearly with laser intensity and get saturated after a certain intensity. The damage threshold energy depends on laser pulse duration as  $t_p^\alpha$ , where  $t_p$  is laser pulse duration and the value of  $\alpha$  for BK7 glass is estimated as  $\sim 0.2$  and  $\sim 0.3$  for front and rear surface respectively. It is observed that the rear side of the optical glass being used for the confinement of plasma can sustain the threshold fluence of about  $75 \text{ J/cm}^2$  and  $31 \text{ J/cm}^2$  at the fundamental wavelength for nanosecond and sub-nanosecond laser pulses respectively. Below these laser fluences; laser will pass through the glass without any damage and interact directly to the Aluminium foil. This Aluminium foil is being used as a shock wave generator. The thermal losses in the case of picoseconds heating is much lower than nanosecond heating due to lower interaction time and hence the damage spot diameter is smaller in picoseconds heating. The estimated average temperature and density for nanosecond produced plasma from the optical emission spectrum is around  $0.94 \text{ eV}$  and  $10^{17} \text{ cm}^{-3}$ . The SEM record of the damage spot due to nanosecond and sub-nanosecond laser pulses shows that in case of long pulse, the tensile stress exceeds the dynamic strength of the material which causes the cracks and fracture. However, for short pulse laser, laser ablation is accompanied by the electron heat conduction and melting processes are dominated. It is observed that for the longer pulse duration, the thermal diffusion length is longer and temperature gradient is also higher which can cause larger damage area. Lastly, the laser modified and unmodified regions are studied with the help of Raman spectroscopy. The Raman results show that vibrational groups are more easily damaged by nanosecond laser pulses. The recorded Raman spectrum has similar nature for both the pulses and suggests that the processes involved in the permanent transformation are ionic rather than bond or covalent conversion.

**Chapter 4** describes the Raman spectroscopy analysis for Polystyrene and PVT that reveals the behavior of these aromatic polymers under shock compression. Plastic scintillator radiation detectors based on polystyrene and poly vinyl toluene (PVT) are well known and are being commercially produced by Saint Gobain, USA for various radiation monitoring applications. These scintillators are produced by controlled polymerization of the corresponding monomers in the presence of suitable organic fluorescent additives. Various fluorescent additives and polymerization techniques have been investigated to produce most efficient scintillator detectors. In context of advancement of scintillating detectors, studies of the response of radiation scintillators under extreme conditions are important.

The Hugoniot relation for Aluminium, polystyrene are taken as  $U_s = 5.16 + 1.25u_p$  and  $U_s = 2.494 + 1.47u_p$  for shock pressure calculations. In these relations  $U_s$  and  $u_p$  are the shock and particle velocity respectively. The shock pressure induced shifts of the vibrational modes common to both systems are almost similar. The changes in vibrational frequencies of fundamental Raman peaks ( $\nu_{12}$  mode and  $\nu_{8a}$  mode) have been observed with respect to shock wave propagation. A maximum vibrational frequency shift caused by shock compression is found to be  $5 \text{ cm}^{-1}$  for polystyrene  $\nu_{12}$  mode. The results of the peak shift under 2.0 GPa agree with reported static compression data of Polystyrene. For PVT, all observed modes show a linear relation with static pressure. The relationship between the static pressure induced peak shift ( $\nu$ ) and pressure (P) for 1001, 1031 and  $1602 \text{ cm}^{-1}$  modes; are  $\nu = 1001 + 2.33P$ ,  $\nu = 1031 + 3.08P$  and  $\nu = 1602 + 3.94P$  respectively. There is no evidence observed for changes in the slopes of the peak shift-pressure plots [ $d\nu/dP (\text{cm}^{-1}/\text{GPa})$ ] up to  $\sim 2$  GPa, for PVT and polystyrene under shock compression. This indicates, there are no chemical processes involved for the generation and/or breaking of intra-molecular bonds in present experimental

conditions. The  $1602\text{ cm}^{-1}$ ,  $\nu_{8a}$  mode of PVT shifted at an average rate of  $3.94\text{ cm}^{-1}/\text{GPa}$ . This is higher than the shift in the Raman active mode of polystyrene at  $1606\text{ cm}^{-1}$ , which is shifted by an average of  $3.50\text{ cm}^{-1}/\text{GPa}$  over the same pressure range. The slope of the plot defines the extent of the anharmonicity. However, higher energy modes of PVT are showing relatively higher anharmonicity compared to Polystyrene with increase of pressure. For the final pressure of 2.25 GPa for the present experiment, the bond frequencies of PVT shifted by an amount of 0.6% to 0.8% from the ambient pressure value. Thus the changes in the bond length are of the order of 0.06-0.08%. In contrast, the changes in volume for the corresponding pressure are  $\approx 15\%$ . This clearly indicates that the primarily volume changes (below 1GPa) are due to free volume and compression of the inter-chain bonds, and not because of changes in intermolecular bond lengths. The individual mode Grüneisen Parameters are calculated for each Raman modes. It is observed that the anharmonicity in PVT for higher frequencies are more than the polystyrene. All the observed results shows both aromatic polymers are stable under shock loading and are reversible up to 2 GPa.

**Chapter 5** describes the shock wave induced high pressure and nanosecond time resolved spontaneous Raman spectroscopic studies to examine the dynamic response of fluoro polymer, Polytetrafluoroethylene (PTFE) in confinement geometry target assembly. The time resolved Raman spectroscopy is used to observe the pressure induced molecular and physical changes on nanosecond time scale. Raman spectra are measured as a function of shock pressure in the 1.2–2.5 GPa range. The observed peak assigned as  $\text{CF}_2$  twisting at  $291\text{ cm}^{-1}$  shows red shift with the pressure, while peaks at 381, 729 and  $1380\text{ cm}^{-1}$  assigned as  $\text{CF}_2$  bending modes, symmetric stretching mode of  $\text{CF}_2$  and C–C respectively, show blue shift with pressure. Furthermore, the vibrational mode at  $729\text{ cm}^{-1}$ , symmetric stretching mode of  $\text{CF}_2$  is compared to

corresponding static high pressure measurements carried in a diamond anvil cell. Observed changes in  $729\text{ cm}^{-1}$ , Raman spectra line width (FWHM) indicates that the shock pressure gradient is responsible for Raman peak broadening rather than shock induced temperature in PTFE film. A relationship between pressure induced shift ( $\nu\text{ cm}^{-1}$ ) and applied pressure (P GPa) for static compression for symmetric stretching mode of  $\text{CF}_2$  is given by the linear equation  $\nu = 5.08P$ . According to this relation, the shift  $12\text{ cm}^{-1}$ ; corresponds to a pressure of 2.4 GPa inside PTFE, which is in good agreement with pressure values under dynamic compression. By using time evolution of Raman intensity ratios, at the delay time 38, 52, 60 and 80 ns, the Raman intensity ratios belonging to the shocked area are 0.23, 0.72, 1.04, and 2.2, respectively. The shock velocity is estimated by the following equation:  $U_s = r \cdot t$ , where  $U_s$  is the shock wave velocity,  $r$  is the rate of change of Raman intensity ratio from shocked to total region and  $t$  is the thickness of the PTFE. According to the above intensity ratio data the fitted value of  $r$  is,  $(0.014 \pm 0.001) \times 10^9\text{ s}^{-1}$ . Hence the approximate shock velocity inside the PTFE calculated to be  $1.68 \pm 0.12\text{ km/s}$ . This is in good agreement with the calculated shock velocity using 1D radiation hydrodynamic simulations.

**Chapter 6** describes the in-situ spontaneous Raman spectroscopy studies of shock response of thermoplastic polymer, PMMA under confined photo-thermal laser ablation. The magnitude of shock pressures in PMMA as a function of incident laser intensity is calculated from the Hugoniot of the standard (in this case aluminum), taking the EOS data from SESAME and QEOS and utilizing the impedance matching technique.

The positions of the observed fundamental modes of PMMA are measured as a function of shock pressure. All vibrational modes are showing pressure induced broadening and are shifted to higher wavenumber with the pressure. The pressure induced peak shift ( $\nu$ ) for 599,

813, 1453 and 1735  $\text{cm}^{-1}$  Raman modes are found varying linearly with pressure ( $P$ ) as;  $\nu = 599 + 3.09P$ ,  $\nu = 813 + 2.65P$ ,  $\nu = 1453 + 1.6P$  and  $\nu = 1728 + 2.0P$  respectively. The shift in Raman mode C–C–O at 599  $\text{cm}^{-1}$ , is found higher than other modes. The higher shift for C–C–O at 599  $\text{cm}^{-1}$ , indicates the greater anharmonicity in the potential energy surface of this mode or the local volume compression near this coordinate is larger than the other modes. The larger shift of C–C–O mode at 599  $\text{cm}^{-1}$  than the C–O–C mode at 813  $\text{cm}^{-1}$ , is because C–O–C mode is of more extended from the polymer backbone relative to C–C–O mode, this suggests that the smaller shift is due to smaller intrinsic anharmonicity for this vibrational mode. Observed peak shift and line width data are used to determine mode Grüneisen parameters and bond anharmonicities. These shock compressed states are also compared with the static compression data, to see if any general trend can be established.

**Chapter 7** summarizes the important findings of the present research work. This thesis presents the physical response of different polymers and their structural stability under shock compression. Time resolved Raman spectroscopy has been used as a main technique to characterize these polymeric systems. The results are compared with other polymers under high pressure and shock compression experiments. The main results of the thesis are:

- (i) The shock pressure in confinement geometry depends on incident laser intensity and has main limitation of dielectric breakdown of transparent materials used for confinement. The damage threshold energy depends on laser pulse duration as  $t_p^\alpha$ , where the value of  $\alpha$  for BK7 glass is estimated as  $\sim 0.2$  and  $\sim 0.3$  for front and rear surface respectively.
- (ii) The maximum shock amplitude and shock duration attained in the confined ablation are approximately 10 and 6 times higher in comparison to direct ablation case for the same laser irradiance.

- (iii) The vibrational spectra and equation of state under shock compression are quite similar for both aromatic polymers (PS and PVT). However, there are small differences in the vibrational spectrum. Further studies under higher shock compression are required to quantify these differences. Grüneisen Parameters are calculated for each modes which indicates that the primarily volume changes (below 1GPa) are due to free volume and compression of the inter-chain bonds, and not because of changes in intermolecular bond lengths. It is observed that the anharmonicity in PVT for higher frequencies are more than the polystyrene. All the observations show that both aromatic polymers are stable compound under shock compression and reversible up to our experimental pressure range.
- (iv) Evidence for a possible phase transition from phase II–III is found for semi-crystalline fluoro polymer (PTFE) near 1 GPa. Observed changes in the Raman spectra line width (FWHM) indicates that the shock pressure gradient is responsible for Raman peak broadening rather than shock induced temperature in PTFE film. The shock velocity inside the PTFE is calculated as  $1.68 \pm 0.12$  km/s, by the time dependent integrated intensity variation of the shock front.
- (v) The shift in Raman mode C–C – O at  $599\text{ cm}^{-1}$ , is found higher than other modes for PMMA. The higher shift for C–C – O at  $599\text{ cm}^{-1}$ , indicates the greater anharmonicity in the potential energy surface of this mode or the local volume compression near this coordinate is larger than the other modes.

To conclude, this thesis presents a study of different polymeric materials in confinement geometry target assembly using time resolved Raman spectroscopy under laser-driven shock compression. Three different types of polymers are studied. These polymers differ in their

weight, degree of crystallinity, and amount of branching and cross-linking. Several different aspects of polymer physics are examined by performing studies under shock loading. Vibrational spectroscopy under shock compressions reveals the effects of extreme conditions at the level of chemical bonds. The vibrational modes shift with shock pressure reveals information about the anharmonicity of the intra-molecular potentials. When combined with an equation of state, mode Grüneisen parameters are obtained. In addition to obtaining information about the molecular bonds, information about the arrangement of the polymer chains can also be obtained. In amorphous polymers, compression of the material removes void space in the polymer. In semi-crystalline polymers, compression may lead to changes in chain conformations and the lattice structure. Information such as this on the molecular level can also be related to the macroscopic mechanical and thermodynamic properties. Time resolved Raman spectroscopy shows signatures of these phase transitions and shows its importance under shock loading for such studies.



## List of Figures

Figure 1. 1 (a) Pressure-time plot for steady shock wave (b) Shock wave with rarefaction wave bringing pressure back down to initial value, the graph is adapted from J. Frobes [19].	4
Figure 1. 2. Idealized variation in pressure with time behind a shock wave followed by expansion wave. The duration of the compression pulse ranges from tens of picoseconds to a few nanoseconds (in laser-induced shock loading) to a few microseconds (in projectile or gas-gun generated shock).	8
Figure 1. 3. A forward facing $P-u_p$ curve centered at $P = 0, u_p = 0$ and a backward facing $P-u_p$ curve reflected through $(P_q, u_q)$ , are used to determine the state behind a second backward facing shock.	9
Figure 1. 4. $x-t$ and $P-u_p$ diagram for a shock crossing a material boundary into a higher impedance material II.	10
Figure 1. 5. Impedance matching for a shock incident on a higher impedance material (Case 1).	12
Figure 1. 6. Impedance matching for a shock incident on lower impedance material (case 2).	12
Figure 1. 7. Impedance matching for rarefaction incident on higher impedance material (case 3).	12
Figure 1. 8. Impedance matching for rarefaction incident on lower impedance material (case 4).	12
Figure 1. 9. Case 1 where material II has higher impedance than material I.	13
Figure 1. 10. Case 2 where material II has a lower impedance than material I.	13

Figure 1. 11. (a) Definition of dihedral angle. The circle indicates the axis of the central C-C bond, which is perpendicular to the page (b) Potential energy diagram for butane as a function of the dihedral angle. The graph is adapted from Cowie [30].	15
Figure 1. 12. Structure of (a) trans and (b) gauche butane. Here the carbon atoms are shown in grey while hydrogen atom and CH <sub>3</sub> group are shown by light grey and blue, respectively.	15
Figure 1. 13. Structure of the chains of (a) polyethylene, (b) poly (tetrafluoroethylene), and (c and d) $\alpha$ - and $\beta$ -PVDF. Carbon atoms are shown in grey while hydrogen and fluorine atoms are shown in light grey and blue, respectively.	17
Figure 1. 14. Energy level diagram for Raman Scattering	24
Figure 1. 15. (a) Creation of photon corresponding to Stokes scattering (b) Annihilation of photon corresponding to anti-Stokes Scattering.	26
Figure 2. 1. (a) Pump laser beam profile used for shock generation in Al-foil measured with the beam profiler. The beam profile of the laser beam is super Gaussian in spatial domain, (b) temporal profile of the laser pulse, (c) spectral width of the laser beam measured with the wavelength meter and (d) laser energy reproducibility or fluctuation with shot number (<0.2%).	31
Figure 2. 2. Schematic drawing of the confinement geometry target assembly.	34
Figure 2.3. Schematic diagram of Raman spectrometer; where M1 and M2 are reflecting concave mirrors, S1, S2 are entrance and S3 is exit slits respectively; and G is holographic grating target having 600, 1200 and 2400 grooves.	35
Figure 2. 4. Screen shot of the data acquisition system used for recording the data, taking CCl <sub>4</sub> as a sample.	36

Figure 2. 5. Schematic of diamond anvil cell (DAC) with sample and pressure sensor.....	37
Figure 2. 6. (a) Schematic of the experimental setup; where $M_{1-9}$ –reflecting mirrors; QWP– quarter wave plate; P–polarizer; DSO–digital oscilloscope; ICCD–intensified charge coupled device (b) Scanning of signal $CCl_4$ for $\pm 5$ ns around the set delay between pump and probe beams. ....	39
Figure 2. 7. (a) Synchronization of the set up using fast photo diode and digital oscilloscope, (b) photograph of multi pass delay generator.....	40
Figure 3. 1. Schematic of experimental setup; where EM1 and EM2- energy meters; PD- photodiode; CCD- charge coupled device; SP- optical spectrometer.....	45
Figure 3. 2. Optical microscope images of the front surface of the sample at 4 mJ energy where; (a) $\lambda= 1064\text{nm}$ , $t_p= 8$ ns without $N_2$ flow (b) $\lambda= 1064\text{nm}$ , $t_p= 500$ ps without $N_2$ flow (c) $\lambda= 1064$ nm, $t_p= 8$ ns with $N_2$ flow (d) $\lambda= 532\text{nm}$ , $t_p= 500$ ps without $N_2$ flow (e) $\lambda= 1064\text{nm}$ , $t_p= 8$ ns with $N_2$ flow, 50 shots (f) $\lambda= 532\text{nm}$ , $t_p= 500$ ps with $N_2$ flow (g) optical microscope images of rear surface damage at $\lambda= 532$ nm, $t_p= 500$ ps (h) optical microscope images of rear surface damage at $\lambda= 532\text{nm}$ , $t_p= 8$ ns (i) $\lambda= 1064$ $t_p= 500\text{ps}$ without $N_2$ , at higher laser energy focused at rear side. In figure 3.2 (a), the magnification is 9x and for figure 3.2 (b-i) magnification is 6x..	52
Figure 3. 3. Photodiode signal of scattered light from damage spot at various laser energies. ....	55
Figure 3. 4. Dependency of damage width on (a) laser pulse duration and at fixed wavelength i.e. 532 nm (b) laser wavelength for fixed pulse duration (c) effect of inert gas flow on damage width and (d) the number of shots at the same position for a fixed laser parameters.....	56

Figure 3. 5. (a & b) show SEM images of irradiated glass target with 500x and 3Kx magnification for the laser pulse  $t_p= 500$  ps and energy 4 mJ and (c & d) for the laser  $t_p= 8$  ns and energy 4 mJ. .... 58

Figure 3. 6. Percentage transmitted energy as a function of incident laser energy where; (a) front surface % glass transmission at  $\lambda= 1064$  nm,  $t_p= 500$  ps and 8 ns (b) rear surface % glass transmission at  $\lambda= 1064$  nm,  $t_p= 500$  ps and 8 ns; (c) front surface % glass transmission at  $\lambda= 532$  nm,  $t_p= 500$  ps and 8 ns; (d) rear surface % glass transmission at  $\lambda= 532$  nm,  $t_p= 500$  ps and 8 ns. .... 59

Figure 3. 7. Raman spectrum from damaged and undamaged region of BK7 glass at  $t_p= 500$  ps and 8 ns. .... 61

Figure 3. 8. Recorded emission spectra of BK7 glass plasma irradiated by an Nd:YAG laser of pulse duration 8 ns and wavelength 1064 nm. .... 62

Figure 3. 9. Saha Boltzmann plot using Silicon excitation lines for plasma temperature estimation. .... 64

Figure 4. 1. The (a) thermogravimetric analysis (TGA) (where inset shows the chemical structure of polystyrene) and (b) differential scanning calorimetry (DSC) profiles of the polystyrene, recorded at a heating rate of 20°C per minute, under N<sub>2</sub> atmosphere and DSC profile recorded at 3°C per minute to measure glass transition temperature..... 71

Figure 4. 2. The thermogravimetric analysis (TGA) and differential scanning calorimetry (DSC) profiles of the PVT, recorded at a heating rate of 15°C per minute, under N<sub>2</sub> atmosphere. The inset in figure 4.2 shows the chemical structure of PVT. .... 72

Figure 4. 3. (a) Calculated instantaneous pressure in Al and polystyrene behind the shock front using the impedance mismatch technique with the known sample Hugoniot (b) shows impedance mismatch and simulation pressure variation with laser intensity. .... 73

Figure 4. 4. Normalized Raman spectra of polystyrene as a function of shock pressure for the range 100–1800  $\text{cm}^{-1}$ ; and the unshocked spectrum shows Raman spectrum of Polystyrene ambient pressure and temperature. The labels above the peaks are references to their mode assigned as in the table 4.2..... 78

Figure 4. 5. Raman blue shift of 1004 and 1034  $\text{cm}^{-1}$  modes, under dynamic shock compression with the unshocked Raman spectrum as a reference for peak shift under pressure. The dots in the figure 4.5 are the original experimental data, and the dashed lines are the fitted Gaussian function. The dashed vertical line measures Raman peak shift under shock compression. .... 80

Figure 4. 6. Pressure-dependent behaviors of observed Raman modes of polystyrene. The symbols show experimental data, and solid lines show the linear fit to the data under hydrostatic compression taken from reference [118]. Here error bars are comparable to the size of the symbols. .... 81

Figure 4. 7. Changes in Raman line widths ( $I_{\text{shocked}}/I_{\text{unshocked}}$ ) under shock compression for two fundamental modes of aPS..... 83

Figure 4. 8. Raman Spectrum of fundamental modes of PVT (a) under static compression for the range 950-1700  $\text{cm}^{-1}$  (b) under shock compression for the range 950-1700  $\text{cm}^{-1}$ . .... 84

Figure 4. 9. Raman blue shift of  $\nu_{12}$  mode at 1001  $\text{cm}^{-1}$  under dynamic shock compression. The open circles in the figure 4.9 are the original experimental data and the dashed lines are the fitted Gaussian function. The dashed black line measures Raman peak shift under shock compression. .... 85

Figure 4. 10. Pressure dependent behavior of PVT and polystyrene (PS) under static and shock wave compression. Where symbols shows the experimental data for Raman wavenumber shift under static and shock compression, and the solid lines show linear fit to the static compression data..... 86

Figure 4. 11. A log-log plot of the  $\nu_i(P)/\nu_i(0)$  vs  $V(0)/V(P)$  for all analyzed peaks of polystyrene. The graph shows the tendency of the vibrational modes to be individual volume independent Grüneisen parameters. .... 89

Figure 4. 12. Fractional compressibility ( $\rho/\rho_0$ ) of PVT for pressures below 15 GPa. .... 90

Figure 4. 13. A log-log plot of the  $\nu_i(P)/\nu_i(0)$  vs  $V(0)/V(P)$  for observed peaks of PVT under static and shock compression. The graph shows the tendency of the vibrational modes to be individual volume independent Grüneisen parameters..... 92

Figure 4. 14. Raman spectra of polystyrene as a function of shock delay times for the range 135-1885  $\text{cm}^{-1}$ , with unshocked Raman spectrum as a reference for peak shift..... 93

Figure 4. 15. (a) and (b) show time resolved Raman spectra of 1004 and 1606  $\text{cm}^{-1}$  mode at various delay times (c) Shock wave propagation inside Polystyrene at different delay times. The blue dashed line at 200  $\mu\text{m}$  shows the Polystyrene-Aluminium interface. These simulations are done by using 2D radiation hydrodynamic code. .... 95

Figure 4. 16. Relative intensity ratio for the shocked to whole region of the sample vs delays time. .... 97

Figure 4. 17. (a) Show time resolved Raman spectra of  $\nu_{12}$  mode at 1001  $\text{cm}^{-1}$  mode at various delay times (b) Shock wave propagation inside polystyrene at different delay times. The simulations are done by using 1D radiation hydrodynamic code. .... 98

Figure 5. 1. Phase diagram of PTFE. The graph is adopted from Brown et al [137] ..... 102

Figure 5. 2. (a) Calculated instantaneous pressure in Al and PTFE behind the shock front using the impedance matching technique with the known sample Hugoniot; (b) shows impedance mismatch and simulation pressure variation with laser intensity. .... 104

Figure 5. 3. Raman spectra of PTFE at ambient conditions after baseline correction. The broad peaks at 550 and 1100  $\text{cm}^{-1}$  are due to glass substrate..... 105

Figure 5. 4. Raman spectra of PTFE at ambient and static high pressure conditions. .... 106

Figure 5. 5. Shows Raman blue shift under dynamic shock compression. The dots in the figure 5.5 are the original experimental data and the dashed lines are the fitted Gaussian function respectively. The blue dashed line denotes the Raman peak shift under shock compression. ... 107

Figure 5. 6. (a) Pressure-dependent behaviors of observed Raman modes of PTFE. The symbols show experimental data, and solid lines show the linear fit to the data (b) Pressure vs peak shift under hydrostatic and shock compression for symmetric stretching mode of  $\text{CF}_2$  at 729  $\text{cm}^{-1}$ . Representative error bars are shown, indicating the estimated uncertainties in the peak shift. .. 109

Figure 5. 7. (a) The shocked to unshocked ratios for the  $\text{CF}_2$  symmetric stretching mode; the amplitude and the integrated intensity (area under the Raman peak), (b) the full width at half maximum (FWHM) under shock compression. Representative error bars are shown, indicating the estimated uncertainties in the peak amplitude and FWHM measurement. .... 110

Figure 5. 8. (a) and (b) Time resolved Raman spectra of twisting and symmetric stretching mode of  $\text{CF}_2$ . The time zero denotes the arrival of pump beam at the Aluminum foil. The different times are the time delays between pump and probe pulses. (c) Shock wave profile inside PTFE at different delay times generated by 1D radiation hydrodynamic code MULTI-fs. .... 113

Figure 5. 9. Ratio of the intensities of Raman peaks from the shocked and the total region for the peak 287 and 729  $\text{cm}^{-1}$  versus delay time. Representative error bars indicate the estimated uncertainties in the calculated relative amplitudes. .... 114

Figure 6. 1. (a) shock pressure calculation in Al and PMMA using principle Hugoniot data and impedance mismatch technique (b) represents variation of pressure with laser intensity. .... 122

Figure 6. 2. (a) Show time resolved Raman spectra of 813  $\text{cm}^{-1}$  mode at various delay times. The vertical dashed blue lines denote the Raman peak location at ambient and under shock compression (b) Shock wave propagation inside PMMA at different delay times. The simulations are done by using 1D radiation hydrodynamic code. .... 123

Figure 6. 3. (a) Molecular structure of Methyl methacrylate (b) PMMA repeating monomer unit. The labeled mode  $\nu_1$  represents the (C–C–O) stretching mode and  $\nu_2$  represents symmetric/anti-symmetric stretching modes of (C–O–C) respectively..... 125

Figure 6. 4. Normalized Raman spectrum of PMMA for the range 200–3300  $\text{cm}^{-1}$ , using 532 nm excitation..... 126

Figure 6. 5. Normalized, spontaneous Raman spectrum of PMMA as a function of shock compression for the range 200- 3300  $\text{cm}^{-1}$ . .... 127

Figure 6. 6. Fractional compressibility ( $\rho/\rho_0$ ) of PMMA for pressures below 8 GPa. .... 133

Figure 6. 7. A log-log plot for  $\ln [V(0)/V(P)]$  versus  $\ln [v_i(P)/v_i(0)]$  for analyzed peaks of PMMA. The solid lines are linear fits to the exact Grüneisen parameters. .... 135

## List of Tables

Table 3. 1. Threshold measurement for BK7 glass.....	49
Table 3. 2 Atomic parameters for the Si I, Si II and Si III used in temperature estimation .....	63
Table 3. 3. Spectral Parameters for Si I, Si II and Si III calculated free electron density .....	66
Table 4. 1. Parameters used for Hugoniot and shock pressure calculations, where Hugoniot is expressed as $U_s = C_0 + Su_p$ .....	72
Table 4. 2. Raman active vibrational modes analyzed under shock compression and mode dependent Grüneisen parameters ( $\gamma_i$ ).....	78
Table 4. 3. Changes in Raman line width under shock compression .....	82
Table 4. 4. Table of Volume independent Gruneisen parameters, ( $\gamma_i$ ).....	91
Table 6. 1. Parameters used for Hugoniot and shock pressure calculations, where $C_0$ (sound velocity in the bulk) and $S$ (shock parameter) are materials specific parameters [27] .....	121
Table 6. 2. Raman active modes under ambient conditions .....	127



## Chapter 1. Introduction

Shock compression plays a vital role in astrophysical, geological and materials research from basic science as well as technological point of view. It can induce myriads of structural as well as electronic changes and can also produce altogether new phenomenon and properties related with materials. The shock waves are supersonic disturbances typically having directional loading, non-isotropic compression, pressure range  $\sim 1-10^4$  GPa, time scales  $\sim 10^{-13}-10^{-6}$  s and nonlinear coupling between wave propagation and material response. Because of these properties shock waves can induce structural phase changes, elastic–plastic deformation and metal to insulator transitions. In addition, shock wave compression of materials, detonation of explosives, failure of materials reaching their intrinsic limit of performance, matter withstanding hypervelocity impacts of comets, high pressure and high temperature synthesis of novel materials, all these require an understanding of the fundamental mechanism of the response of materials at the atomic, micro structural and continuum level.

The understanding of these induced phenomena requires time resolved experiments at microscopic scales. Also, if we wish to tailor the behavior of material under shock compression, it is essential that we understand the shock wave effect at atomic and molecular level. In the process of shock compression, the shock wave many times generates unstable intermediates or non-equilibrium states. The *in-situ* time resolved Raman spectroscopy is a powerful tool to investigate those transient intermediates, excitation and relaxation process of matter as well as to obtain real time information of shock compression induced chemical and structural changes in the materials. For this, a time resolved Raman spectroscopy facility to study the dynamically shocked material has been developed at Laser Shock laboratory, HP&SRPD, BARC.

In comparison with other shock generation method such as gas gun loading, rail gun, impact loading [1]; laser shock has advantage of good synchronization, high loading efficiency small sample requirement and high repeatability. The laser driven shock wave experiments provide unique method to investigate the material evolution under shock loading; including phase transitions, chemical reactions as well as real time examination of time dependent mechanisms. In recent years, the time resolved spectroscopy has become an attractive experimental tool for investigating atomic and molecular dynamics of materials under shock loading [2]–[4]. As intermolecular interactions can be altered under shock loading and monomers may undergo phase transitions. Hence, these altered properties may provide new pathways to produce novel properties in materials that are distinct from conventional synthesis methods [5], [6]. Moreover, the understanding of microscopic behavior of materials at atomic and molecular level could be useful in order to specify excitation or relaxation processes of materials under shock compression. Such studies are also very important to study shock responses of energetic materials [7], [8].

Polymeric materials and polymeric composites play an important role in the modern technology and have attracted an increased level of interest in recent years, especially under dynamic compression [9]–[14]. The large molecular mass relative to small molecular compounds produces unique physical properties in polymers, including toughness, viscoelasticity and a tendency to form glasses and semi–crystalline structures rather than crystals. Polymers are broadly divided into several classes based on the scale at which the property is defined as well as upon its physical basis. The most basic property of the polymer is the identity of its constituent monomers. The polymeric molecules can undergo a wide variety of phase transitions as well as conformational changes because of interplay of intramolecular covalent bonds and Vander

Waal's and hydrogen intermolecular bonds between different molecules in the condensed phase. In earliest studies with several different polymers, the structural transition is found only in Teflon at 0.65 GPa. Since that time few more polymers are found showing phase transitions at high pressures. However, it is still not known how common these transitions would be in general. The investigation of polymeric materials temperature, pressure and volume behavior under dynamic loading would be valuable, particularly for constitutive models for modeling, equation of state (EOS) measurement and predicting their response under extreme conditions. Till date various measurements have been performed using technique such as infrared, CARS, spontaneous and stimulated Raman spectroscopy to examine the polymers behavior at molecular level under compression [15]-[19]. More extensive studies of polymers under dynamic compression or extreme conditions would be very helpful to elucidate the fundamental processes these materials undergo.

This chapter gives a brief introduction about shock waves, impedance mismatch technique and their application, physical properties of polymers as well as theoretical formulations of Raman spectroscopy. At the end of this chapter the motivation for the present work is also discussed.

## **1.1. Shock Waves**

When the amplitude of stress waves greatly exceeds the dynamic flow strength of a material in comparison with the compressive hydrostatic component of the stress, this leads to a high-amplitude disturbance traveling into a material [18]. The disturbance front will steepen-up as it travels through the material because the higher amplitude regions of the front travel faster than the lower amplitude regions. This leads to a shock wave, which is defined, ideally, as a discontinuity in pressure, internal energy or temperature and density. Thus, shock

waves are characterized by a sharp discontinuity in the thermodynamic variables of the material. It travels faster than the speed of sound in the medium ahead of the shock i.e. shock waves are supersonic [19]. When a shock wave passes through matter, the energy is preserved but entropy increases. A 1D shock wave goes from one compression level (usually zero) to higher compression level in an almost discontinuous jump as a function of time [19] and is shown in figure 1.1 (a). Shock waves compress the material in a fraction of microsecond putting energy directly into atoms and molecules. Shock waves also create defects in materials, which increases entropy [19]. An excellent review on the fundamentals of shock wave phenomena and ultrafast spectroscopy of shocked material is given by Dana D. Dlott [20].

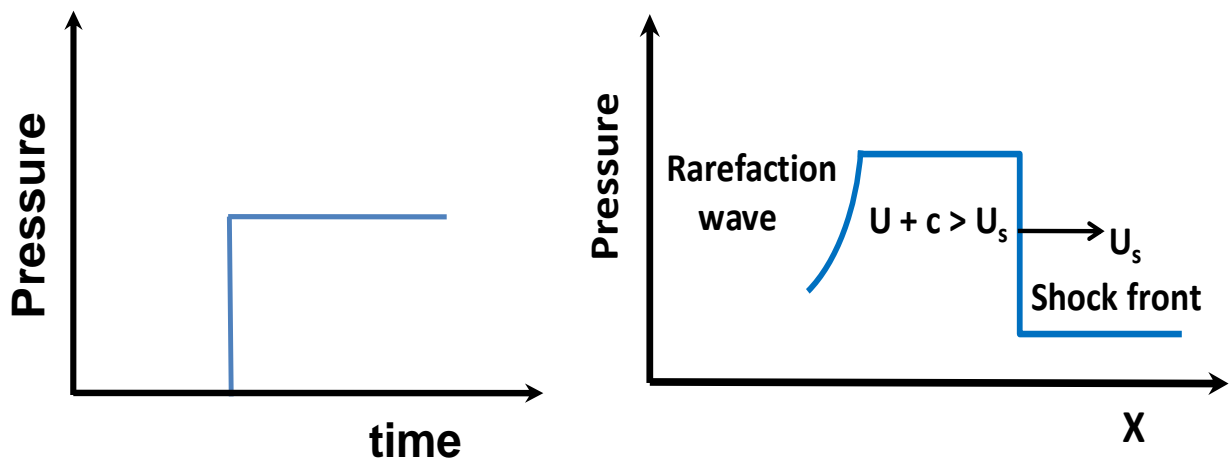


Figure 1. 1 (a) Pressure-time plot for steady shock wave (b) Shock wave with rarefaction wave bringing pressure back down to initial value, the graph is adapted from J. Frobes [19].

Shock waves allow us to study fast evolution structural processes in the higher energy regions of the energy landscape, which are difficult or impossible to access by conventional techniques. The experimental devices used for shock loading can be classified according to energy source as:

1. Gun type launchers like powder guns, light–gas guns and ballistic shock tubes

2. Explosive systems based on powerful condensed high explosives
3. Electric and electromagnetic guns
4. Devices using radiation sources like lasers, x-rays, etc.

The measurement of dynamic properties of materials under extreme conditions requires use of specialized, sophisticated equipment and techniques. A brief discussion on several of the approaches used previously has been presented in this section. The time-resolved Raman spectroscopy has proven valuable in the microscopic characterization of symmetry and structural changes in the shocked state [21]. Time-resolved Raman spectroscopy studies were performed on benzene derivatives under laser-driven shock compression up to a few GPa, in order to investigate the effects of steric hinderance and chemical structure on the molecular dynamics under shock compression [22]. It was observed that, the ring-breathing mode of benzene showed a high frequency shift of  $10 \text{ cm}^{-1}$  which corresponded to a ring reduction of 0.7% under shock compression. The magnitude of frequency shift showed a systematic dependence on intermolecular distance. The ring breathing mode is decreased, while the ring-vibration is increased, since the molecules are forced to come close together. The nanosecond time-resolved Raman spectroscopy is also used to investigate the bond strength and structure of molecules and the crystals under shock compression using a pump-probe technique [23]. Tas et al. have characterized the nano shock waveform by measuring the shock front rise-time, shock fall-time, velocity and peak pressure using CARS [24]. Lagutchev et al. have used laser-driven shock waves  $\sim 1 \text{ GPa}$  to dynamically compress self-assembled monolayers (SAMs) [25]. They found evidence of a complicated viscoelastic response of materials under shock loading and also observed that the SAM response to shock is dependent on both the molecular structure and on the lattice structure as determined by the metal substrate. In viscoelastic shock compression the

shock front consists of two parts, a faster elastic part and a slower plastic deformation part. As the shock front propagates, the elastic part moves ahead and disperses whereas the plastic part lags behind and remains steep. This time lag is a measure of the rate of mechanical deformation or shape change at high strain rates. The ultrafast laser–driven shock waves generating pressures up to 5 GPa were used to study molecular orientational processes occurring in a thin layer of polycrystalline energetic material [26]. It was found that there is an orientational sensitivity of energetic materials to the direction of shock front propagation.

## 1.2. Shock characterization: Principal Hugoniot

A shock wave is different from the acoustic sound waves in condensed matter. It creates high pressure, mass particle speed, and internal energy changes in condensed matter. The thermodynamic parameters pressure (P), volume (V), internal energy (E) are related to the hydrodynamic parameters of shock velocity ( $U_s$ ) and particle velocity ( $u_p$ ). This means the thermodynamic parameters can be accurately determined from shock wave parameters. The shock waves can be characterized by two variables, the shock velocity ( $U_s$ ) and particle velocity ( $u_p$ ). The shock velocity is defined by the velocity of the shock wave in the material being impacted and the particle velocity is the speed with which the material at the point of interest is moving [27]. The relationship between several points of  $U_s$  vs  $u_p$  is known as material's principal Hugoniot. The quantitative relationship which governs the behavior of shock waves is derived by using Rankine–Hugoniot equations. By considering 1D steady flow of a non-viscous, compressible fluid, the following equivalent expressions of conservation of mass, momentum, and energy all apply [19]:

$$\rho_0 U_s = \rho(U_s - u_p) \quad (1.1)$$

$$P - P_0 = \rho_0 U_s u_p \quad (1.2)$$

$$E - E_0 = \frac{1}{2} (P - P_0)(V_0 - V) \quad (1.3)$$

where  $P$  is pressure,  $V$  is specific volume,  $\rho$  is the density,  $E$  is energy; and initial states of the material are denoted by subscript zero [27].

The principal Hugoniot can be described by any combination of these parameters for a material. It is important to note that the Hugoniot is not a path that a shocked sample takes, but a curve consisting all of the possible states the material can be shocked to from its initial state [27]. In the above equations there are five variables. To determine all the parameters as a function of one of them, an additional equation is needed. This equation can be expressed as the relationship between shock and particle velocities, and has to be experimentally determined.

$$U_s = C_0 + S u_p \quad (1.4)$$

where,  $C_0$  is the sound velocity in the material at zero pressure and  $S$  is the shock parameter. Almost for all materials not undergoing phase transition, equation (1.4) is valid. The figure 1.2 shows idealized variation of pressure with time behind a shock wave followed by the expansion wave.

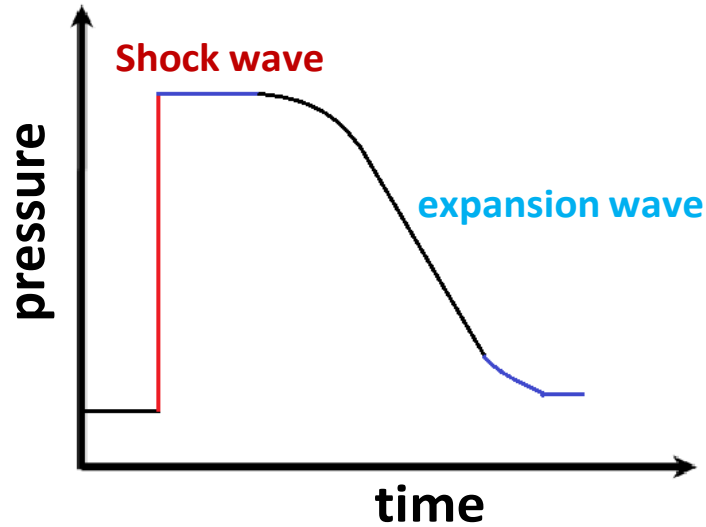


Figure 1. 2. Idealized variation in pressure with time behind a shock wave followed by expansion wave. The duration of the compression pulse ranges from tens of picoseconds to a few nanoseconds (in laser-induced shock loading) to a few microseconds (in projectile or gas-gun generated shock).

### 1.3. Impedance Mismatch technique

A fundamental thing required in shock wave physics is to determine EOS ( $P-u_p$ ) states behind the shock waves after they have reflected from the material boundary or intersect another wave. In most cases impedance mismatch technique is accurate but when the state ahead of the shock is not at  $P= u_p= 0$ , small errors occur. However these errors are typically smaller than actual measurement errors for  $P-u_p$  parameters [19].

### 1.4. Practical uses of Impedance Mismatch technique

- Experimental designs and interpretation of experimental results
- Determining peak stresses in materials that is hit by a flat plate or induced in layers of materials in contact with each other
- Shock mitigation techniques can be understood using this technique

- Shock pressure amplification in targets

### 1.5. $P-u_p$ curves for materials with $U_s = A + bu_p$

Most of the materials have linear relation with shock velocity and particle velocity especially at high pressures where materials become stiffer. A material with linear  $U_s - u_p$  will have a quadratic equation defining shock pressure for forward facing shock waves. For the parabola vertex at  $P = u_p = 0$ ,

$$P = \rho_0 A u_p + \rho_0 b u_p^2 \quad (1.5)$$

Due to symmetry the reflected parabola through state  $(P_q, u_q)$  in figure 1.3 is represented by

$$P = \rho_0 A (2u_q - u_p) + \rho_0 b (2u_q - u_p)^2 \quad (1.6)$$

The equations 1.5 and 1.6 are used to calculate the shock pressure inside the sample of interest and is discussed in chapters 4, 5 and 6.

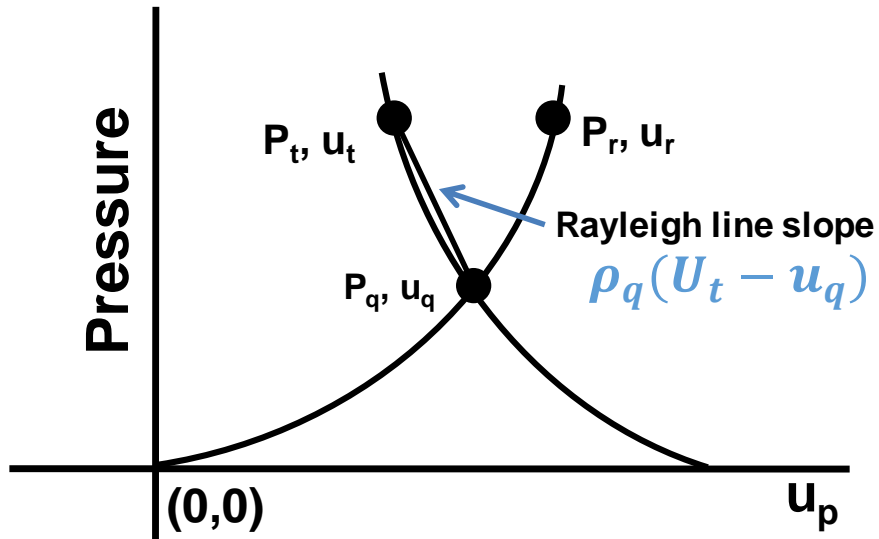


Figure 1. 3. A forward facing  $P-u_p$  curve centered at  $P = 0, u_p = 0$  and a backward facing  $P-u_p$  curve reflected through  $(P_q, u_q)$ , are used to determine the state behind a second backward facing shock.

### 1.6. $P-u_p$ diagram for a shock crossing a boundary into a material of higher impedance

For  $P-u_p$  diagrams it is always necessary to first draw a generic  $x-t$  diagram as a guide. Going from field **a** to **e** in  $x-t$  diagram in figure 1.4 across the forward facing shock  $S_1$  in material I. Field **a** has  $P = u_p = 0$ , but field **e** is behind shock  $S_1$  so its state is  $(P_e, u_e)$  and has to lie on the principle Hugoniot of material I. Upon forward facing shock arrival at material boundary, forward facing shock  $S_2$  is transmitted across the boundary in material II and shock  $S_3$  is reflected from the higher impedance boundary back into material I (see figure 1.4).  $S_2$ 's shock state has to be somewhere on the forward facing  $P-u_p$  curve for material II. The reflected shock  $S_3$  will have to be at a state on a backward facing  $P-u_p$  curve for material I with initial state  $(P_e, u_e)$ , so material I's principle  $P-u_p$  is reflected around state **e**. This gives a backward facing  $P-u_p$  curve for material I from initial state  $(P = 0, u_r)$ . Symmetry of these curves gives,  $u_r = 2u_e$ .

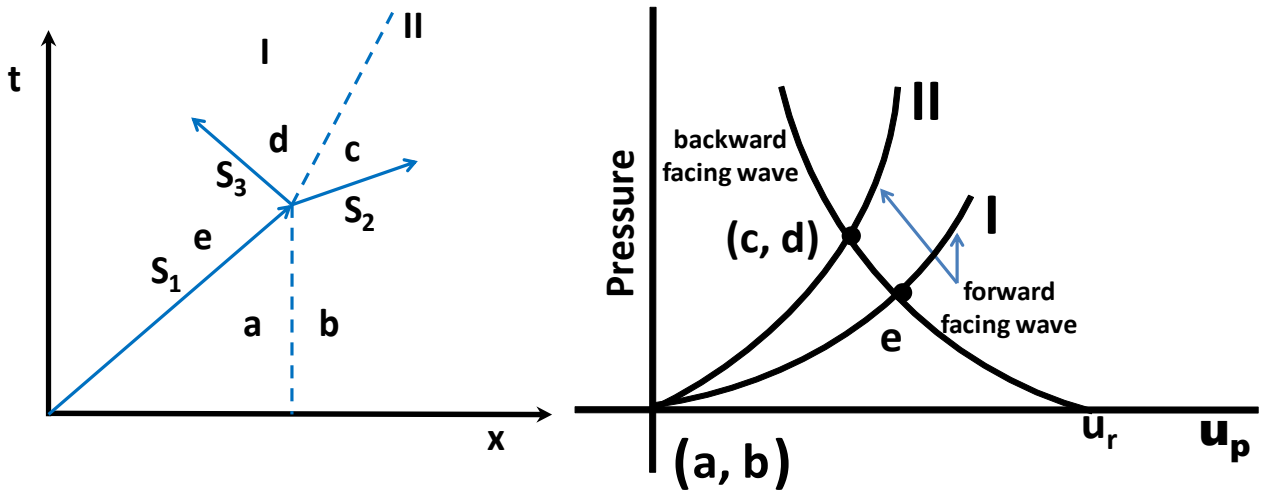


Figure 1. 4.  $x-t$  and  $P-u_p$  diagram for a shock crossing a material boundary into a higher impedance material II.

For a material with linear  $U_s - u_p$  equation 1.2 can be written as:

$$P = \rho_0[A + b(2u_e - u_p)][2u_e - u_p] \quad (1.7)$$

It is clear that the only  $(P, u_p)$  point that meets these criteria is at **(c, d)** where the backward facing  $P-u_p$  curve from state **e** and forward facing  $P-u_p$  curve cross.

### 1.7. Rules for impedance matching

A shock or rarefaction wave incident on a boundary of higher impedance will transmit and reflect the same type of wave as the incident wave. A wave incident on the boundary of lower impedance will transmit the same type of wave as the incident wave but will reflect opposite type of wave [19].

### 1.8. Impedance matching for four basic cases

Four cases will illustrate this rule and boundary condition. The graphs 1.5–1.10 is adopted from reference [19].

**Case 1:** A right travelling shock incident on a higher impedance material II i.e.  $\rho_0^I U_s^I(P_1) < \rho_0^{II} U_s^{II}(P_2)$ ;

**Case 2:** A right travelling shock incident on a lower impedance material II i.e.  $\rho_0^I U_s^I(P_1) > \rho_0^{II} U_s^{II}(P_2)$ ;

**Case 3:** A rarefaction step wave incident on a higher impedance material II i.e.  $\rho_0^I U_s^I(P_1) < \rho_0^{II} U_s^{II}(P_2)$

**Case 4:** A rarefaction step wave incident on a lower impedance material II i.e.  $\rho_0^I U_s^I(P_1) > \rho_0^{II} U_s^{II}(P_2)$

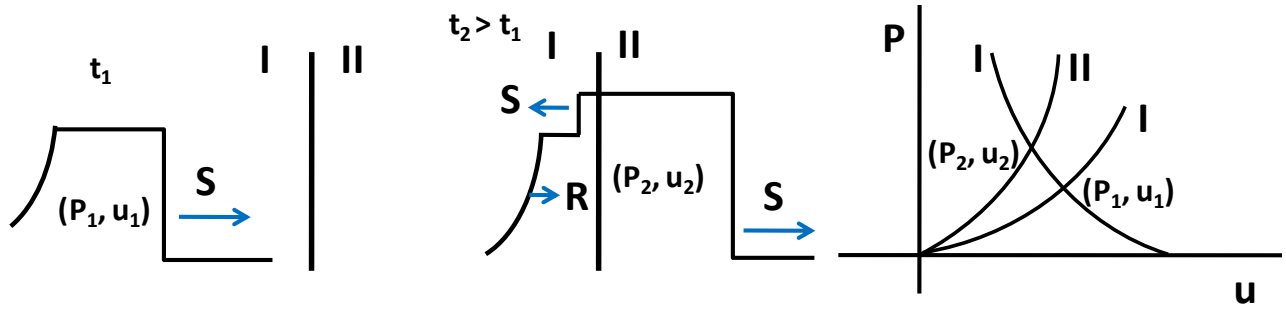


Figure 1. 5. Impedance matching for a shock incident on a higher impedance material (Case 1).

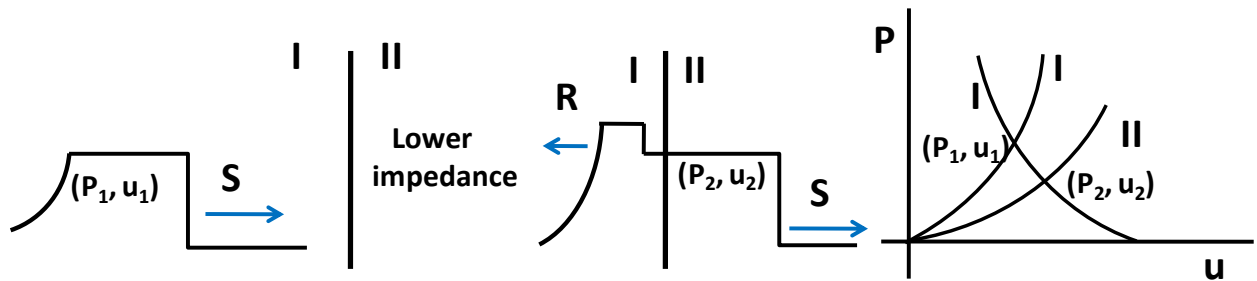


Figure 1. 6. Impedance matching for a shock incident on lower impedance material (case 2).

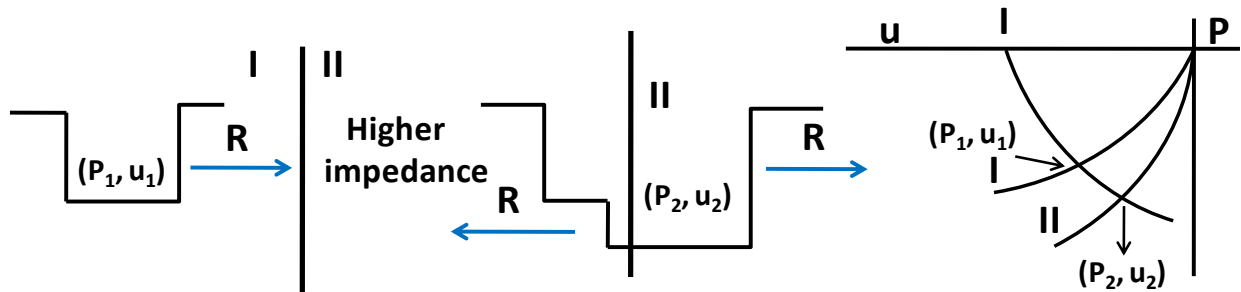


Figure 1. 7. Impedance matching for rarefaction incident on higher impedance material (case 3).

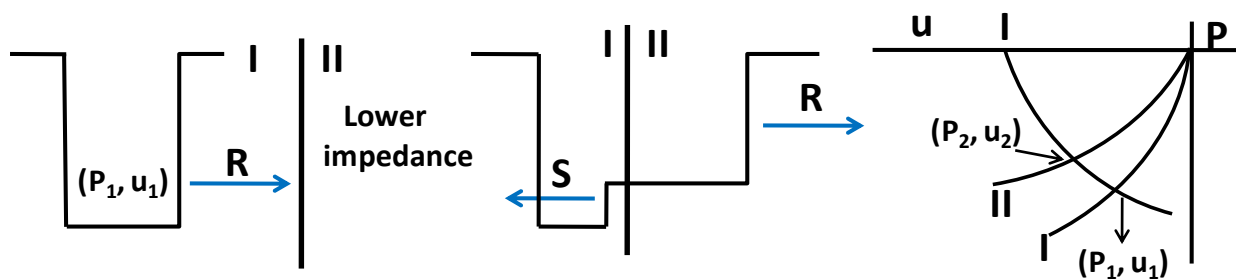


Figure 1. 8. Impedance matching for rarefaction incident on lower impedance material (case 4).

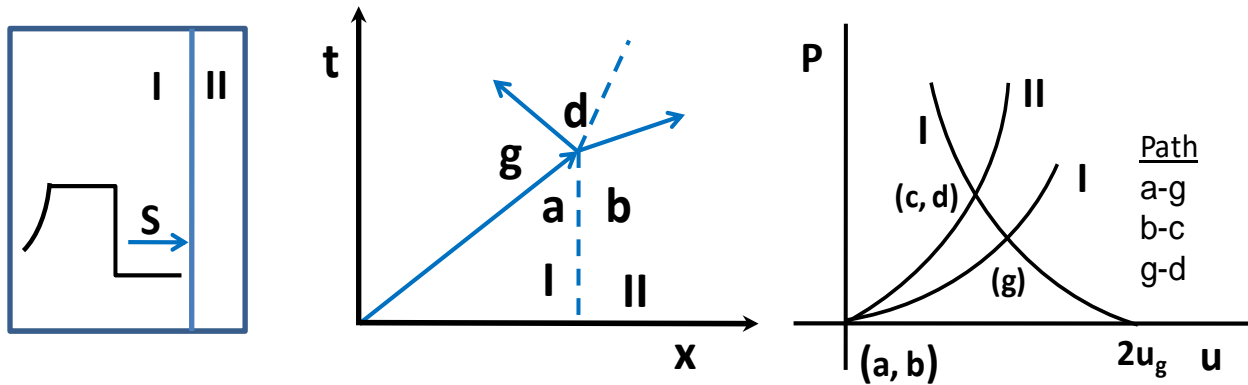


Figure 1. 9. Case 1 where material II has higher impedance than material I.

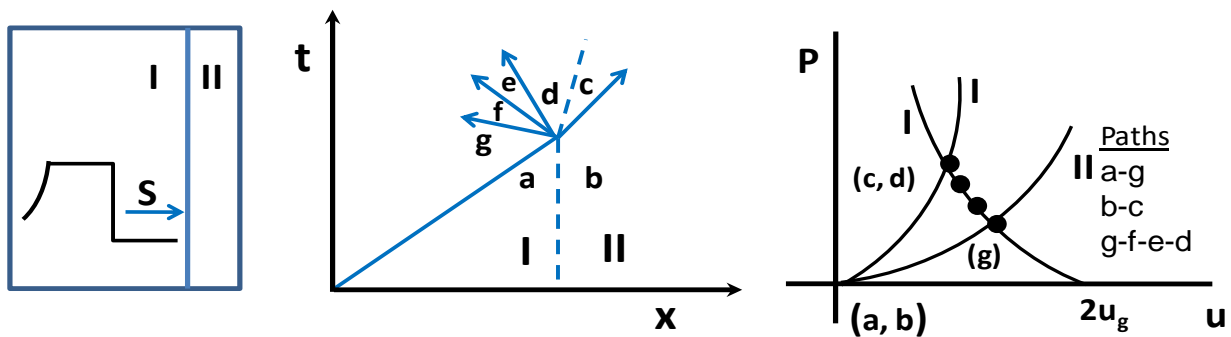


Figure 1. 10. Case 2 where material II has a lower impedance than material I.

### 1.9. Physical Properties of Polymers

There are different types of polymeric materials. Among them the most important technologically are organic polymers. These are the focus of the research under shock compression described in this dissertation. A short overview of polymer science can be found in Bower and Maddams [28]. A textbook focusing the chemistry and physics of polymers under high pressure is A. L. Kovarskii [29].

### 1.10. Polymers configuration and conformations

The polymers are defined as macromolecules composed of one or more chemical units that are repeated throughout a chain. The simplest organic polymer, polyethylene, is produced when ethylene ( $C_2H_4$ ) molecules break their double bonds and linked together. The monomer units

contain a double bond joining the carbon atoms. Hence, the carbon atom orbitals are  $sp^2$  hybridized and all the bond angles are approximately  $120^\circ$ . After polymerization single bonds are formed, resulting in  $sp^3$  hybridization and tetrahedral bond angles of approximately  $109.5^\circ$  for all the bonds. There are huge numbers of shapes which a polymer chain can assume. For example, in crystalline polyethylene chains, the carbon atoms are arranged in a planar zig-zag pattern. This shape is known as the all-trans conformation. The structure of a polymer chain has a profound influence on the structure of the solid it forms as well as the resulting properties of the material. In addition, the symmetry of the molecule affects which vibrational modes will be active in the infrared or Raman spectra. For these reasons, it is worthwhile to look into the structure of a polymer chain in more detail. For this purpose looking into the structure a small organic molecule, butane is helpful. Butane has the chemical formula  $C_4H_{10}$ . When viewing along the central C-C bond, the other two C-C bonds form an angle with each other known as the dihedral angle. The potential energy of a butane molecule is a function of the dihedral angle between the first and third C-C bonds as is shown below in figure 1.11. The potential energy has a global minimum near  $180^\circ$ , and two local minima near  $\pm 60^\circ$ . The molecules will be found in one of these minimum energy configurations. The  $180^\circ$  value leads to the conformation called the trans-conformation. The  $\pm 60^\circ$  conformations are known as gauche conformations. Three-dimensional structures of the two conformations of butane are shown in Figure 1.12. These diagrams can be extended to polymer chains as well. Each new bond after the second will adopt either a trans or gauche conformation. The potential energy graph for polyethylene appears similar to that for butane [30], therefore, chains in the crystalline regions of polyethylene tend to adopt an all-trans configuration. The potential energy diagram for each individual polymer will depend on the nature of their side groups.

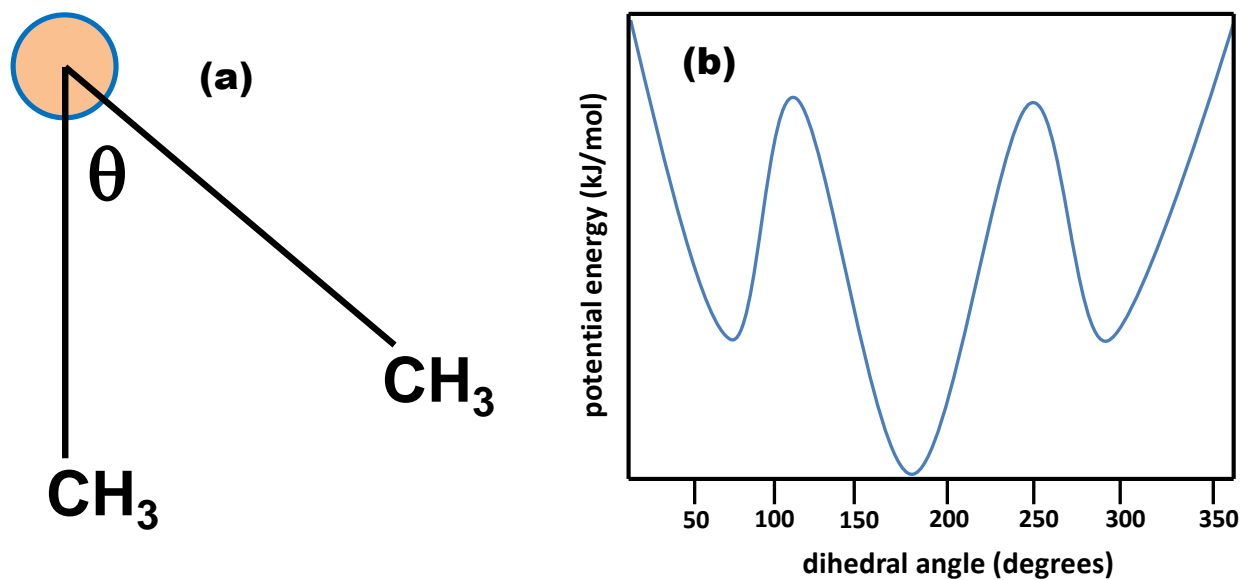


Figure 1. 11. (a) Definition of dihedral angle. The circle indicates the axis of the central C-C bond, which is perpendicular to the page (b) Potential energy diagram for butane as a function of the dihedral angle. The graph is adapted from Cowie [30].

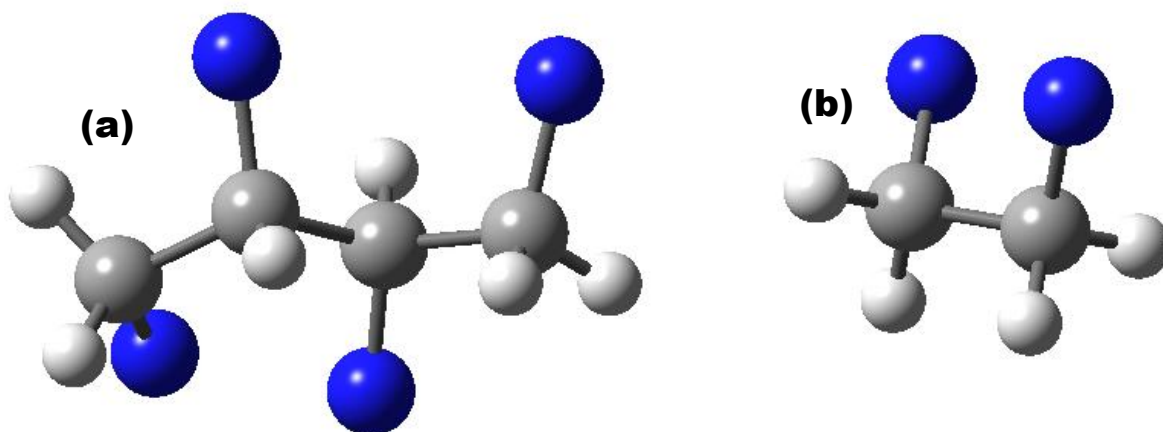


Figure 1. 12. Structure of (a) trans and (b) gauche butane. Here the carbon atoms are shown in grey while hydrogen atom and  $\text{CH}_3$  group are shown by light grey and blue, respectively.

Another important aspect of polymers is their configuration. For many polymeric materials, the monomer is of the form  $\text{CH}_2 = \text{CXY}$ , where Y is not H. These polymers are known as vinylidene polymers if X is not H and vinyl polymers if X is H [31]. If the polymer chain is

stretched out to an all-trans conformation, some of the Y groups will appear above the carbon backbone plane, while others will appear below. If all the Y groups are on one side of the plane, the polymer is isotactic. If the Y groups regularly alternate sides, the polymer is syndiotactic. Finally, if the Y groups are randomly arranged, the polymer is atactic [30]. Isotactic and syndiotactic polymers are assumed to be stereoregular. The tacticity of a polymer has a strong influence on the way the polymer chains pack into a solid. The atactic polymers tend to be amorphous, as they have trouble into packing in a regular structure. Isotactic and syndiotactic polymers tend to be crystalline since they have a regular structure [30]. There is also a connection between the configuration of a polymer chain and the conformations these chains adopt. The isotactic polymers generally avoid all-trans configurations since this leads to large steric strains when bulky substituents overlap [30]. Often these molecules adopt regular helical structures in the crystalline state. Syndiotactic polymers tend to occur in all-trans configurations, because substituents are already separated spatially [30].

As an example of structures of polymers, it is useful to compare the structures of polyethylene, polytetrafluoroethylene, and poly (vinylidene fluoride). Polyethylene adopts an all-trans configuration. Poly (tetrafluoroethylene) is in a nearly all-trans configuration, with dihedral angles of  $165.8^\circ$  [32], [33] at the room temperature phase IV. The bond varies little from a strict  $180^\circ$  dihedral angle because of steric strain between overlap of fluorine atoms on alternating carbon atoms. Since fluorine has a larger Vander Waals radius than hydrogen, so the fluorine atoms twist in the chain to reduce the overlap. It thus forms a helical structure. The most common form of poly (vinylidene fluoride), the  $\alpha$  phase, has at TGTG\* conformation, which denotes alternating trans and gauche bonds, where alternating gauche bonds twist in different

directions, as indicated by the asterisk. The structures of these different polymers are shown below in Figure 1.13.

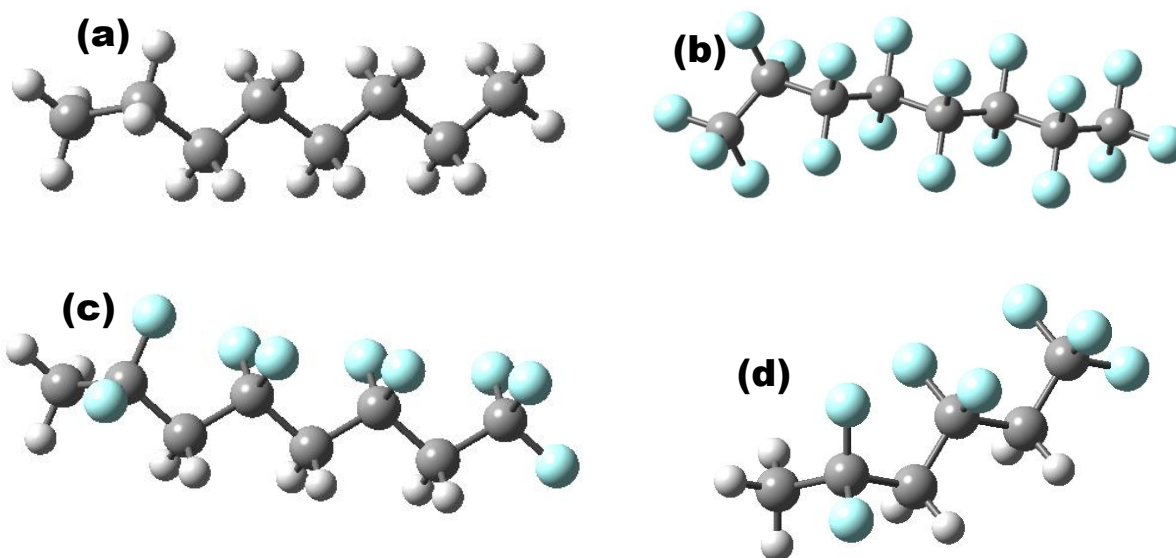


Figure 1. 13. Structure of the chains of (a) polyethylene, (b) poly (tetrafluoroethylene), and (c and d)  $\alpha$ -and  $\beta$  -PVDF. Carbon atoms are shown in grey while hydrogen and fluorine atoms are shown in light grey and blue, respectively. The structure of poly (tetrafluoroethylene) is similar to that of polyethylene except that it has a slight twist due to the dihedral angle changing from  $180^\circ$  to  $165.8^\circ$  for the room temperature phase IV [32], [33].

### 1.11. Crystalline and Amorphous Polymers

In the solid state, organic polymers are characterized by two different types of bonding. The chains are bound together in a solid by intermolecular forces such as weak Vander Waals forces (induced dipole-dipole interactions), or possibly by stronger forces such as hydrogen bonding [34]. The covalent bonds are responsible for the intramolecular bonds in a polymer chain. The form chains will take in a solid depends on these forces as well as the conformation and configuration of the chains. There are two main types of domains that the chains can occupy in a solid: amorphous and crystalline. Polymeric materials generally consist of a mixture of these

two types of domains, thus said to be semi-crystalline. The fractional crystallinity of polymeric materials can span a large range, however, there is at least a small amount of amorphous content [35].

Polymers tend to exist in the crystalline phase if it is a phase of minimum Gibbs free energy  $G = U + PV - TS$ , where  $U$  is the potential energy,  $P$  the pressure,  $V$  the volume,  $T$  the temperature, and  $S$  the entropy [30]. In determining the phase of polymer there is competition between energetic and entropic considerations. Whether or not the crystalline phase is favored it depends on the relative magnitude of these two effects and the temperature [30]. Crystallization packed the molecules more closely, so, it tends to decrease the potential energy of the system, but it also creates order which lowers the entropy. The more symmetric polymer chains tend to form crystalline polymers. Polymer chains which are stereoregular are easier to pack into an ordered lattice structure, and thus tend to be crystalline. Since it is more difficult for atactic polymers to be incorporated into a regular lattice hence, they tend to be amorphous [30].

Polymer crystals generally form lamellar structures, where the chains have linear conformations in the crystalline regions. The crystallites are plates where the chain axes are perpendicular to the plates. Generally, a single polymer chain is longer than the thickness of the plate, so it will be necessary for the chains to fold repeatedly and reenter the same crystallite or others for high crystallinities to be obtained. Typically these lamellae are part of larger structures called spherulites. Spherulites are made of many sets of parallel lamellae separated by amorphous regions [35]. These lamellae radiate outward in a spherical pattern from a central nucleus [30]. Polyethylene crystallites consist of all-trans configurations inside the crystal, while outside the crystal there are gauche bonds to facilitate reentry [30].

Opposite to crystalline domains, amorphous regions of polymers chains do not adopt a regular structure and a significant portion of their volume is occupied by free space. Since the chains are randomly shaped and distributed in amorphous polymers, there is inefficiency in their packing, i.e., the Vander Waals radii of adjacent atoms in different chains do not necessarily touch [30]. Amorphous polymers have different properties compared to crystalline properties. They have a phase transition known as the glass transition. Below the glass transition temperature, the chains as a whole are locked into rigid positions. Above the glass transition, however, the chains themselves can move around [30]. Below the glass transition temperature, polymers tend to be hard and brittle, while above this temperature they become rubbery. Above the glass transition temperature the amount of free volume in the sample begins to increase and this provides the polymer chains room in which they move. The glass transition affects many properties of a polymer, causing properties such as the refractive index and heat capacity to experience sudden increases or decreases [30]. Even below the glass transition temperature, polymers still may have localized segmental motion occurring [30]. The structure of the polymer chains has a strong effect on the glass transition temperature. Factors which increase the ability of polymer chains to move lower the glass transitions temperature [30], [36]. A flexible polymer backbone allows easier motion, while a stiffer backbone restricts motion. For example, benzene rings along the backbone tend to stiffen the structure and lead to a high glass transition temperature. Large side groups also increase the glass transition temperature by inducing steric restrictions to motion. Atactic and syndiotactic polymers generally have larger glass transition temperatures since the alternating side groups are lock together. For example, isotactic poly (methyl methacrylate) has a glass transition temperature of 318 K, while atactic and syndiotactic PMMA have glass transition temperatures of 378 and 388 K, respectively [30]. Crosslinking also

locks the polymer chain into more rigid structures and increase the glass transition temperature [30], [36].

The free volume of a polymer is also an important property. There are different theories that are used to describe the free volume in a polymer. One of these theories is called the free volume theory [30], [36]. It focuses on the effects of increasing free volume of the polymer sample above the glass transition temperature, but does not describe the details of the chain motion itself. Another theory, the Gibbs-DiMarzio theory, which considers the details of the molecular chain motion by considering the different conformations the chains can take [30],[36]. Sperling [36] discusses the effects of pressure on the glass transition temperature of a polymer. The fractional free volume in a polymer,  $f_{t,p}$  is given by the equation

$$f_{t,p} = f_0 + \alpha_f [T - T_g(0)] - \beta_{fp} \quad (1.8)$$

where  $f_0$  is the fraction of free volume at the glass transition temperature at zero pressure,  $\alpha_f$  is the volume expansion coefficient of the free volume,  $T_g(0)$  is the glass transition temperature at zero pressure, and  $\beta_{fp}$  is the free-volume compressibility. At particular pressure, the glass transition occurs at a temperature where  $f_{t,p} = f_0$  and it can be shown that

$$\frac{\partial T_g(p)}{\partial P} = \frac{\beta_f}{\alpha_f} \quad (1.9)$$

The glass transition temperature rises quite rapidly with pressure. For example, PMMA at low pressures, the glass transition temperature rises at a rate of 20 K/kbar [36]. Optically, many amorphous polymers such as poly (methyl methacrylate) and polycarbonate (PC), are highly transparent [30]. In other semi-crystalline polymers such as polyethylene and polytetrafluoroethylene, the crystallites size is generally comparable to the wavelength of light. Hence, these crystallites scatter light to a significant degree, resulting in materials that appear white.

## 1.12. Fundamental of Raman Spectroscopy

Raman spectroscopy is one of the most widely used and versatile techniques for studies of materials under extreme conditions such as under shock compression [37]. The Raman spectroscopy also has an advantage that it provides a large amount of easily analyzable information very rapidly. It probes elementary excitations in materials by utilizing inelastic scattering processes using near ultraviolet, visible or near infrared monochromatic light source. The recorded Raman spectra can be utilized to characterize the vibrational, electronic and magnetic subsystems by observing the corresponding elementary excitations. It can also be used as a finger–printing technique for analyzing the materials. By in situ spectroscopy one can observe the changes in the Raman spectra with application of pressure. These changes may be in the form of vibrational excitations, phase transformations (including melting), chemical reactivity and magnetic and electronic transitions. Raman scattering in crystalline solids can be used to probe phonons.

In the Raman spectroscopic studies of crystalline solids, features of Raman spectra such as Raman shift, line shape, intensity and polarization are useful to deduce information regarding the system under study. Raman spectroscopy has been used extensively for investigation of polymeric materials at various shock conditions [11], [15], [38]–[40]. It is very sensitive to local changes hence Raman spectroscopy has proven to be an important tool to probe polymeric materials and provide information about structural changes. Pressure dependent Raman spectroscopy is also helpful to estimate the isothermal Grüneisen parameter for Raman modes. Raman scattering is the inelastic scattering of electromagnetic radiation due to elementary excitations in a medium such as molecular vibration, phonon, polariton or magnon etc. Light scattered due to Raman scattering contains two components, one of which has frequency less

than the incident frequency, is called as Stokes component and the other which has frequency more than the incident is called as anti–Stokes component.

In the classical description of Raman scattering, both the medium and the incident electromagnetic radiation are assumed to be continuum. The incident radiation of electric field  $E(\nu)$  induces the polarization in the crystal system [41], [42].

$$\mu_i = \chi_{ij}E(\nu) \quad (1.10)$$

$$E(\nu) = E_0 \cos(2\pi\nu_0 t) \quad (1.11)$$

where,  $\mu_i$  is the induced dipole moment and  $\chi_{ij}$  is the electrical susceptibility.

Electrical susceptibility is a second rank tensor which describes the response of the crystal lattice to the incident electric field. Electrical susceptibility is a function of lattice vibration; it can be expanded in Taylor series using normal coordinate as follows,

$$\chi_{ij} = \chi_0 + \sum_k \left( \frac{\partial \chi_{ij}}{\partial Q_k} \right)_{Q_k=0} Q_k + \sum_{k,l} \left( \frac{\partial^2 \chi_{ij}}{\partial Q_k \partial Q_l} \right)_{Q_{k,l}=0} Q_k Q_l + \dots \quad (1.12)$$

where  $Q_k$  is normal coordinate for  $k^{\text{th}}$  normal mode of vibration, which is responsible for first order scattering. While second and other higher order effects are represented by higher order terms in equation (1.12).

Normal modes are harmonic in nature, hence it can be given as follows

$$Q_k = Q_{k0} \cos(2\pi\nu_m t) \quad (1.13)$$

Substituting equation (1.13) into equation (1.12) we get

$$\chi_{ij} = \chi_0 + \sum_k \left( \frac{\partial \chi_{ij}}{\partial Q_k} \right)_{Q_k=0} Q_{k0} \cos(2\pi\nu_m t) + \dots \quad (1.14)$$

Replacing  $\chi_{ij}$  and  $E(\nu)$  in equation (1.10) by using the values from equation (1.14) and (1.11) gives,

$$\mu_i = \chi_0 E_0 \cos(2\pi\nu_0 t) + \frac{1}{2} \left( \frac{\partial \chi_{ij}}{\partial Q_k} \right)_{Q_k=0} Q_{k0} E_0 [\cos(2\pi\{\nu_0 - \nu_m\}t) + \cos(2\pi\{\nu_0 + \nu_m\}t)] \quad (1.15)$$

First term on right side of equation (1.15) denotes the Rayleigh scattering (elastic). Second and third term denotes Raman Stokes and anti-Stokes scattering respectively. From equation (1.15), we can also infer that normal mode of vibration for which electrical susceptibility changes can only be Raman active. We get the selection rule for Raman scattering as follows,

$$\left( \frac{\partial \chi_{ij}}{\partial Q_k} \right)_{Q_k=0} \neq 0 \quad (1.16)$$

$\left( \frac{\partial \chi_{ij}}{\partial Q_k} \right)_{Q_k=0}$  is the derived susceptibility tensor, also called as Raman tensor. For individual mode of vibration, it is written in the form of  $3 \times 3$  matrix. For Raman active modes, it should have at least one non vanishing component in the matrix.

Classical theory can successfully explain the occurrence of Stokes and anti-Stokes Raman frequencies. It also explains correctly the dependence of Raman scattering on derived susceptibility. However classical theory has some limitations for example, it cannot explain rotational Raman spectra. Classical theory also cannot explain the difference in the intensities of Stokes and anti-Stokes Raman frequencies. Therefore quantum mechanical treatment is needed to get further insights into Raman scattering. Energy level diagram for the Raman scattering process is shown in Figure 1.14. In Rayleigh scattering, incident photon  $\omega_i$  takes the system from ground state energy level to some intermediate virtual state and brings back again into ground state, during which energy is neither transferred nor absorbed. In the case of Rayleigh scattering process, incident and scattered photon has same frequency viz.  $\omega_s = \omega_i$ . In the Stokes Raman scattering, incident photon ( $\omega_i$ ) takes the system from ground state energy level to first excited state through some intermediate virtual state, during which phonon of energy  $\omega_l$  is getting created. In the Stokes Raman, scattered photon has the frequency is  $\omega_s = \omega_i - \omega_l$ . While in the

case of anti-Stokes Raman scattering, incident photon  $\omega_i$  brings back the system from excited state to ground state through some intermediate virtual state and annihilates the phonon of energy  $\omega_l$ . In the anti-Stokes Raman, scattered photon has the frequency is  $\omega_s = \omega_i + \omega_l$ .

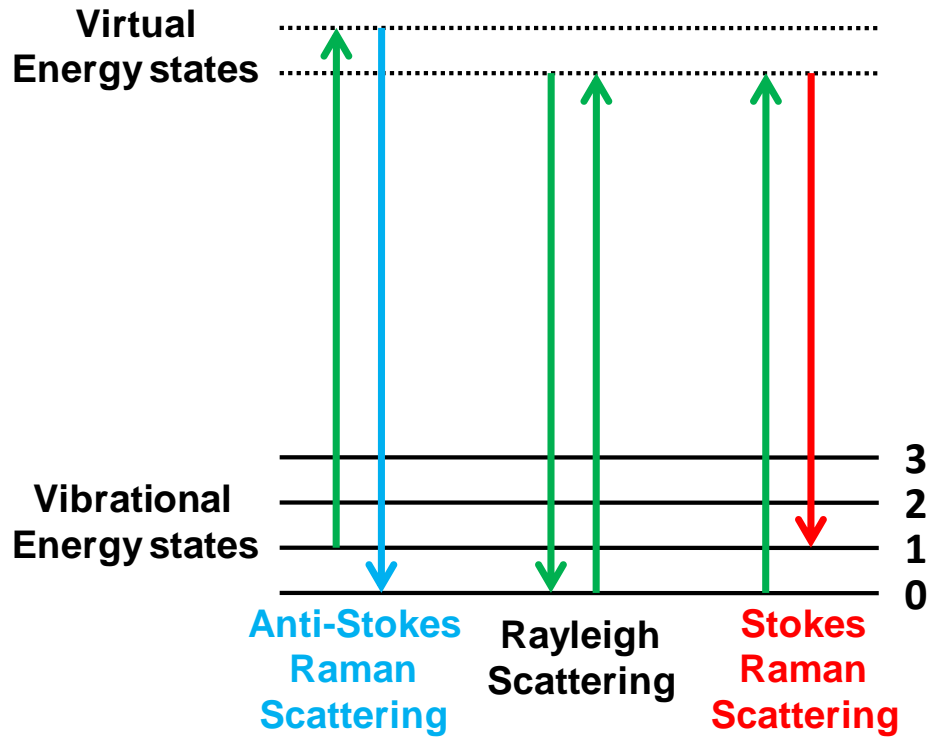


Figure 1. 14. Energy level diagram for Raman Scattering

In quantum mechanical treatment of Raman scattering, time dependent perturbation theory is used [41]. In quantum mechanical description of Raman scattering, an incident photon interacts with the system and take it from initial state  $|i\rangle$  to an intermediate state  $|r\rangle$ . Followed by creation or annihilation of elementary excitation such as phonon which is corresponding to processes such as Stokes or anti-Stokes respectively. Process ends with transition of a system from intermediate state  $|r\rangle$  to final state  $|f\rangle$ . Time scale of the whole of this process is limited by Heisenberg uncertainty. Transition susceptibility [41] is given as

$$(\chi_{ij})_{fi} = \frac{1}{\hbar} \sum_{r \neq i, f} \left\{ \frac{\langle f | \hat{P}_i | r \rangle \langle r | P_j | i \rangle}{\omega_{ri} - \omega_l} + \frac{\langle f | \hat{P}_j | r \rangle \langle r | P_i | i \rangle}{\omega_{rf} + \omega_l} \right\} \quad (1.17)$$

where  $\omega_{ri} = \omega_r - \omega_i$  and  $\omega_{rf} = \omega_r - \omega_f$ ;  $\omega_i$  is the frequency of incident photon,  $\omega_f$  is the frequency of scattered photon,  $\omega_r$  is frequency at intermediate state  $|r\rangle$ ,  $\omega_l$  is the phonon created or annihilated in the Stokes or anti-Stokes Raman scattering process respectively. The results of the quantum mechanical treatment are similar to that of classical treatment; however susceptibility is defined in terms of wave functions and energy levels of the system, which enables in determining the properties of scattering system from the analysis of scattered photon. Intensity of Stokes and anti-Stokes Raman scattering is proportional to the population of phonons, given by Bose-Einstein distribution function. Ratio of intensity of Stokes to anti-Stokes scattering for phonon mode  $\omega_l$  is given as

$$\frac{I_s}{I_{AS}} = \left( \frac{\omega_i - \omega_l}{\omega_i + \omega_l} \right)^4 \exp\left(\frac{\hbar\omega_l}{k_B T}\right) \quad (1.18)$$

As the temperature increases the anti-Stokes intensity increases as compared to Stokes.

During the scattering process, incident photon exchanges energy and momentum with scattering medium and inelastic scattering follows the law of conservation of energy and momentum as follows,

$$\hbar\omega_i = \hbar\omega_s \pm \hbar\omega_l \quad (1.19)$$

$$\hbar\vec{k}_i = \hbar\vec{k}_s \pm \hbar\vec{q}_l \quad (1.20)$$

‘+’ and ‘-’ sign denotes creation and annihilation of phonon respectively or can be referred as Stokes and anti-Stokes scattering process respectively.  $(\hbar\omega_i, \hbar\vec{k}_i)$  and  $(\hbar\omega_s, \hbar\vec{k}_s)$  is the energy and momentum of incident and scattered photon respectively.  $(\hbar\omega_l, \hbar\vec{q}_l)$  is energy and momentum of 1<sup>th</sup> phonon mode. Figure 1.15 shows the creation and annihilation of phonon.

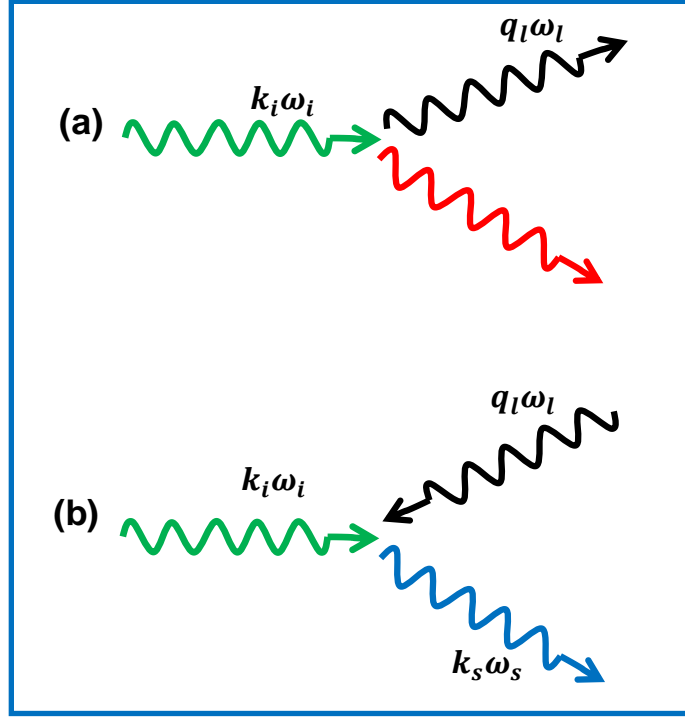


Figure 1. 15. (a) Creation of photon corresponding to stokes scattering (b) Annihilation of photon corresponding to anti–Stokes Scattering.

For  $180^\circ$  backscattering geometry; maximum allowed value of  $q$  related to  $k_i$  and  $k_s$  can be obtained as

$$q_{max} = k_i + k_s \approx 2k_i \quad (1.21)$$

Phonon can have any value of wave vector in the Brillouin zone. Maximum value of wave vector at the zone boundary is of the order of  $10^8 \text{ cm}^{-1}$ , which is much larger than wave vector of  $k_i$  for visible range which is of the order of  $10^5 \text{ cm}^{-1}$ , hence only phonons from Brillouin zone centre ( $q = 0$ ) are allowed in Raman scattering process in crystals. However in the case of solid solution, nano or amorphous materials, due to the lack of translation symmetry, non–zone centre phonons can also contribute for Raman scattering.

### 1.13. Motivation for the present work

Investigations of response of materials under dynamic loading (such as the equation of state (EOS) and strength) rely on experiments in which a well characterized load is applied and the response is measured. Most of these experiments have employed shock waves, induced by projectile impact or the detonation of the chemical explosives which is of microsecond time scale. High power solid state laser has become a very vital tool for the studies of the materials behavior under fast (few nanosecond) and very high pressure dynamic loading. Various shock diagnostics such as optical streak camera, optical shadowgraphy, interferometer, X-ray shadowgraphy/backlighting etc. have been developed to measure shock velocity and particle velocity and hence the EOS of the materials. Such diagnostics are being used to measure the materials behavior at the final stage. To study the materials behavior under shock at atomic/molecular level ‘time resolved Raman spectroscopy/X-ray diffraction of shocked material’s are the best suitable diagnostics. The time-resolved Raman spectroscopy is a powerful tool to investigate dynamics of the molecules, molecular structural changes, and bond strength etc. Thus chemical or structural changes can be monitored which can give direct information of the initiation and decomposition mechanisms occurring at the molecular levels under shock compression. The time resolved Raman spectroscopy enables us to study various parameters under extreme conditions such as

- Time resolved and microscopic measurements of matter at molecular level (in order to understand the excitation and relaxation processes of matter induced by applying an impulse of high pressure or shock waves)
- Chemical and physical changes under the shock compression

- Identifying the transient intermediates in the fast reactions, analyzing their bonding and structure. Also monitoring their kinetics of formation and decay.
- The structural changes of the molecules and phase transitions under extreme conditions

Due to their complexity and adoption of different conformations, polymeric material exhibits several interesting phenomenon. With the increase in pressure some semi crystalline polymers show solid-solid phase transition. The intermolecular and intra-molecular interactions inside polymeric materials can be altered under pressure. These altered properties may provide new pathways to produce novel properties in polymers that are distinct from conventional synthesis methods. Moreover, it is important for the polymer industries to explore pressure induced polymer products with improved, advanced and distinct properties from that obtained using conventional synthetic methods. In addition, polymers also have potential application as an energetic material. The interactions of energetic materials and polymers have important implications in safety, long-term storage, and performance of explosives and explosive mixtures. In the present thesis, extensive work is carried out using in house developed time-resolved Raman spectroscopy facility on the selected polymers to measure their EOS and to understand the fundamental processes these materials undergo under extreme conditions.

## **Chapter 2. Development of in situ time-resolved Raman spectroscopy facility for dynamic shock loading in materials**

### **2.1. Introduction**

In the present thesis work, time resolved Raman spectroscopy facility has been developed, and used as a main technique to investigate physical and chemical properties of different types of polymers under different shock conditions. The experimental facility consists of mainly three parts; high power pulsed laser system, confinement geometry target assembly, and detection and data acquisition system, which will be briefly discussed in the next section. This chapter present development of time resolved Raman spectroscopy facility at Laser shock laboratory, HP&SRPD, BARC to study the behavior of materials under laser driven shock compression. The time resolved Raman spectroscopy facility is optimized by using carbon tetra chloride ( $\text{CCl}_4$ ) as sample. The measurements of this chapter has been published in the Journal of instrumentation [43].

### **2.2. Laser system for pump and probe beam**

The time resolved Raman spectroscopy of shocked materials requires a laser system with narrow bandwidth, small pulse to pulse energy variation and electronic jitter, as several diagnostics are synchronized to detect the pulsed event over several numbers of laser shots, and good spatial and temporal profile. For this a 2 J/8 ns Nd: YAG laser system operated in Q-switched mode has been used. The laser system designed in such a manner that it can deliver two laser beams simultaneously: one at fundamental wavelength (1064 nm) and other at second harmonic (532 nm). The pulse energy in both the beams can be adjusted by tuning some of the optics inside the laser system. Here for the Raman spectroscopy of shocked materials, the maximum laser energy used in fundamental mode is approximately 1.6 J (used for shock

generation) and in second harmonic beam is approximately 10 mJ (to produce the Raman scattered light from the samples). The pump and probe beam energy is adjusted on the sample with the help of laser control system and neutral density filters.

### **2.2.1. Characterization of laser parameters**

The spatial profile of the laser beam is near hat top with only 20% variation in the intensity of the top 80% of the beam as shown in figure 2.1 (a). Such a beam profile is good for the generation of steady shock wave in the sample. The laser pulse duration of the laser beam is measured as 8 ns with the help of fast photodiode (from M/s Alphalas) having rise time of 40 ps and a 2.5 GSa/s oscilloscope (from M/s Agilent technologies) and is shown in figure 2.1 (b).

Raman spectroscopy techniques are employed for the analysis of rotational, vibrational, and other low frequency modes in a molecular system. The interaction of the light with the system causes shifting up or down of the energy of the laser photons. This shift in energy provides data about the molecular bonds and thereby the molecule itself. The resolution of the Raman system is limited by the bandwidth of the excitation beam, with lower bandwidths generating higher resolution. The present laser system is single longitudinal mode with theoretically calculated bandwidth of  $0.02 \text{ cm}^{-1}$ . The spectral measurements are performed using available High Finesse WS5 wavelength meter which is having resolution of  $0.1 \text{ cm}^{-1}$ , (3000 MHz) for 1064 nm wavelength. The measurement is shown in figure 2.1 (c), which indicates that the bandwidth of the laser is  $< 0.1 \text{ cm}^{-1}$ . Here the horizontal (x) axis of the graph in figure 2.1 (c) represents the pixel number of the CCD line-array and the vertical (y) axis is the voltage of every single chip in mV. The graph therefore is the direct reproduction of the interferences pattern focused on the array.

The time resolved Raman spectroscopy of laser shocked materials experiments required accumulation of several hundreds of shot for one data point due to very short time exposure (a few hundreds of picosecond to a few nanosecond), so, stability in the laser energy is very important parameter. The pulse to pulse energy variation measured for different energy range is  $< 0.2\%$ , and is shown in figure 2.1(d).

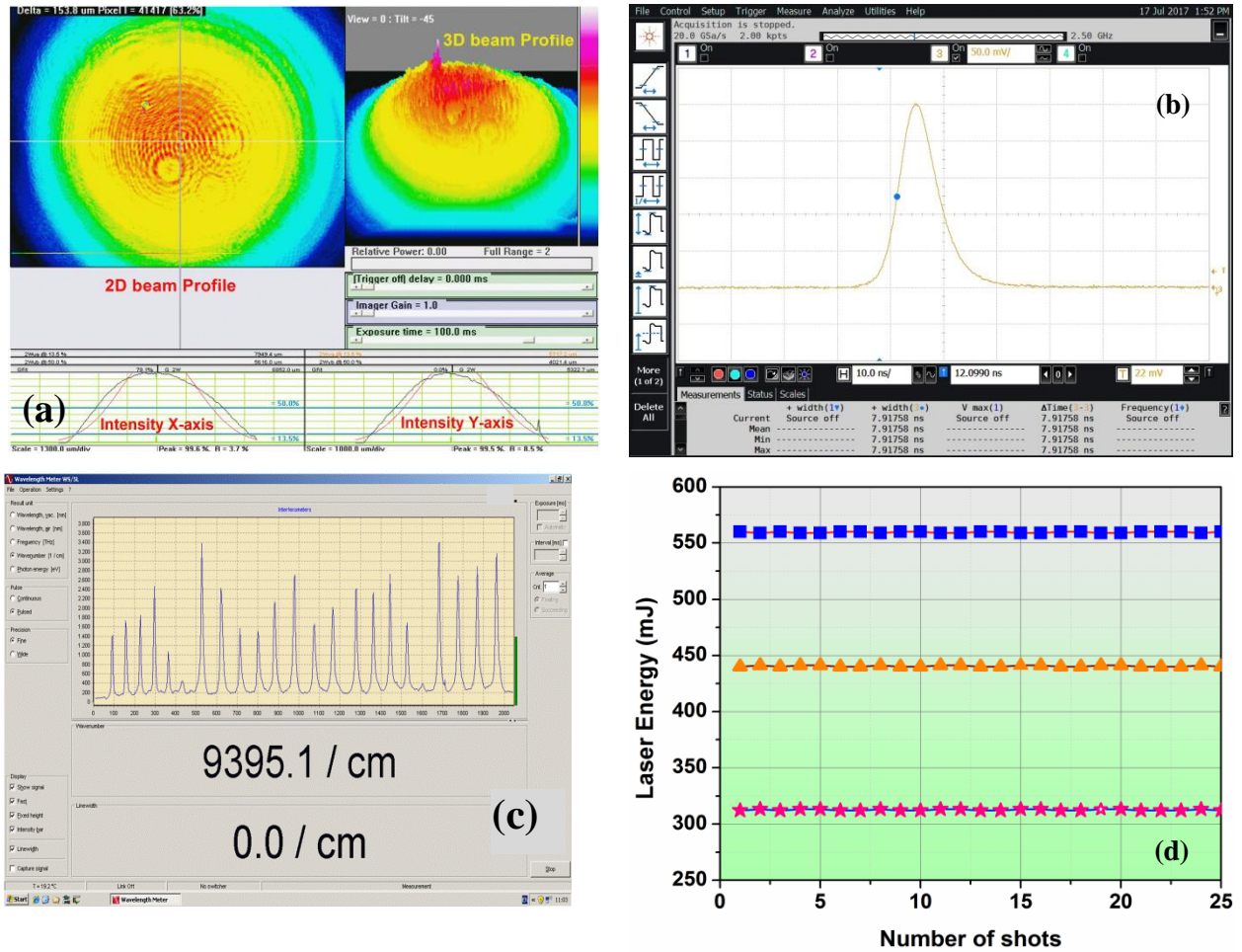


Figure 2. 1. (a) Pump laser beam profile used for shock generation in Al-foil measured with the beam profiler. The beam profile of the laser beam is super Gaussian in spatial domain, (b) temporal profile of the laser pulse, (c) spectral width of the laser beam measured with the wavelength meter and (d) laser energy reproducibility or fluctuation with shot number ( $< 0.2\%$ ).

### 2.3. Confinement geometry target assembly

Mostly, the time resolved Raman spectroscopy experiments of laser shocked materials are done in open environment. Where the limiting factor is dielectric breakdown of the air at higher laser intensities, which is directly proportional to ablation pressure. The only way to enhance the pressure keeping laser intensity well below the break down limit of air is to modify the target geometry. Anderholm et al. [44], proposed a scheme of the confinement geometry target assembly for the enhancement of the shock pressure inside the sample. In this scheme the confinement of plasma is done between the glass and the Aluminum foil glued on the glass. This plasma confinement with solid block enhances the amplitude and duration of shock by several times in comparison to direct ablation scheme. Such geometry is a pressure booster in the studies of time resolved Raman spectroscopy of shocked material.

Devaux et al. [45] had studied different physical processes involved in the laser produced plasma in confined geometry. They developed an analytical model to describe the laser–matter interaction in this geometry. The model is mainly based on two hypotheses: (i) Plasma is formed at the interface between the target and the dielectric. Two shocks are generated by the plasma in these two mediums. Behind the shock wave front, the matter moves at fluid velocity, given by the well-known relation  $P=Zu$ , where  $P$  is the pressure of the shock front,  $Z = \rho_0 U_s$  ( $\rho_0$  - initial density of the material;  $U_s$  - shock velocity in the material) is the shock impedance of the material and  $u$  the fluid velocity. The displacement of the interface walls opens the interface, and induces the adiabatic cooling of the plasma. (ii) The plasma is taken as a perfect gas, but with a correction factor and written as:  $\alpha U = 3/2kT$ , where  $U$  is the internal energy,  $k$  the Boltzmann constant,  $T$  the temperature of the plasma and  $\alpha$  is corrective factor.

Using these two hypotheses and the conservation of energy and momentum, the maximum pressure of the plasma  $P$  (kbar) is calculated by the below relation [45]:

$$P(GPa) = 0.01 \sqrt{\frac{\alpha}{2\alpha+3}} \sqrt{Z} \sqrt{I(GW/cm^2)} \quad (2.1)$$

where  $Z$  is the reduced shock impedance between the two materials and  $I$  is the flux of the laser beam. Here the expression does not depend on the laser pulse duration.

In this geometry, the limiting factor for ablation pressure is damage threshold of the optical glass [45]–[48]. The dependencies of these optical glasses (dielectric) on laser parameters are needed to be investigated before making confinement geometry target. A thorough study on dependency of dielectric breakdown on laser parameters is performed and the discussions on related results are presented in chapter 3.

The target assembly used in our experiment consists of a cover glass ( $100 \times 100 \times 5 \text{ mm}^3$ ), a  $50 \text{ }\mu\text{m}$  thick Aluminum foil, a sample of required thickness, and a back-up glass ( $100 \times 100 \times 5 \text{ mm}^3$ ). An aluminum foil is glued to cover glass with an optically transparent adhesive and left at ambient conditions for 72 hours to cure the glue. This target assembly is mounted on a motorized X–Y–Z translational stage. The translational stage is synchronized with the laser pulse to get each shot on fresh target. The pump beam is focused on the Aluminum foil to generate laser induced plasma at the glass-Aluminum interface which generates a shock wave inside the Al-foil and drives a shock wave into the sample through Aluminum foil. The pressure in the sample is calculated by using impedance mismatch technique using Aluminum as a reference/standard material and obtained results are compared with 1D hydrodynamic simulation results. The schematic of the confinement geometry target assembly is shown in figure 2.2.

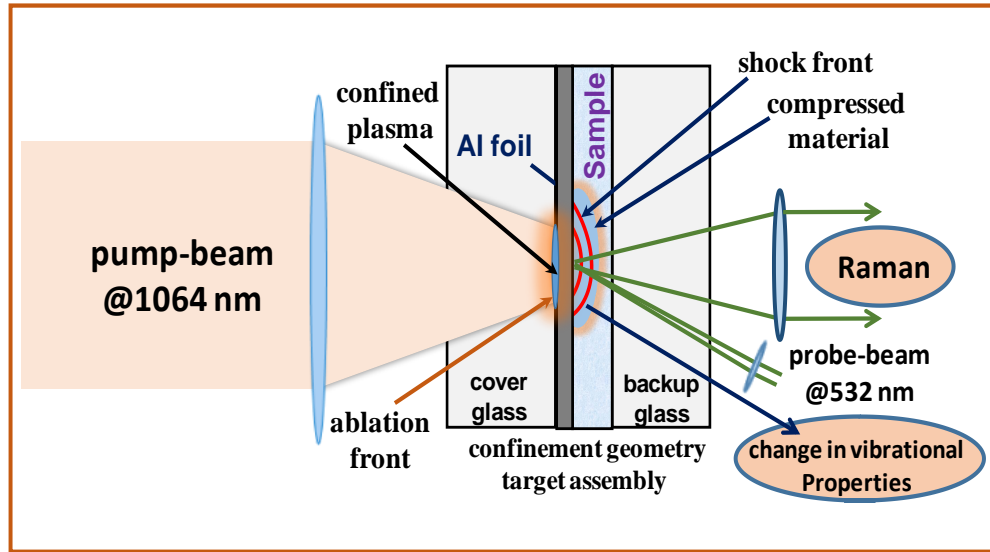


Figure 2. 2. Schematic drawing of the confinement geometry target assembly.

## 2.4. Detection System

The detection system consists of two parts (i) Raman Spectrometer (ii) fast gated ICCD camera. For our experiments, we have used 0.5 meter long Raman spectrometer, having holographic grating target with 600, 1200 and 2400 lines/mm. Figure 2.3 shows the schematic diagram of the Raman spectrometer. Here, S1, S2 are entrance and S3 is exit slits respectively, M1 and M2 are concave mirrors to reflect the signal towards grating G mounted on a cosecant drive, ICCD camera and exit slit S3 respectively. Scattered radiation enters through slit S1 and falls on mirror M1, which reflects parallel beam to grating G. Grating disperses the scattered signal, which is finally focused by mirror M2 towards ICCD camera slit. Slits and mirrors are in the same focal plane. As the grating is rotated with the help of cosecant drive, successive spectral regions appear at the ICCD camera slit. Total spectral range of the spectrometer is 200–1400 nm for 1200 groves. At 500 nm of wavelength with 1200 groves/mm grating and 500 mm imaging mirror focal length, the reciprocal linear dispersion of the instrument is  $\sim 2\text{nm/mm}$ , and the reproducibility of the spectra is within  $\pm 0.075\text{ nm}$ . For 100  $\mu\text{m}$  entrance slit width, spectrometer

resolution limited width is  $\leq 0.03$  nm with 2400 groves/mm. All the Raman experiments are carried out with 100  $\mu$ m entrance slit.

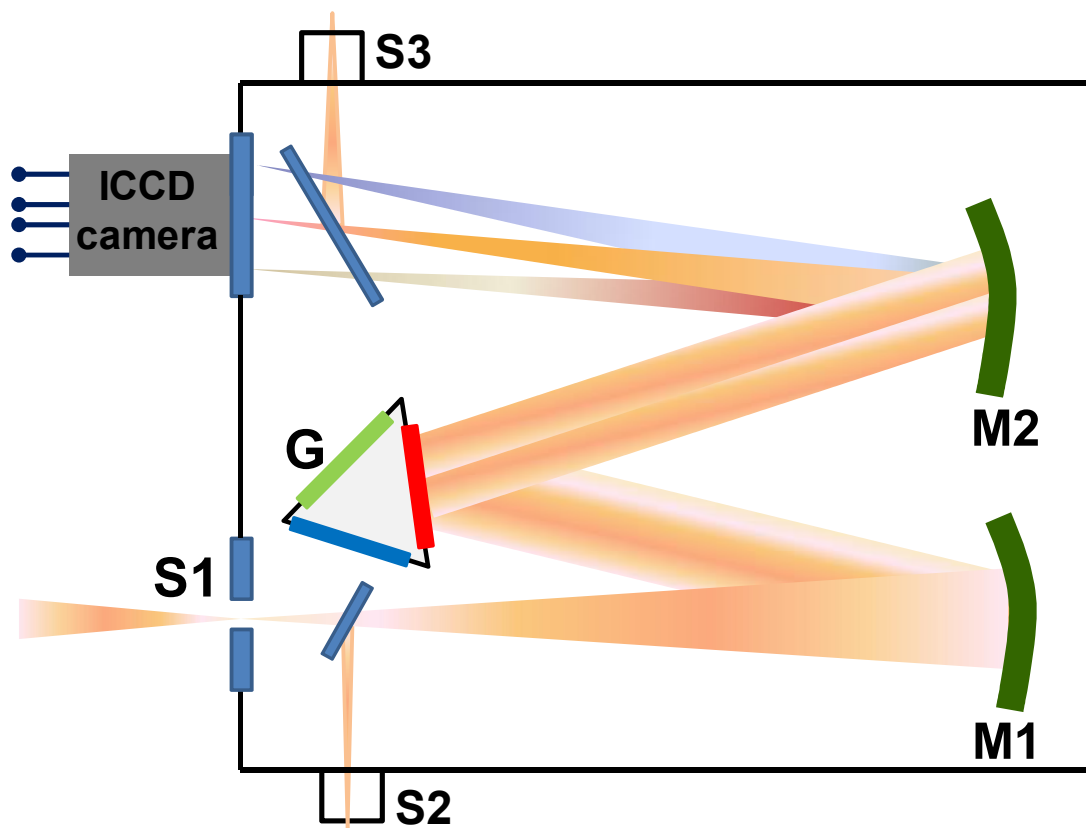


Figure 2.3. Schematic diagram of Raman spectrometer; where M1 and M2 are reflecting concave mirrors, S1, S2 are entrance and S3 is exit slits respectively; and G is holographic grating tarnet having 600, 1200 and 2400 groves.

Generally Raman instruments consists either photomultiplier based or charged coupled device (CCD) based detector system. Our Raman instrument has been coupled to air cooled intensified charge coupled device (ICCD) detector from ANDOR technology. Size of the ICCD image is  $2048 \times 512$  pixels. Size of each pixel is  $13\mu\text{m} \times 13\mu\text{m}$ . It has computer based integrated data acquisition system. All shock experiments on different polymers are carried out

using home built time resolved Raman instrument. The screen shot of the data acquisition system used for recording the data is shown in figure 2.4.



Figure 2. 4. Screen shot of the data acquisition system used for recording the data, taking  $\text{CCl}_4$  as a sample.

## 2.5. Static high pressure Measurement

To compare the shock compression results, the static Raman measurements are carried out using a triple stage Raman spectrograph (Jobin–Yvon T64000) equipped with a liquid  $\text{N}_2$  cooled open electrode CCD detector. The Raman scattering is excited with 532 nm diode pumped solid state laser and the sample is pressurized using in house developed diamond anvil cell (DAC). The sample along with a tiny chip of ruby for pressure calibration is loaded in a hole of  $\sim 100 \mu\text{m}$  diameter drilled in a pre-indented tungsten gasket to  $50 \mu\text{m}$ . No pressure transmitting medium is used here, which make the system quasi hydrostatic. However, polymer samples like PTFE, PVT, polystyrene etc. are very soft so the errors in the measured pressure and corresponding peak shift will be insignificant. The typical relative error in measurements of

pressure in hydrostatic environments using this high pressure system is about  $\pm 0.01$  GPa. The schematic of diamond anvil cell (DAC) with sample and pressure sensor is shown in figure 2.5.

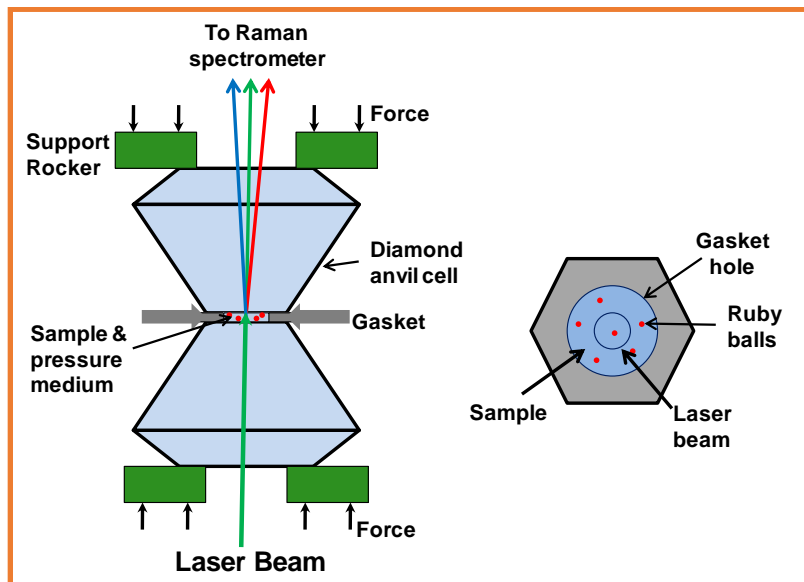
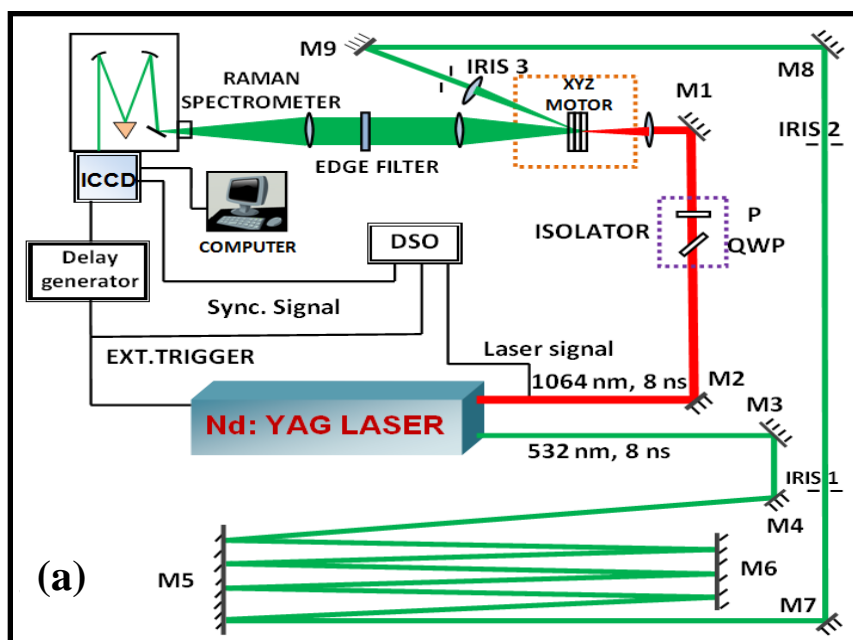


Figure 2. 5. Schematic of diamond anvil cell (DAC) with sample and pressure sensor.

## 2.6. Experimental arrangement for time resolved Raman spectroscopy

A time resolved Raman spectroscopy facility, based on pump-probe technique has been developed using pulsed lasers. The experimental arrangement is shown in figure 2.6 (a). The laser shock is generated by focusing fundamental beam (pump beam at 1064 nm, 1.6 J/8 ns) with a spot diameter of 2 mm, using a Q-switched Nd:YAG laser (Ekspla, NL120) on the target assembly. Whereas part of laser beam is converted into second harmonic (532 nm) for the probe beam. This second harmonic radiation ( $\sim 4$  mJ/5 ns) is focused to a spot size of 0.5 mm at the central area of the shocked region from backside. This will give advantage to measure the nearly flat shocked region and reduce the chance of error due to 2D effect because of Gaussian beam profile of the laser pulse. The Raman scattered signal is measured by a half meter Raman spectrometer with gated ICCD camera arranged in confocal geometry. The ultimate spectral and

temporal resolution of the Raman spectrometer coupled with ICCD camera are  $3 \text{ cm}^{-1}$  and  $1.2 \text{ ns}$  respectively for these experiments. However, for most of the experiments the temporal resolution is kept to  $3 \text{ ns}$  to get considerable amount of signal. The pump and probe beams on target and ICCD camera gate pulse are synchronized with the help of delay generator to get optimized signal. Each Raman spectrum is obtained by accumulating 300 laser shots. The Rayleigh scattered light is removed by using an edge filter, which enabled us to measure spectral range above  $200 \text{ cm}^{-1}$ . For best resolution and higher Raman signal, the set up is optimized using carbon tetrachloride ( $\text{CCl}_4$ ), as the Raman signal from the  $\text{CCl}_4$  is fairly large. For the best delay between Raman signal reaching on the spectrometer and opening of the ICCD gate pulse are done by changing the delay in the range of  $-5 \text{ ns}$  to  $+5 \text{ ns}$  around the fixed delay between pump and probe beams. The final delay is optimized by adding or subtracting the time for the best signal in the fixed time delays. The Raman mode of  $\text{CCl}_4$  liquid at  $218 \text{ cm}^{-1}$  (C–Cl symmetric stretching mode),  $314 \text{ cm}^{-1}$  (C–Cl asymmetric bending mode) and  $459 \text{ cm}^{-1}$  (C–Cl symmetric stretching mode) for various delay are shown in figure 2.6 (b) [49].



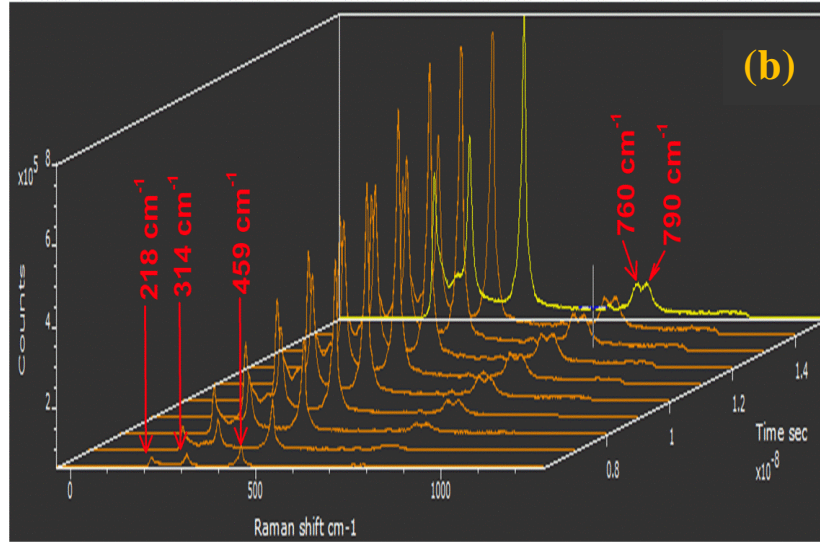


Figure 2. 6. (a) Schematic of the experimental setup; where  $M_{1-9}$  –reflecting mirrors; QWP–quarter wave plate; P–polarizer; DSO–digital oscilloscope; ICCD–intensified charge coupled device (b) Scanning of signal  $\text{CCl}_4$  for  $\pm 5$  ns around the set delay between pump and probe beams.

The delay between pump and probe beam is measured with the help of fast photodiode and a 2.5 Gs/s oscilloscope and is shown in figure 2.7 (a) (pink signal). The details of synchronization of the experiments i.e., SYNCH OUT pulse (Yellow square pulse), laser pulse recorded by inbuilt photodiode in the oscillator (blue), ICCD camera gating pulse (green) along with the pump and probe beams are shown in figure 2.7 (a). The delay between pump and probe beams is generated for more than hundred nanoseconds, by using two large size mirrors with maximum reflection at zero degree angle of incidence as shown in figure 2.7 (b). The delay in one round trip is  $\sim 7$  ns.

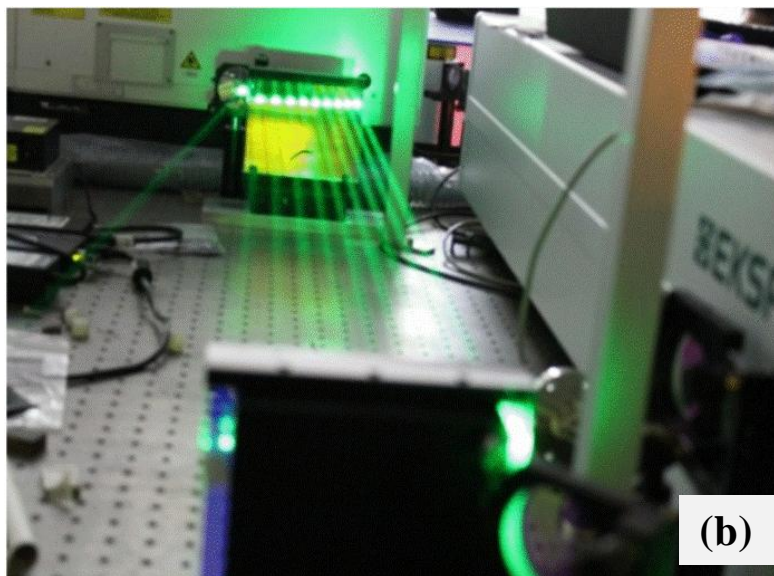
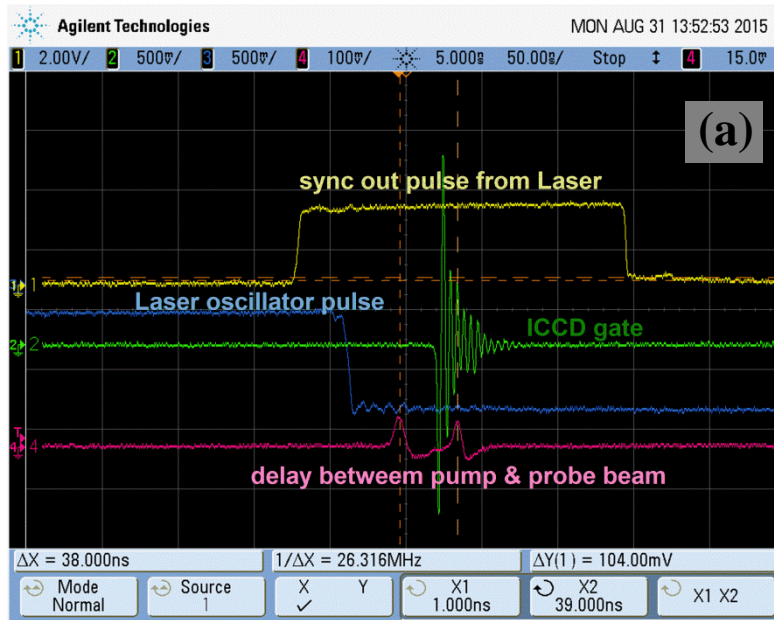


Figure 2. 7. (a) Synchronization of the set up using fast photo diode and digital oscilloscope, (b) photograph of multi pass delay generator.

## 2.7. Summary

In summary, time resolved Raman spectroscopy experimental facility has been developed using high power pulsed laser to study the behavior of materials under shock compression. Various components of the facility are optimized. The temporal and spectral resolutions of

system in best condition achieved are 1.2 ns and  $3 \text{ cm}^{-1}$  respectively. For best resolution and higher Raman signal, the set up is optimized using carbon tetrachloride ( $\text{CCl}_4$ ) and later the experiments are performed with the various samples. All the observed results indicate that the in situ time resolved Raman spectroscopy is an effective tool to investigate the shock induced changes inside a material.



## **Chapter 3. Investigation of damage mechanism in optical glasses used for making confinement geometry targets**

### **3.1. Introduction**

In the design of confinement geometry targets for shock studies, damage mechanism play an important role and is the main limiting factor for shock amplitude. This chapter describes damage threshold measurements of borosilicate glass used for making confinement geometry targets, and their dependency on laser parameters. Experimental results of numerous laser shots on glass are presented and analyzed. The laser induced damage studies in optical glasses are important for other applications also; such as laser micromachining, breakdown and excitation mechanism studies in optical components etc. [50]–[55]. The laser induced damage morphology by femtosecond to nanosecond lasers has been studied by several researchers [53], [54], [56]–[59]. However, surface morphology changes induced by laser pulses has not been yet fully understood. Lasers with pulse duration from femtosecond to nanosecond initiates inducing damage on the surface of optical component through breakdown, sputtering or ablation processes [55]. The dielectric material used for making confinement geometry targets requires low absorption of laser radiation and high laser damage thresholds. In this context various experimental techniques have been developed to understand the laser initiated damage phenomena [59]–[65]. The damage threshold is linked to many factors such as damage criteria, test procedure, spatial and temporal beam shapes, spot size, wavelength and number of shots. These large numbers of parameters makes comparisons, or compilations of results of several experiments, difficult. The measurements of this chapter have been published in an article by V. Rastogi et al. in *Journal of Non-Crystalline Solids* [66].

### 3.2. Damage threshold

When a high power laser pulse is incident on a transparent dielectric, no damage occurs unless the energy of the pulse exceeds a certain minimum threshold value known as the damage threshold of the material. Damage threshold studies have been made on a wide variety of glass targets and have indicated a material dependence on the condition of the surface of the glass (i.e. number of cracks, pores or scratches); polishing technique used in the production of the glass (etching or chemical used); and any heavy metal ion embedded in the glass surface (either as a strengthener or as an unwanted result of the manufacturing process). Additionally, the pulse length of the laser, and the transverse mode of the operation of the laser, has been shown to affect the surface threshold.

### 3.3. Causes of laser induced damaged phenomena

Many damage mechanisms are responsible for laser induced glass breakdown. Among them the two main mechanisms that causes laser induced dielectric breakdown and thermal absorption in dielectric materials are avalanche and multiphoton absorption [67]. Mostly dielectric breakdown occurs at surfaces. Since surface defects failure takes place at a lower power levels than one would expect from the bulk. Factors which significantly reduce the damage threshold on surface are scratches, pores, contamination and inclusions. Surface absorption due to material inclusion is usually caused by an adsorbing layer particulate matter or residual polishing compound. For long pulses ( $t_p > 100$  ps), the dominant mechanism for laser induced damage is electron avalanche and/or thermal absorption.

### 3.4. Experimental detail

Laser induced damage threshold measurement and tests are performed on a borosilicate glass. The schematic of the experimental setup for damage test is shown in figure 3.1. The damage threshold studies have been done for various laser parameters, such as pulse duration (500 ps and 8 ns), laser power density, number of shots at same place and wavelengths (1064 and 532 nm). A beam reflected by beam splitter is incident on energy meter EM1 to monitor the shot to shot energy variation of the incident laser beam. The incident laser beam is focused on front and rear surface of glass sample using a  $f/2$  focal length lens L. The effective, focal spot of the incident laser beam on the target is around 50  $\mu\text{m}$ . An energy meter EM2 (Ophir Vega) is placed behind the glass sample to record the percentage transmitted laser radiation from the back side of the glass sample. The damage measurement is done by using three diagnostics; a photodiode, optical spectrometer and an optical CCD camera. Photodiode and optical spectrometer are used to collect the reflected laser and emitted spectrum from the sample respectively. The background signal is recorded by the spectrometer and subtracted from the emission spectrum.

The focal spot area is imaged by a CCD camera. At the time of damage; the generated damaged spot is recorded by the CCD camera connected to a personal computer. All the three diagnostics together are providing a better measurement of damage threshold of the glass sample. The irreversible modifications in the glass sample are observed by an optical microscope. The entire damage test is performed on 1-on-1 procedure (single shot). To see the thermal effects generated in the plasma formation process, we introduced a continuous flow of inert gas ( $\text{N}_2$  gas) on the laser focused surface during the experiment.

The damage modifications on the surface of the BK7 glass irradiated with different experimental conditions are examined by SEM (Mini SEM SNE–3000M) with a resolution of

100 nm. The pulsed Raman spectrums of undamaged and damaged regions are recorded by Raman spectrometer (Andor 550i with  $3 \text{ cm}^{-1}$  resolution) coupled with an ICCD camera at  $-30^\circ\text{C}$  temperatures. The excitation line used for Raman spectroscopy is 532 nm.

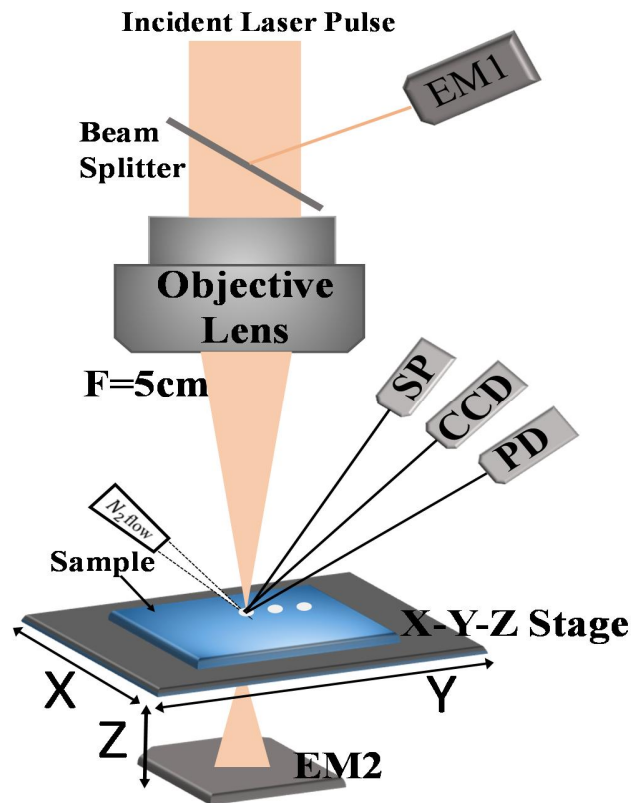


Figure 3. 1. Schematic of experimental setup; where EM1 and EM2- energy meters; PD- photodiode; CCD- charge coupled device; SP- optical spectrometer.

### 3.5. Results and Discussions

#### 3.5.1. Surface damage investigation

The damage threshold studies of BK7 glass are summarized in the table 3.1. Each data presented in table 3.1 is taken over an average of 10 shots on fresh target to reduce the errors. The effect of single and multiple shots on the same spot, the dependency of damages on the laser parameters are briefly discussed in the following sections.

### 3.5.2. Damage threshold and thermal effect studies of BK7 and its dependency on pulse duration

The dielectric materials at low intensities are transparent but become opaque at higher intensities because of the non-linear process, known as multiphoton ionization which generates over-dense plasma. The damage mechanism is generally considered as thermal absorption and electron avalanche, which play dominant role for the different laser pulse durations. In general, the damage mechanism may follow three steps (i) multiphoton absorption (ii) triggered conduction band mechanism and (iii) avalanche ionization. The typical damage morphology on the surface of components observed in experiments is also closely related to the damage mechanism. The damage crater in thermal absorption process, which can be estimated by thermal diffusion model, is typical distortion, melting and ablation debris often with an elevated rim caused by melted material flow and re-solidification. Damage initiated by electron avalanche is often accompanied by generation of plasma, crush and fracture. In general, most of the dielectric materials get damaged at lower intensity than the pure and defect free materials of same composition due to the presence of defects. This defect can be inherent inclusion of materials in which it is prepared or surface contamination or due to intense laser generated point defects. Because of such defect presence, the photon matter interaction occurs indirectly via defect state in the band gap (intra-band states). For example, in fused silica, a fundamental defect has been identified as neutral oxygen vacancy and a non-bridging oxygen hole centre. These defects have absorption about 5.8 and 4.8 eV respectively [56].

The primary mechanism of photon absorption is non thermal but the transfer of heat from electron to vibrations of the lattice is due to thermal conduction. The temperature evolution in the area of the interest (focal spot diameter on sample) depends on the optical absorption of the laser

radiation, the heat flux from the irradiated zone and on transformation enthalpies of phase transitions such as melt or evaporation. The evolution of thermal conduction (considering the heat transport by convection and radiation negligible) is given by [56]

$$\partial/\partial t (C_p \rho T) = \frac{1}{r^2} \partial/\partial r (r^2 k \partial T/\partial r) + Q(r, t) \quad (3.1)$$

where  $\rho$ ,  $C_p$  and  $k$  are mass density, specific heat capacity and thermal conductivity respectively.

The coefficients can be combined to the thermal diffusivity ( $D$ ) [56]

$$D = \frac{k}{C_p \rho} \quad (3.2)$$

According to Lambert Beer law the source term  $Q(r, t)$  can be written as

$$Q(r, t) = \alpha I(t) \exp(-\alpha r) \quad (3.3)$$

$\alpha$  = absorption coefficient =  $\frac{1}{d_\alpha}$ , where,  $d_\alpha$  is optical penetration depth

For BK7 glass, value of  $\alpha$  for optical light is  $27 \text{ cm}^{-1}$ , so the value of optical penetration depth is about  $370 \text{ }\mu\text{m}$ . From above equation (3.3) it is clear that the temporal dependence of laser intensity has significant effect on source term. For Gaussian pulse width with pulse duration  $\tau_p \geq \tau$  (heat relaxation time), the pulse width dependence of laser induced damage is approximated as

$$I(\tau_p) = I_{th} \exp[(\tau/\tau_p)]^2 \quad (3.4)$$

and the heat diffusion length is given by

$$d_\tau = \sqrt{4D\tau_p} \quad (3.5)$$

which is a measure of the heated material depth in the time of laser pulse duration. For BK7 glass value of  $D \sim 0.0052 \text{ cm}^2/\text{s}$ . Considering these values, we can conclude that it is optical confinement case ( $d_\alpha \gg d_\tau$ ) and the change in temperature at the optics surface is given by

$$\nabla T = \frac{I_0 \tau_p}{\rho C_p d_\alpha} \quad (3.6)$$

It can be seen from eq.(3.4) and table 3.1 that for shorter pulse duration the threshold intensity reduced. It has been reported that the damage threshold energy depends on laser pulse duration as  $\tau_p^\alpha$ , where  $\alpha$  varies from 0.3 to 0.6 [61], [68]. The value of the  $\alpha$  can be deduced by following relation,  $\frac{E_{th1}}{E_{th2}} = \left(\frac{t_1}{t_2}\right)^\alpha$ . Here  $E_{th1}$  and  $E_{th2}$  are the laser fluence at the damage threshold for the laser pulse duration of  $t_1$  and  $t_2$ . In present case the value of  $\alpha$  for the front surface is  $\sim 0.2$  and for the rear surface is  $\sim 0.3$ . This is measured by measuring the damage threshold energy for different pulse duration. The damage threshold for the front surface is lower than that of the rear surface. This is due to the fact that after the polishing process for the finishing of optical components there are residual obstacles, defects, imperfection and also the minute inclusions of polishing materials are imbedded in the surface where electric field of the light wave is greatly intensified which leads to the damage. From eq. 3.5 and 3.6, it is clear that for the longer pulse duration the thermal diffusion length is longer and temperature gradient is also higher which can cause larger damage area for the nanosecond laser than the picoseconds laser and same can be seen from the figure 3.2 (a) and (b).

### 3.5.3. Damage threshold dependency on wavelength

In multiphoton inter-band transitions, n-photons are absorbed simultaneously and their total energy exceeds the band gap. The generalized transition rate for n-photon process is given by [58]

$$\frac{dN_e}{dt} = \frac{\sigma^n N_0 I^n}{(\hbar\omega)^n} = \frac{\sigma^n N_0 (I\lambda)^n}{(hc)^n} \quad (3.7)$$

where  $\sigma^n$  is cross section for the n-photon process,  $N_0$  is ground state population density and  $I$  is local irradiance.

**Table 3. 1.** Threshold measurement for BK7 glass

laser	Pulse duration $t_p$	Wave-length $\lambda$	Front surface threshold (mJ) $E_{th}$	Rear surface Threshold (mJ) $E_{th}$	Damage mechanism	Damage phenomenon
ns	8 ns	1064 nm	0.74	1.48	Impact ionization	Micro pits, debris
ns	8 ns	532 nm	0.36	0.59	Impact ionization	Micro pits, debris
ps	500 ps	1064 nm	0.45	0.625	Impact ionization	Crater, plasma melting and crush
ps	500 ps	532 nm	0.234	0.34	Impact ionization	Crater, plasma melting and crush

The probability of multiphoton ionization is increased for small value of n i.e. for shorter wavelengths; less number of photons is required to overcome the inter-band transitions. From eq. (3.7), we can estimate the required breakdown intensity and can be written as

$$I_c = \sqrt[n]{(N_e/N_0\sigma^n\Delta t)} \left( hc/\lambda \right) \quad (3.8)$$

From eq. (3.8), it is clear that the damage threshold is lower for shorter wavelength. This can also be seen from the table 3.1 that the laser induced breakdown threshold energy is lower for 532 nm than 1064 nm.

### 3.5.4. Effect of convection on glass damage using N<sub>2</sub> gas flow

The ambient medium can be heated directly by absorption of laser in medium or indirectly by substitute heated area. Heat transport within a gas takes place by conduction, convection and thermal radiation. Convection can be originated from the density gradient which is related to temperature gradients and is known as free convection. In case of external flow of gas with medium or higher pressure convection is known as forced convection. In this case, flow of N<sub>2</sub> gas along the laser heated substrate has been used. Here we will discuss about two cases, case (i): steady state condition i.e. the damage mechanism studied in the air medium but no gas flow (first case shown in figure 3.2 (a)); the temperature rise for the Gaussian beam can be written as [56]

$$Q_c = \Delta T_c = \frac{P(1-R)}{2\sqrt{\pi}\omega_0 k_s} \left(1 + \frac{k}{k_s}\right)^{-1} \quad (3.9)$$

where  $k_s$  and  $k$  are the thermal conductivity of the substrate and medium.  $R$  is the reflectivity and  $P$  is the laser power and  $\omega_0$  is the beam focal spot diameter. With the stationary condition i.e. in the absence of convection, the heat flux from the surface is shared between the ambient medium and the substrate. In this case, the temperature rise changes only a little in the presence of the gaseous atmosphere.

Case (ii): The convection is important if the irradiated surface is exposed to medium or high pressure flow of gas (with medium pressure N<sub>2</sub> gas flow). The influence of the forced convection on the substrate can be estimated if we take into account the surface conduction  $\eta$  for  $v_0 \ll v_c$ , where  $v_0$  is sound velocity and  $v_c$  is the gas flow or velocity of the convection flow as

$$\eta = \eta(T) + \eta_1(T) \left(\frac{v_c}{v_1}\right) \quad (3.10)$$

where for standard condition  $v_1 \approx 1m/s$  for air and  $\eta_1 \approx 0.2\eta$ . All coefficients  $\eta_i$  depend on the geometry and its orientation with respect to gas flux. Then the temperature in the ambient medium can be described as

$$\rho C_p \frac{\partial T}{\partial t} - \nabla[k(T)\nabla T] + \rho C_p v_c \nabla T = 0 \quad (3.11)$$

Here third term is due to convection. By comparing the single term in the eq. (3.11), the influence of heat transfer caused by convection and conduction can be estimated as

$$v_c^* = \frac{\rho C_p v_c T l^{-1}}{l^{-1} k T l^{-1}} = \frac{v_c l}{D} \quad (3.12)$$

where  $\nabla T \approx \frac{T}{l}$  is used and  $l$  is the characteristic length which has the dimension of the hot zone.

From equation 3.9–3.12, it is clear that for the higher flow of pressurized inert gas the thermal conduction and convection also becomes important and the temperature of the substrate reduces significantly. To study the local thermal effect initiated by high local temperature and pressure on the damage threshold and morphology, we removed these thermal effects by continuous flow of pressurized inert N<sub>2</sub> gas on the surface of the sample. The images shown in the figure 3.2 (c) and 3.2 (f) are clearly indicating that the heat removal using pressurized N<sub>2</sub> gas on the damage site drastically decreases the spot diameter. The images shown in figure 3.2 (c) and (f) are the damages created by 8 ns and 500 ps pulse durations respectively in the presence of pressurized gas flow. The flow rate of the N<sub>2</sub> from the nozzle is kept between 6 to 7 liters per minute (lpm). From the images, it is clear that the local heat generated in the ablation process during the central crater formation is taken away by the inert gas. Also, the effect of thermal tensile stress is very much reduced. This resulted in reduction of fracture and cracking and this effect can be seen from the figure 3.2 (a) (without gas flow) and figure 3.2 (c) (with pressurized N<sub>2</sub> gas flow).

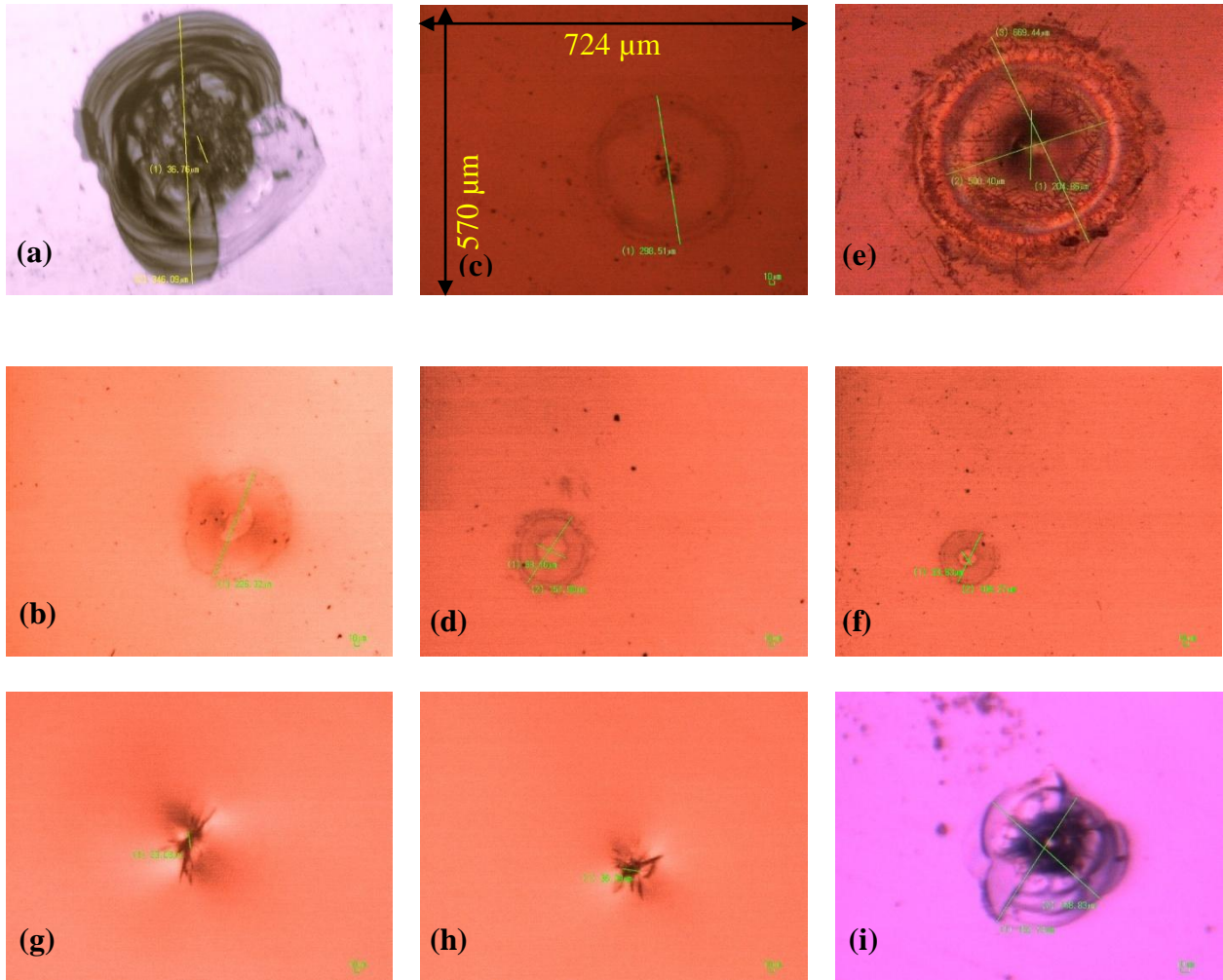


Figure 3. 2. Optical microscope images of the front surface of the sample at 4 mJ energy where; (a)  $\lambda= 1064\text{nm}$ ,  $t_p= 8 \text{ ns}$  without  $\text{N}_2$  flow (b)  $\lambda= 1064\text{nm}$ ,  $t_p= 500 \text{ ps}$  without  $\text{N}_2$  flow (c)  $\lambda= 1064 \text{ nm}$ ,  $t_p= 8 \text{ ns}$  with  $\text{N}_2$  flow (d)  $\lambda= 532\text{nm}$ ,  $t_p= 500 \text{ ps}$  without  $\text{N}_2$  flow (e)  $\lambda= 1064\text{nm}$ ,  $t_p= 8 \text{ ns}$  with  $\text{N}_2$  flow, 50 shots (f)  $\lambda= 532\text{nm}$ ,  $t_p= 500 \text{ ps}$  with  $\text{N}_2$  flow (g) optical microscope images of rear surface damage at  $\lambda= 532 \text{ nm}$ ,  $t_p= 500 \text{ ps}$  (h) optical microscope images of rear surface damage at  $\lambda= 532\text{nm}$ ,  $t_p= 8 \text{ ns}$  (i)  $\lambda= 1064 \text{ nm}$ ,  $t_p= 500\text{ps}$  without  $\text{N}_2$ , at higher laser energy focused at rear side. In figure 3.2 (a), the magnification is 9x and for figure 3.2 (b-i) magnification is 6x.

### 3.5.5. Effect of incident Laser energy and number of pulses on damaged area

The instant of the damage on the glass is measured by using the photodiode (PD) which collects the scattered light. The scattered light profiles for different laser energies are shown in figure 3.3. In the beginning when there is no damage, no signal is detected by the PD. At the moment damage occurs (at  $E_{th}$ ) the photodiode detects the scattered light with small peak. The photodiode signal amplitude and the temporal behavior increases with laser energy. At  $E = E_{th}$  a small point damage occurs at the peak of laser spatial profile so scattering is small. For the case  $E > E_{th}$  larger spatial portion of the beam crosses the  $E_{th}$  and hence larger damage site. This resulted larger scattered area and hence larger signal detected by PD.

Figure 3.4 (a-c) shows measured induced damage width with respect to incident laser energy at 8 ns and 500 ps, keeping wavelength fixed; scaling of spot diameter with laser energy for 532 and 1064 nm at fixed laser pulse duration; and effect of inert gas flow on the surface during damage at fixed laser wavelength and pulse duration respectively. From the graph it can be seen that the damage width increases nonlinearly and get saturated against the incident laser energy. The diameter of this circular deformation is decided by the intensity of the incident laser. A simple quantitative relation between ablation diameter (D), material dependent damage threshold fluence ( $\phi_{th}$ ), and peak fluence in the beam ( $\phi_0$ ), is given by:

$$D^2 = 2\omega_0^2 \ln\left(\frac{\phi_0}{\phi_{th}}\right) \quad (3.13)$$

Where  $\phi_0 = \frac{2I_p \times Area \times t_p}{\pi \omega_0^2}$ , and  $\omega_0^2 = \frac{1}{e^2}$ ,  $I_p$  are Gaussian beam radius and laser pulse intensity respectively.

Figure 3.4 (d) shows the damage diameters dependence on the number of pulses at the same site. In these experiments, laser energy is fixed at 3.24 mJ, 21.8 mJ and 28.3 mJ and change the number of shots to 10, 25 and 50. From figure 3.4 (d), it is clear that the damage diameter

increases with increasing the number of pulses at the same position and same can also be seen from figure 3.2 (e) for the laser energy of 3.24 mJ and 50 numbers of shots at same positions. It is also observed that the lateral diameter increase slowed down and become constant after large number of laser shots, but the depth of damage increases with the number of laser shots. This phenomenon can be explained by the plasma formation mechanisms after dielectric breakdown. In case of high power short pulse laser irradiation, the laser energy absorbed by the plasma in the material is released mainly in three forms such as part of the energy drives crash material movement, some part used in shock formation and transportation, and remaining is consumed in cracking. When the laser fluence is further increased, the damage diameter and damage depth increased as function of number of shots in the stage 1 and then in the second stage the damage diameter became constant and depth increased.

The damage morphology between front and back surface is different as can be seen from figure 3.2 (g) and (h). On the front surface, the surrounding area of the damage site where laser is being absorbed is burned by the plasma. The plasma is shielding the surface, just in contrast to the rear surface, where the plasma is ignited in the bulk near the rear surface. Plasma ignition is a source of generation of an acoustic wave/shock wave. This strong pressure tends to damage the optics in a more catastrophic way than on the entrance surface. H. E. Bennett et al., [69] has shown by numerical models that the shock pressure at exit surface is 6 times greater than the entrance faces at the same laser energy. In case of rear surface much deeper crack propagation appears in comparison to front surface as shown in figure 3.2 (g) and (h). The induced damage generates a streak much inside the bulk of the sample instead of circular morphology because of the Rayleigh range of the focusing optics and confined plasma. Damage growth at rear surface of components is extremely severe. This can be explained by several models such as fireball

growth, impact crater, brittle fracture and electric field enhancement [70]–[74]: all the physical effects are not independent but mutually coupling. Plasma at rear surface ejects into the material with high kinetic energy which is redistributed between plasma and material along their interface. Once the pressure exceeds the materials strength, the plasma parameters at the interface causes deformation, material crash and crater deformation as shown in figure 3.2 (i).

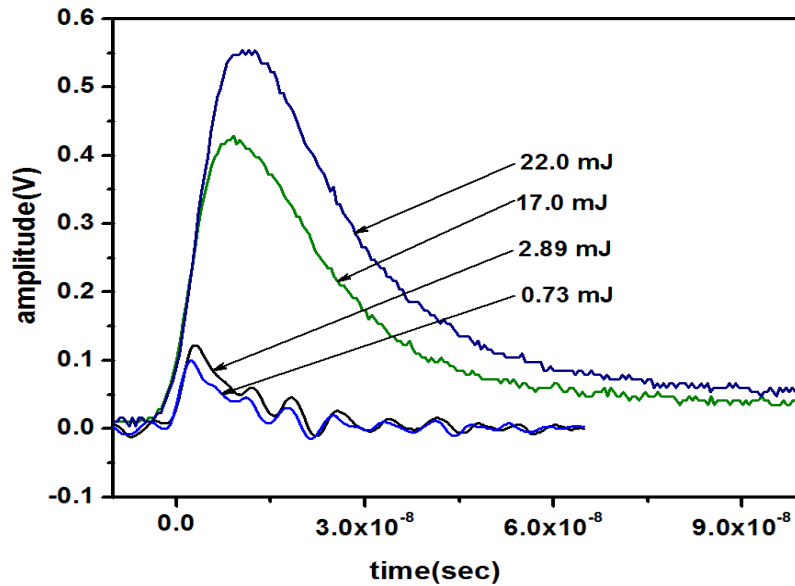
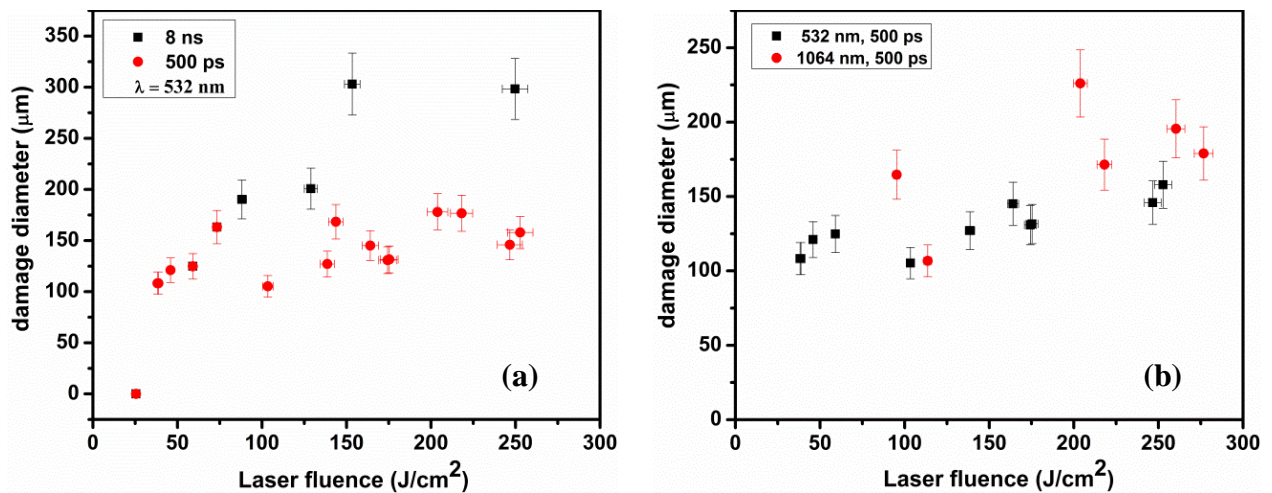


Figure 3. 3. Photodiode signal of scattered light from damage spot at various laser energies.



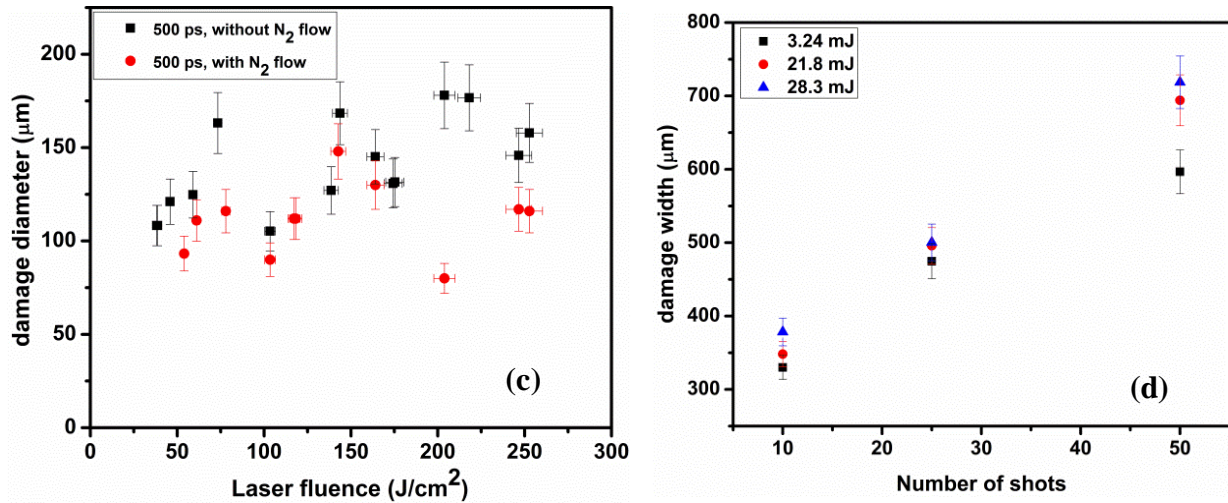
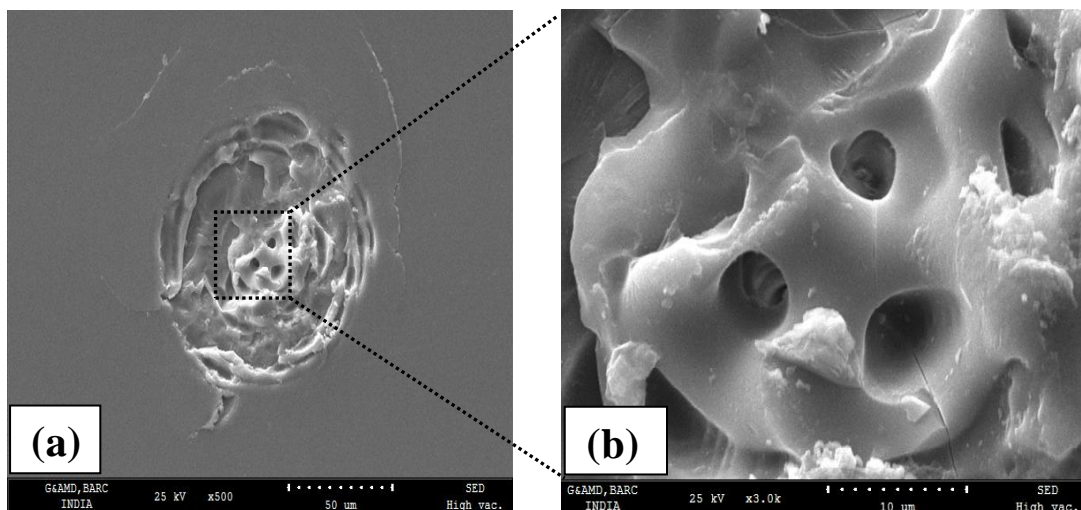


Figure 3. 4. Dependency of damage width on (a) laser pulse duration and at fixed wavelength i.e. 532 nm (b) laser wavelength for fixed pulse duration (c) effect of inert gas flow on damage width and (d) the number of shots at the same position for a fixed laser parameters.

### 3.5.6. Damaged Surface Morphology

The effect of laser irradiation on target surface induced by laser pulses at intensities above the damage threshold in BK7 glass are studied by using scanning electron microscope (SEM). Figure 3.5 (a-b) and 3.5 (c-d) shows the SEM images of irradiated glass surface by picoseconds (500 ps, 532 nm, single shot) and nanosecond (8ns, 532 nm, single shot) laser pulses respectively at a fixed laser energy of 4 mJ. When the incident laser energy density exceeds the critical value i.e.  $E_{pulse} \geq E_{th}$  for the longer pulse duration, the local temperature increases sharply and reaches the boiling point of the material. Because of this, generated tensile stress exceeds the dynamic strength of the material which causes the cracks and fracture. The continuous merging of these micro cracks leads to ejection of one or several fragments from the sample. The ejected molten material from the interaction zone splashes out on the surface of glass around the irradiation region. These traces of spalled material and ejected fragments can easily be seen in the figures 3.5 (c-d). From the figure 3.5 (c), the heat and mechanical stress

affected zone around the central crater can be seen. These cracks and heat affected zones are generated mainly due to the distribution of thermal heat and stress on the laser focused area at the time of plasma formation. With long pulses there is enough time for the thermal waves to propagate into the target and create relatively a large layer of melted material. On the other hand, in short pulse regime, the lattice temperature remains much less than the electron temperature, thus laser ablation in this case is accompanied by the electron heat conduction and can be seen from figure 3.5 (a) and (b). By comparing figures 3.5 (a) and (c) we can see that, in case of nanosecond pulses sputtering and shock wave induced damage has taken place instead of melting process. While with the picosecond pulses, melting processes are dominating and at intensities  $I_p \geq 3 \times 10^{10} W/cm^2$ , a melt area looks like water waves, on the glass surface. Figure 3.5 ( a and c) also shows the edge of damage surface, which suggest short pulses are more efficient in creation of precise and small hole with a lower energy, compared to long pulses. Brand and Tam also reported that spherical molten droplets are ejected when an optical component surface is irradiated by picosecond lasers from the interaction zone [64], [65], [75]. While the irradiated surface region from glass generally is removed without melting process when exposed to nanosecond laser pulse of lower intensity.



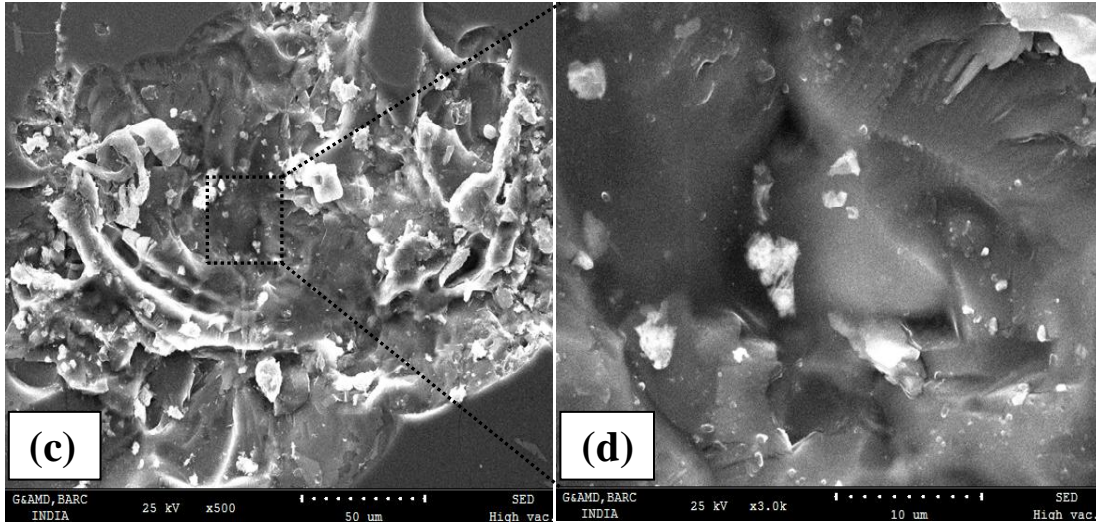


Figure 3. 5. (a & b) show SEM images of irradiated glass target with 500x and 3Kx magnification for the laser pulse  $t_p= 500$  ps and energy 4 mJ and (c & d) for the laser  $t_p= 8$  ns and energy 4 mJ.

### 3.5.7. Laser transmission through BK7 glass

In this experiment, glass sample are irradiated by two different pulses (500 ps and 8 ns) and wavelengths (1064 nm and 532 nm). The transmitted laser pulse from the glass is collected by an energy meter. The percentage of transmitted laser energy as a function of incident laser radiation is shown in figure 3.6 (a-d). As the laser intensity increases the percentage transmission through the glass decreases, showing more damage or absorption of laser light into the plasma. Also, it can be seen that the laser transmission through back surface is more in comparison to the front surface. The front surface is more contaminated than the bulk, initiation of ionization occurs at lower energy. From the graphs, it is clear that the laser energy absorption phenomenon happening here is completely nonlinear in nature. The reduction in transmission with increase of laser energy can be explained by the laser temporal profile. For the nanosecond laser with energy near the damage threshold, the energy of the leading part of the laser pulse is below threshold energy and hence it will be transmitted through the sample and remaining part of the laser pulse

profile interact with the weak plasma generated at the damage spot partly getting absorbed and scattered in all the direction. However, with increase in the laser energy, the threshold energy can be achieved much before the peak in the leading portion of the laser pulse and hence, larger part of laser pulse interact with the stronger plasma generated at the damage spot. Here damage spot diameter will also increase, so larger portion of laser light will see absorption and scattering.

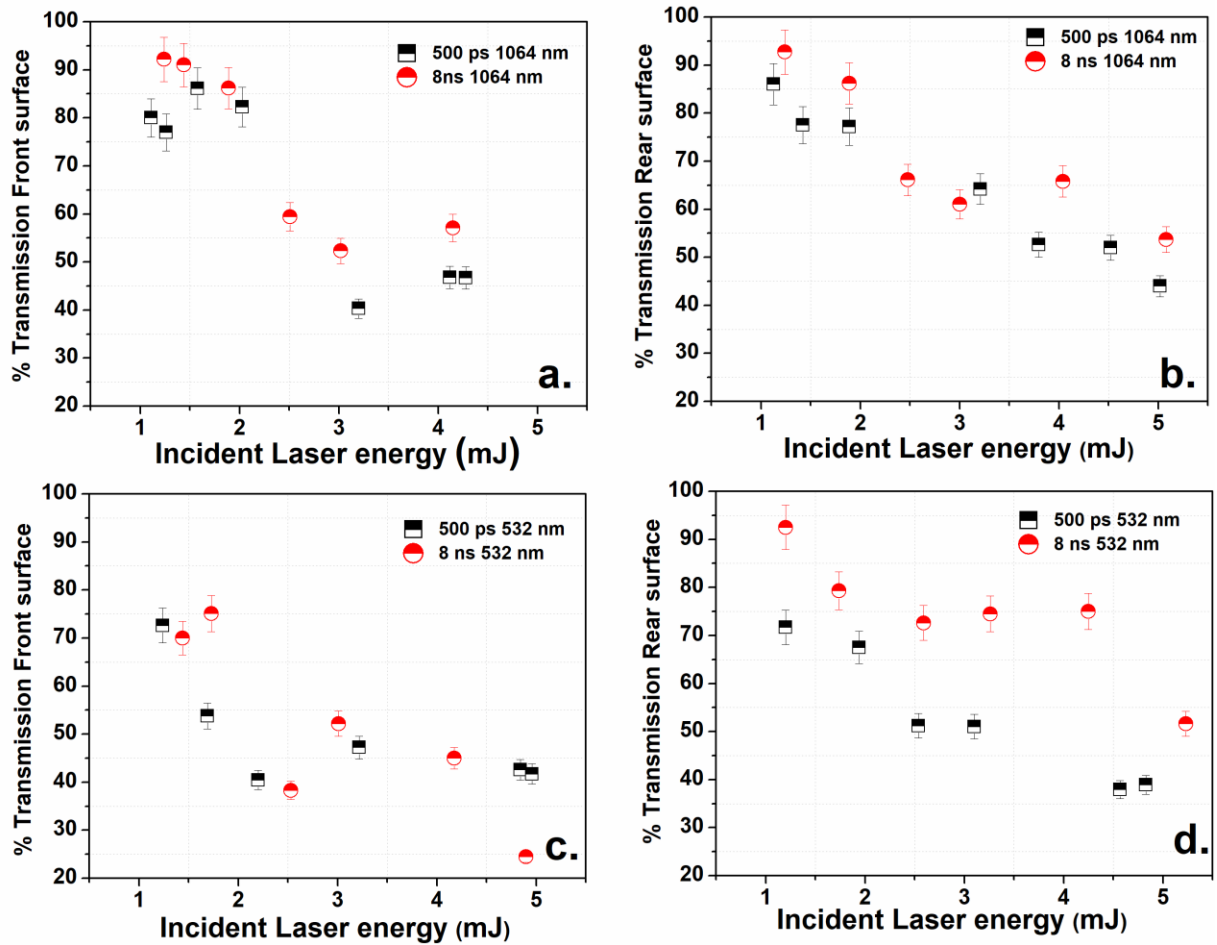


Figure 3. 6. Percentage transmitted energy as a function of incident laser energy where; (a) front surface % glass transmission at  $\lambda= 1064$  nm,  $t_p= 500$  ps and 8 ns (b) rear surface % glass transmission at  $\lambda= 1064$  nm,  $t_p= 500$  ps and 8 ns; (c) front surface % glass transmission at  $\lambda= 532$  nm,  $t_p= 500$  ps and 8 ns; (d) rear surface % glass transmission at  $\lambda= 532$  nm,  $t_p= 500$  ps and 8 ns.

In case of short laser pulse, the leading part is steeper and hence achieve threshold in faster scale with increase in the laser energy compared to longer pulse as it can be seen from the graphs in figure 3.6 (a-d). The transmission for the 532 nm laser beam reduces even about 1 mJ, which is due to the fact that the damage threshold is lower for lower wavelength lasers. The drastic decrease in the transmission of the laser beam through the damage spot is due to the absorption of laser light in the plasma formed due to the laser induced breakdown in glass. Once the plasma frequency is more than the critical density for the laser wavelength, plasma behaves like an opaque medium for the laser beam and hence transmission is drastically reduced.

### **3.5.8. Study of micro structural modifications in Borosilicate glass by laser irradiation using offline Raman spectroscopy**

The Raman spectra of BK7 glass are studied to detect microstructural changes after laser irradiation. Results are shown in figure 3.7. Raman spectroscopy generally provides information about the changes in covalent network of the sample. For the undamaged portion of the sample, peaks are observed at  $450\text{ cm}^{-1}$ ,  $518\text{ cm}^{-1}$ ,  $635\text{ cm}^{-1}$ ,  $810\text{ cm}^{-1}$  and  $1100\text{ cm}^{-1}$ . The peaks at  $450\text{ cm}^{-1}$  and  $518\text{ cm}^{-1}$  are assigned as bending modes of Si-O-Si linkages [76], [77]. Peak around  $518\text{ cm}^{-1}$  is related to the average inter-tetrahedral Si-O-Si angle [50], [76], [78]. The peak at  $635\text{ cm}^{-1}$  arises due to danburite ( $\text{B}_2\text{Si}_2\text{O}_8^{2-}$ ), metastructural units and assigned to a single asymmetric mode [76]. The peaks at  $810$  and  $1100\text{ cm}^{-1}$  are assigned to  $\text{SiO}_4$  band and arises due to Si-O-Si linkages with two non-bridging oxygen atoms [50], [78]. Sharp peaks at  $635$  and  $1100\text{ cm}^{-1}$  indicates the intense vibration of  $\text{B}_2\text{Si}_2\text{O}_8^{2-}$  and Si-O-Si groups.

The spectrum from damaged portion is very similar to undamaged portion. The vibrational band at  $810\text{ cm}^{-1}$  shows a decrease in intensity, but do not vanish completely by the laser irradiation which is because of their strong bond energy. For nanosecond laser damaged

region the relative intensity of Raman peaks decreases significantly. This indicates a serious depolarization of vibrational bands caused by the irradiation. Compared to nanosecond laser irradiation the picoseconds laser irradiation damaged spectra have higher relative intensity, indicating that the vibration groups are more easily destroyed by nanosecond laser pulses. The unmodified spectra in damage sample suggest that the processes involved here in laser induced damages are an ionic transformation rather than a covalent conversion.

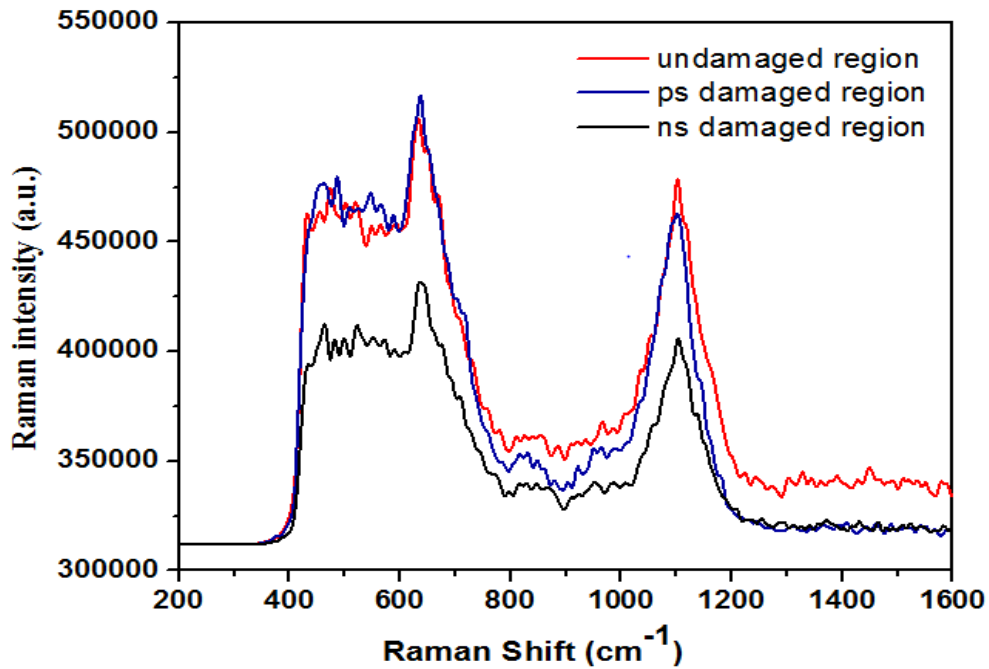


Figure 3. 7. Raman spectrum from damaged and undamaged region of BK7 glass at  $t_p= 500$  ps and 8 ns.

### 3.5.9. Optical Spectroscopy for plasma temperature and density calculation

The plasma formed during high power laser irradiation contains atoms and ions in different excited states, free electrons and radiation. The analysis of this plasma can be done through the measurement of plasma temperature ( $T_e$ ) and free electron density ( $n_e$ ). The plasma temperature describes the plasma state and the free electron density determines the

thermodynamic equilibrium state of the plasma [79], [80]. The emitted spectrum is shown in figure 3.8.

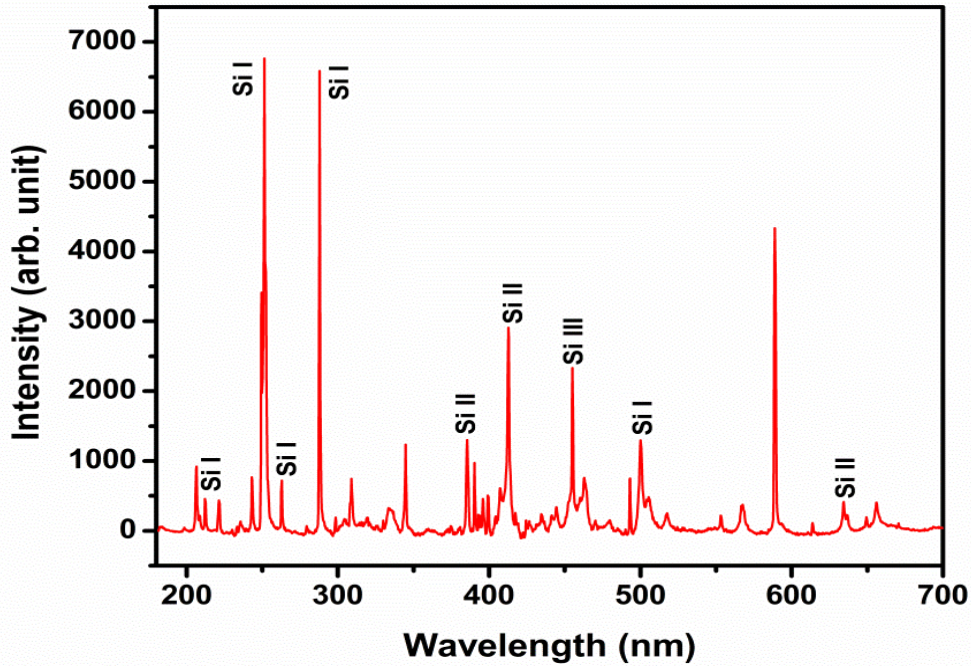


Figure 3. 8. Recorded emission spectra of BK7 glass plasma irradiated by an Nd: YAG laser of pulse duration 8 ns and wavelength 1064 nm.

### 3.5.10. Plasma Temperature Measurement

For the calculation of the plasma temperature, the Boltzmann plot is widely used with considering the plasma in local thermodynamical equilibrium (LTE) [79], [81]–[83]. Using this equation for LTE and relative intensity of two or more lines emerging from the same kind of species and the same ionization stage, temperature can be estimated. However, the temperature can also be measured considering the plasma in local thermodynamical equilibrium (LTE) using Saha-Boltzmann equation [84] in this case population of the ground state of the two consecutive ion states are to be known, and the information of the plasma density must be known in advance. Other diagnostics that typically assume LTE include the use of the line-to-continuum intensity

ratio or Planck's law for  $T_e$ , which can then be used to recover  $N_e$  via absolute spectral radiance measurements [85], [86]. It is observed that the measurements done using above these three methods are not very far from each other [87]. Griem considered that when a plasma is relatively dense and of low temperature ( $N_e > 10^{16} \text{ cm}^{-3}$  and  $T_e < 5 \text{ eV}$ ), it is in thermal equilibrium and the Boltzmann distribution can be used. To avoid the corrections against the relative responses of the detector the wavelength separation of the line used must be very small and in order to get precise result the upper excited state energy separation should be large and the lines should be optically thin i.e. absorption by plasma is negligible. For plasma in local thermodynamic equilibrium (LTE), the population density of atomic and ionic electronic states is described by Boltzmann distribution. The condition required for this assumption is that the radiative depopulation rates are negligible in comparison to collisional depopulation rate.

For LTE plasma the temperature can be calculated from the slope of the lines defined by the below expression;

$$\ln \left( \frac{I_{ki} \lambda_{ki}}{g_k A_{ki}} \right) = C - E_k / k_B T \quad (3.14)$$

where  $I$ ,  $\lambda$ ,  $A$ ,  $E_k$ ,  $g_k = 2J_k + 1$  are the spectral intensity, wavelength, transition probability, upper level energy and statistical weight of the upper state respectively,  $C = \ln [hcN_k/4\pi Q(T)]$  [where  $Q(T)$  is the partition function] and  $T$  is the temperature.

The values of these parameters are taken from NIST data base [88] and summarized in table 3.2. The plasma temperature estimated in this case is approximately 0.94 eV and the corresponding Boltzmann plot is shown in figure 3.9. The lines taken for the temperature calculations are summarized in table 3.2.

**Table 3. 2** Atomic parameters for the Si I, Si II and Si III used in temperature estimation

Element	Wavelength $\lambda_{ki}$ (nm)	Transition probability $A_{ki}$ ( $s^{-1}$ )	Statistical weight $g_k$	Upper energy level $E_K$ ( $cm^{-1}$ )	Reference
Si II	385.53	$0.44 \times 10^8$	4	81251	[88]
Si II	413.10	$1.74 \times 10^8$	3	40992	[88]
S I	493.09	$0.042 \times 10^8$	6	103556	[88]
S I	500.09	$0.028 \times 10^8$	5	60962	[88]
Si II	504.33	$0.70 \times 10^8$	4	101023	[88]
Si II	505.44	$1.45 \times 10^8$	6	101024	[88]
S II	634.30	$0.584 \times 10^8$	4	81251	[88]
Si II	636.80	$0.680 \times 10^8$	2	81198	[88]
Si I	656.20	$0.0069 \times 10^8$	7	63514	[88]

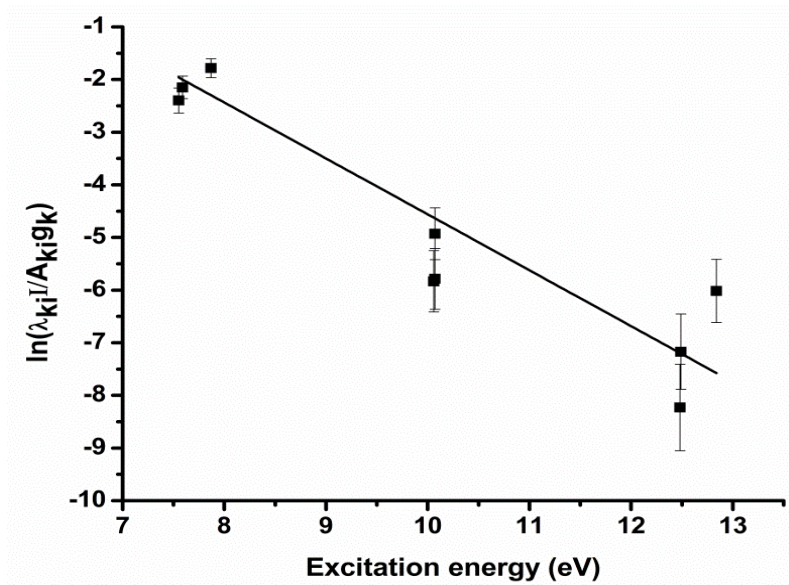


Figure 3. 9. Saha Boltzmann plot using Silicon excitation lines for plasma temperature estimation.

### 3.5.11. Free electron density Measurement

The most important quantity related to plasma density is the free electron density. If the relative abundance of species is known, ion densities can be calculated by using macroscopic neutrality condition from the measured free electron density. The electron number density emitted from plasma can be measured from the following methods; by the measurement of optical reflectivity, by calculating the principal quantum number of the series limit, measurement of Stark profiles of optically thin emission spectral lines, measurement of absolute line densities and from the measurement of absolute emissivity of the continuum emission [79], [80]. It is important to note that the Stark broadening is relatively independent of the temperature. Therefore, the electron number density can be calculated with good accuracy even when the temperature is not well known. So, the determination of electron number density by this method is independent from any assumption of LTE conditions. The Spectral lines width are always broaden and is a composition of finite resolution of the spectrometer used and intrinsic physical causes; the principal causes are Doppler and Stark broadening. If line widths are small against radiative transition and perturbing level separations, Stark broadening is usually dominated by electron collisions. Since the Stark broadening of the spectral line depends on the electron number density, so electron density  $n_e$  could be determined from the corrected FWHM [ $\Delta\lambda = \Delta\lambda_{observed} - \Delta\lambda_{instrument} - \Delta\lambda_{Doppler}$ ] of the line. For a non H-like line the electron density can be calculated from the following relation [80], [89].

$$n_e(cm^{-3}) = \left( \frac{\Delta\lambda}{2\omega(\lambda, T_e)} N_r \right) \quad (3.15)$$

where,  $\Delta\lambda$  is the FWHM of the corrected spectral line width,  $\omega(\lambda, T_e)$  is the Stark broadening parameter can be found in the standard table [79],  $N_r$  is the reference electron density is  $10^{16}$  for neutral atoms and  $10^{17}$  for singly ionized atoms [90], [91]. In the above expression the

ion impact broadening effect is neglected and assumed that lines used to evaluate electron number density should be optically thin. The calculated electron number density from the Lorentzian FWHM and atomic constant used to evaluate the electron densities are tabulated in Table 3.3. The calculated density for lines Si I, Si II and Si III are found to be in the range  $3.16 \times 10^{17} \text{ cm}^{-3}$ .

**Table 3.3.** Spectral Parameters for Si I, Si II and Si III calculated free electron density

Element	Wavelength $\lambda_{ki}$ (nm)	Lorentzian FWHM $\Delta\lambda$ (nm)	Stark Broadening Parameter $\omega$ (nm)/ $N_r$	Reference Source	Calculated Electron Number Density $n_e(\text{cm}^{-3})$
Si I	287.91	0.74	$0.064/1 \times 10^{16}$	[92]	$5.78 \times 10^{16}$
Si I	390.5	0.696	$0.12/1 \times 10^{16}$	[92]	$2.90 \times 10^{16}$
Si I	243.09	0.71	$0.125/1 \times 10^{16}$	[92]	$2.84 \times 10^{16}$
Si I	298.46	0.89	$0.0147/1 \times 10^{16}$	[92]	$3.03 \times 10^{17}$
Si II	634.71	1.93	$0.129/1 \times 10^{17}$	[90]	$7.50 \times 10^{17}$
Si III	455.262	0.769	$0.53/1 \times 10^{17}$	[90]	$7.25 \times 10^{17}$

### 3.5.12. Reason for considering plasma in LTE

For any given plasma to be considered to be in LTE the lower limit for the electron number density  $n_e$  must satisfy equation given below [93]

$$n_e (\text{cm}^{-3}) \geq 1.6 \times 10^{12} T^{1/2} \Delta E^3 \quad (3.16)$$

where  $\Delta E$  (eV) is the energy difference between the upper and lower states and  $T$  (K) is the plasma temperature. For the Si (I) 288.16 nm line transition,  $\Delta E = 4.3$  eV. Considering the highest plasma temperature measured here,  $T_e \geq 10904$  K. So, the required electron density,  $n_e$

for the plasma to be in LTE, the density should be  $\geq 1.3 \times 10^{16} \text{ cm}^{-3}$ . In these measurement the average density taken over several lines is  $3.16 \times 10^{17} \text{ cm}^{-3}$ . Hence the selection of LTE model in our experiments is appropriate.

### 3.6. Summary and Conclusions

In this study, a detailed analysis of laser induced damage mechanism in BK7 glass used for making confinement geometry targets has been performed for two laser pulse durations 0.5 and 8 ns, for two laser wavelength i.e. 1064 and 532 nm. It is observed that the rear side of the optical glass being used for the confinement of plasma can sustain the threshold fluence of about  $75 \text{ J/cm}^2$  and  $31 \text{ J/cm}^2$  at the fundamental wavelength for nanosecond and sub-nanosecond laser pulses respectively. At these laser fluences, laser will interact directly to the Aluminium foil without damaging the optical glass in confinement geometry scheme. This Aluminium foil is being used as a shock wave generator. It is found that the samples display higher damage threshold energy when irradiated with long pulse in comparison to short laser pulse. Furthermore, because of reduced interaction time of pulse with the samples, the thermal losses are less in the picoseconds regime as compared to nanosecond pulse. The estimated average temperature and density for nanosecond produced plasma from the optical emission spectrum is around 0.94 eV and  $3.16 \times 10^{17} \text{ cm}^{-3}$ . The SEM record of the damage spot due to nanosecond and sub-nanosecond laser pulses shows that in case of long pulse, the tensile stress exceeds the dynamic strength of the material which causes the cracks and fracture. However, for short pulse laser, laser ablation is accompanied by the electron heat conduction and melting processes are dominated. These above result suggest that the long pulse lasers are much suitable for shock generation using confinement geometry target assembly, while short pulse lasers are more suitable for material processing. Lastly, the laser modified and unmodified regions are studied

with the help of Raman spectroscopy. The Raman results show that vibrational groups are more easily damaged by nanosecond laser pulses. The recorded Raman spectrum has similar nature for both the pulses and suggests that the processes involved in the permanent transformation are ionic rather than bond or covalent conversion. These parameters obtained from this experiment are used to design confinement geometry target for laser shock experiments [47], [48].



## Chapter 4. Raman Spectroscopic analysis of Aromatic plastic scintillating polymers under Laser driven Shock Compression

### 4.1. Introduction

This chapter describes the Raman spectroscopic analysis of Polystyrene and PVT that reveals the behavior of these aromatic polymers under shock compression. Polystyrene ( $C_8H_8$ )<sub>n</sub>, consists of simple structural units, and has been a subject of several spectroscopic studies [94]–[96]. There are three types of conformational isomers in polystyrene: atactic (aPS), isotactic (iPS) and syndiotactic (sPS). The aPS form is usually found to be amorphous with low crystallinity, whereas the iPS and sPS are mostly crystalline. In the crystalline iPS the macromolecule's substituent are located on the same side of the macromolecular backbone and consists of a 3<sub>1</sub> helical chain [94]. Whereas in the crystalline sPS the macromolecules substituent have alternate position along the chain and is known to take four polymorphic structures [95]–[97]. In the case of aPS, the substituent groups are randomly located on both side of the main polymeric chain, making it amorphous. Sears et al. [95], [98] assigned the Raman bands of aPS using the spectral changes with a degree of polymerization. While poly vinyl toluene (PVT) is a synthetic polymer of alkyl benzenes with a linear formula  $[CH_2CH(C_6H_4CH_3)]_n$ . Commercial vinyl toluene is a mixture of methyl styrene isomers.

The plastic scintillator radiation detectors based on polystyrene and poly vinyl toluene (PVT) are well known and are being commercially produced by Saint Gobain, USA for various radiation monitoring applications. The light emitting efficiency of the PVT based plastic scintillator is reported to be better than that of the polystyrene based ones. Further the higher glass transition temperature (T<sub>g</sub>) value of PVT than that of polystyrene is also responsible for better stability of the plastic scintillators based on PVT. In context of advancement of

scintillating detectors, studies of the response of radiation scintillators under extreme conditions are important. In the present chapter, the effect of the shock compression on the molecular structure and conformation of polystyrene and PVT, and their stability under extreme conditions are examined. The work described in this chapter has been published in Journal of Raman spectroscopy [47], [99], [100].

## **4.2. Synthesis and characterization of Polystyrene and PVT**

### **4.2.1. Polystyrene**

Polystyrene obtained by thermal polymerization of styrene monomer is used for preparation of the films. The polystyrene films are formed by melt casting method using appropriate spacer for the required thickness. The thermogravimetric analysis (TGA) and differential scanning calorimetry (DSC) profiles of the polystyrene, recorded at a heating rate of 20°C per minute, under N<sub>2</sub> atmosphere, are shown in figure 4.1. It is evident from the figure 4.1 that the polystyrene sample starts decomposing near 400°C. The glass transition temperature (T<sub>g</sub>) value is determined from the DSC profile recorded at 3°C per minute, under N<sub>2</sub> atmosphere, and is found to be ~95°C.

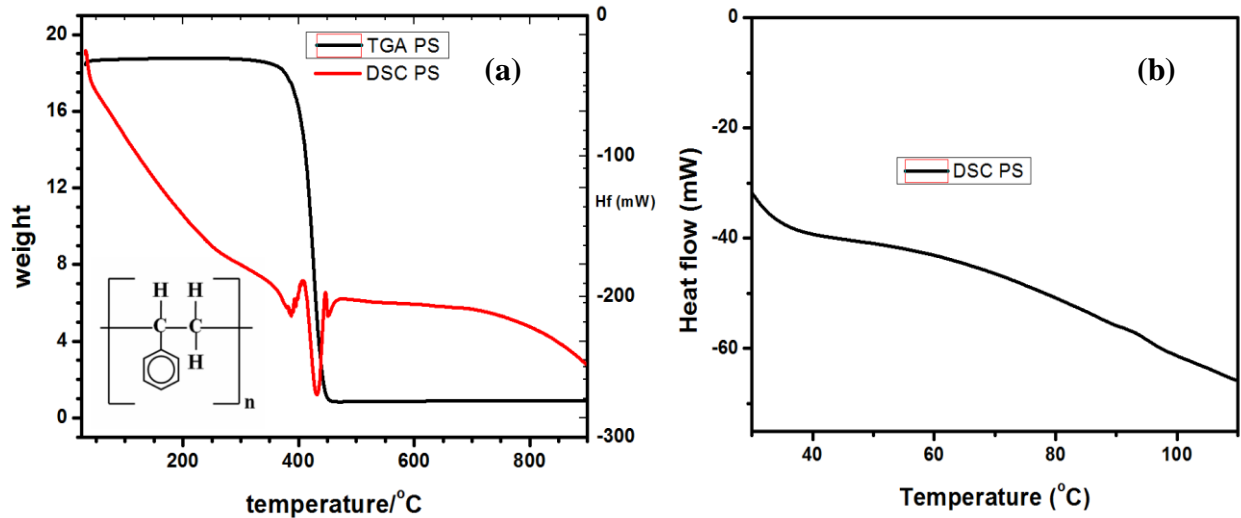


Figure 4. 1. The (a) thermogravimetric analysis (TGA) (where inset shows the chemical structure of polystyrene) and (b) differential scanning calorimetry (DSC) profiles of the polystyrene, recorded at a heating rate of 20°C per minute, under N<sub>2</sub> atmosphere and DSC profile recorded at 3°C per minute to measure glass transition temperature.

#### 4.2.2. Poly vinyl toluene

The poly vinyl toluene (PVT) is obtained by thermal polymerization of vinyl toluene monomer using benzoyl peroxide as initiator. The polymer is precipitated with methanol and purified by repeated dissolution and precipitation. The PVT films of size 100×100 mm<sup>2</sup> are formed by melt casting method using appropriate spacer for the required thickness (200 μm). The thermogravimetric analysis (TGA) and differential scanning calorimetry (DSC) profiles of the PVT, recorded at a heating rate of 15°C per minute, under N<sub>2</sub> atmosphere, showed decomposing of the polymer near 400°C. The glass transition temperature (T<sub>g</sub>) value could not be determined from the DSC profile recorded even at much slower heating rate of 3°C per minute. The T<sub>g</sub> value of the poly vinyl toluene is expected to be about 10°C more than that of polystyrene [101].

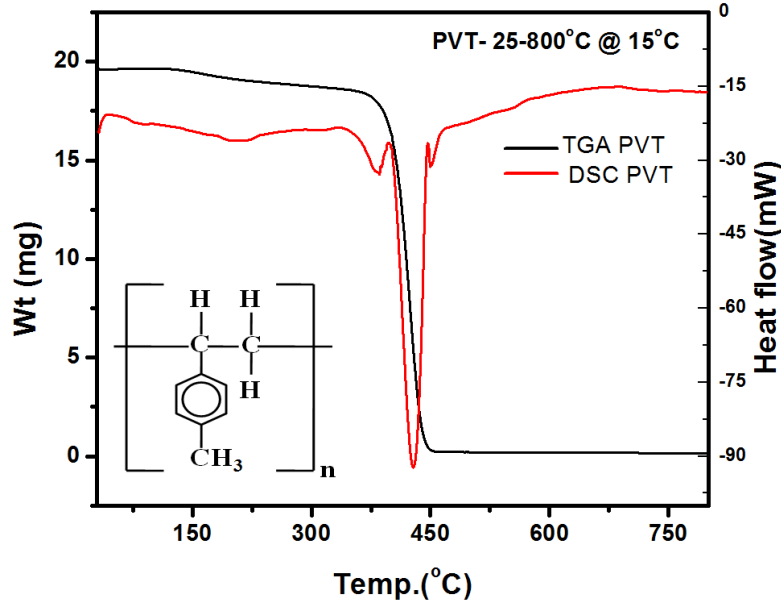


Figure 4. 2. The thermogravimetric analysis (TGA) and differential scanning calorimetry (DSC) profiles of the PVT, recorded at a heating rate of 15°C per minute, under N<sub>2</sub> atmosphere. The inset in figure 4.2 shows the chemical structure of PVT.

### 4.3. Shock pressure estimation

#### 4.3.1. Shock pressure estimation inside polystyrene

The peak pressure in aluminum foil induced by laser irradiation for glass confinement is calculated by using relation 2.1 [45]. The principal Hugoniot for Al and polystyrene can be written as-

$$U_s = C_0 + SU_p \quad (4.1)$$

where  $U_s$  and  $U_p$  are the shock and particle velocities respectively;  $C_0$  (sound velocity in the bulk) and  $s$  (shock parameter) are materials specific parameters listed in table 4.1 [102].

**Table 4. 1.** Parameters used for Hugoniot and shock pressure calculations, where Hugoniot is expressed as  $U_s = C_0 + Su_p$

Material	Density $\rho_0$ ( $\text{g cm}^{-3}$ )	$C_0$ (km/s)	$S$
Al- foil	2.70	5.160	1.250
polystyrene	1.048	2.310	1.47

The shock pressure inside the sample is calculated by utilizing impedance mismatch technique, using initial sample densities (Aluminum,  $2.7 \text{ g/cm}^3$ ; polystyrene,  $1.048 \text{ g/cm}^3$ ); and Hugoniot used are  $U_s = 5.16 + 1.25u_p$  for Al and  $U_s = 2.494 + 1.47u_p$  for polystyrene, where  $U_s$  is shock velocity and  $u_p$  is particle velocity [103], [104]. The Hugoniot plots are done by taking the EOS data from SEASME and QEOS. Figure 4.3 (a) shows the plot between pressure and particle velocity for Al and polystyrene at a laser intensity of  $1.94 \text{ GW/cm}^2$ . Similar calculations are done for all laser intensities. The estimated pressure values calculated here using impedance mismatch technique are found in good agreement with the average pressure values of 1D hydrodynamic simulations for the same laser intensity and is shown in figure 4.3 (b).

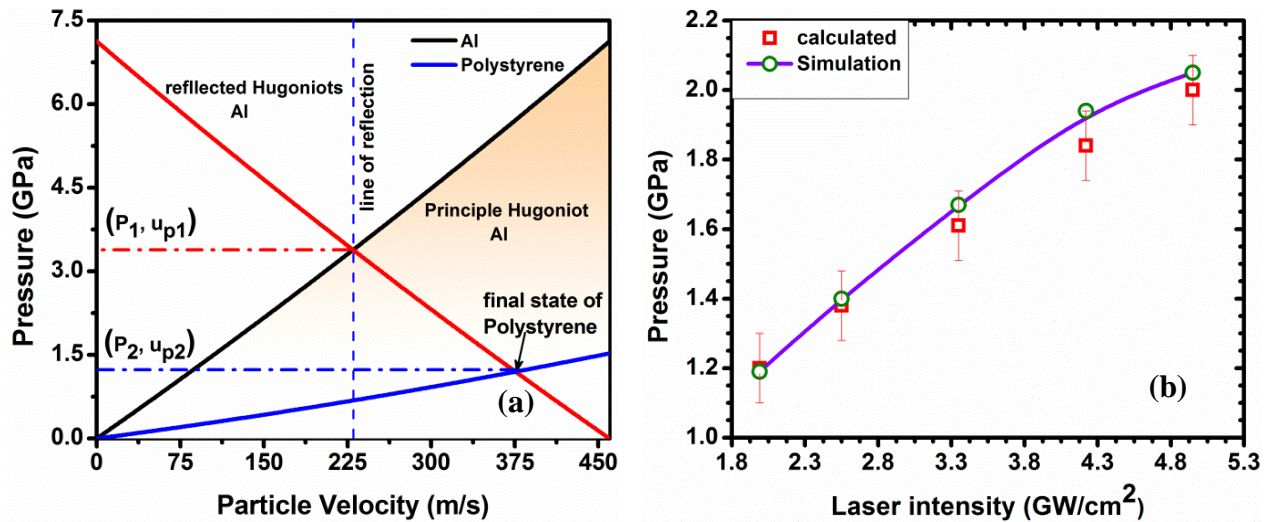


Figure 4. 3. (a) Calculated instantaneous pressure in Al and polystyrene behind the shock front using the impedance mismatch technique with the known sample Hugoniot (b) shows impedance

mismatch and simulation pressure variation with laser intensity.

#### 4.3.2. Shock pressure estimation inside PVT

The shock pressure inside the PVT as a function of laser intensity are estimated by using 1D radiation hydrodynamic code (THRD) [105]. In this model, the electrons and ions can have different temperatures (i.e.  $T_i \neq T_e$ ). However, they are assumed to have same macroscopic fluid velocity. The laser pulse used for simulations has a wavelength of 1064 nm and Gaussian temporal profile with FWHM of 8 ns. Whole simulation region is divided into two regions, 50  $\mu\text{m}$  thick Al foil and 200  $\mu\text{m}$  thick PVT sheet. Each region has grids of 100 and 200 cells respectively. The laser pulse is focused on the first cell of Al foil. The laser energy absorbed near the critical surface transported into the Aluminium foil by electronic heat conduction. The heated material is blown off the target, and this ablation drives a shock wave into the Al-foil ahead of the ablating surface. This generated shock wave reaches the Al-PVT interface at a time of about 17.5 ns and reached to maximum at about 21 ns. The estimated average pressures inside PVT at laser intensities; 1.6, 2.4, 3.2 and 4.5  $\text{GW}/\text{cm}^2$ , are found as 1.04, 1.31, 1.58 and 2.25 GPa respectively.

#### 4.4. Grüneisen parameter and bond anharmonicities

The Gruneisen parameter is a very familiar quantity in solid state physics. It can be defined from a thermodynamic point of view in terms of pressure and internal energy [106]

$$\gamma = V(\partial P / \partial V)_V \quad (4.2)$$

$$= V\alpha/kC_V \quad (4.3)$$

where  $\alpha$  – thermal expansion coefficient,  $k$  – compressibility and  $C_V$  – heat capacity at constant volume.

For a collection of quasi-harmonic oscillators of frequency  $\nu_i$ , it can be shown that [107]

$$\gamma = \sum_i (C_i/C_V) (-\partial \ln \nu_i / \partial \ln V) \quad (4.4)$$

where  $C_i$  is the heat capacity due to the  $i^{\text{th}}$  frequency  $\nu_i$ .

If all the frequencies have the same volume dependence, then Grüneisen parameter can be written as

$$\gamma = (-\partial \ln \nu / \partial \ln V) \quad (4.5)$$

For simple metals  $\gamma$  is a constant and close to 2 hence, for metals the normal frequencies are proportional to  $V^{-2}$ .

However, in polymers the Grüneisen parameter is not a constant and is observed to vary noticeably with temperature and pressure. An understanding of  $\gamma$  would provide insight into the nature of polymeric solid state, particularly its equation of state [107]. The magnitude of  $\gamma$  calculated for many common polymers from experimental thermal expansion, compressibility and heat capacity measurements is typically  $< 1$ , for temperature above 200K [108]. Examination of the thermodynamic definition of the Grüneisen parameter suggests that  $\gamma$  can be considered to be a coupling parameter between mechanical and heat effects. In other words, the Grüneisen parameter can be interpreted as the thermoelastic stress in a material exposed to an impulse of energy. In fact, energy deposition measurements have been used to obtain Grüneisen parameters which agree well with those obtained from measured compressibility, thermal expansion, and heat capacity [106], [107], [109], [110].

There is bigger difficulty in dealing adequately with the vibrations of more complicated structures in terms of a single model. However, the limited objective of relating Grüneisen constants, bond anharmonicities and pressure-induced frequency shifts can be achieved for the

simplest situations. The insight into these is useful as a starting approximation for further discussions of more realistic models.

Using a standard definition of the mode Grüneisen parameter  $\gamma_i$  [111]

$$\gamma_i = -\frac{d \ln(\nu_i)}{d \ln(V)} = -\frac{V}{\nu_i} \left( \frac{d\nu_i}{dV} \right) \quad (4.6)$$

$$\text{or, } [\nu_i(P)/\nu_i(0)] = [V(0) / V(P)]^{\gamma_i} \quad (4.7)$$

where  $\nu_i(P)$  is the vibrational frequency at an applied pressure P,  $V(P)$  is the volume of the bulk solid at pressure P, and  $\gamma_i$  is the Grüneisen parameter for vibrational mode i.

An accurate measurement of mode Grüneisen parameter is important for characterizing the shock induced/solid state detonation chemistry [40]. If the mode Grüneisen parameters are assumed to be same for all vibrational modes, then one can obtain bulk or average Grüneisen parameter ( $\gamma$ ) by differentiation of the equation of state with respect to temperature. The bulk Grüneisen parameter is useful in modeling bulk thermodynamic changes associated with shock. Such kind of analysis is not able to describe non-equilibrium or mode specific dynamics during the shock. The chemical reactivity depends exponentially on temperature and temperature of a shock wave depend exponentially on Grüneisen constant [110], [112] so the mode specific chemical reactions are expected to be extremely sensitive to the mode Grüneisen parameters.

## **4.5. Results and Discussion**

### **4.5.1. Vibrational spectroscopy of polystyrene and PVT under shock compression**

#### **4.5.1.1. Spectroscopic analysis of Polystyrene under shock compression**

Raman spectra as a function of different shock pressure for polystyrene are recorded. Figure 4.4 shows typical Raman spectra for polystyrene under various shock compression with the un-shocked Raman spectrum as a reference for peak shift. All the vibrational modes observed in the study show inhomogeneous broadening, shift to higher

wavenumbers and decrease in intensity, as the pressure is increased. As the intensity of the Raman mode depends on the vibrational mode induced changes in the polarizability of molecule, the observed pressure induced variations in the intensities would be a measure of the variations in the polarizability derivative (with respect to normal coordinates of interest) i.e. the drop in intensity at higher pressure is because of change in polarizability of the respective modes. Second, in the case of dynamically shocked samples, at a chosen time delay, the volume of unshocked sample reduces with increasing shock pressure. Therefore, the intensity of the ambient modes decreases with increasing pressure. In contrast, increasing shocked volume shows up as increasing intensity of shifted Raman peak (appearing as new mode). The observed broadening of the peak indicates overlapped Raman signals from shocked and unshocked regions. The several Raman active vibrational modes studied and investigated under shock compression are given in table 4.2. The table 4.2 consists of Raman wavenumber ( $\text{cm}^{-1}$ ) of polystyrene at ambient pressure and their assigned vibrational modes as given by Anema et al. [113], and references therein along with their symmetries.

To understand the effect of shock compression on fundamental Raman modes of polystyrene the peak positions and FWHM of these modes are analyzed. The details of the separate peaks and shock loading for the  $1004$  and  $1034 \text{ cm}^{-1}$ , modes are shown in figure 4.5. As the shock front moves into the sample, the Raman peaks start broadening. To obtain the peak shift information, spectra under shock compression are analyzed by fitting double Gaussian peaks, shown as dashed curves.

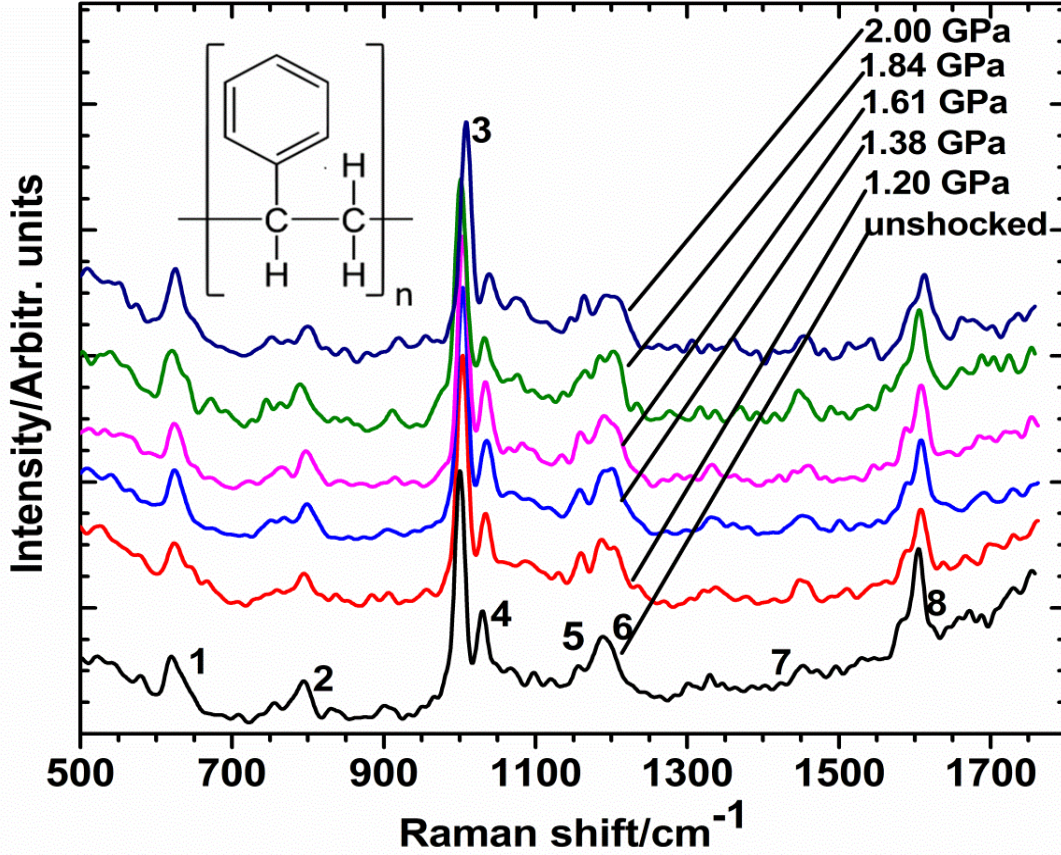


Figure 4. 4. Normalized Raman spectra of polystyrene as a function of shock pressure for the range 100–1800  $\text{cm}^{-1}$ ; and the unshocked spectrum shows Raman spectrum of Polystyrene ambient pressure and temperature. The labels above the peaks are references to their mode assigned as in the table 4.2.

**Table 4. 2.** Raman active vibrational modes analyzed under shock compression and mode dependent Grüneisen parameters ( $\gamma_i$ )

Labels	Frequency ( $\text{cm}^{-1}$ ) at ambient pressure	Mode assignment with Symmetry and references	Under pressure		$\gamma_i$
			$\frac{dv}{dP}(\text{cm}^{-1}/\text{GPa})$		
			a	b	
1	625	6b $B_2 \alpha_{yz}$ [95], [113]– [117]	1.88	1.3	$0.036 \pm 0.0042$

2	798	1A <sub>1</sub> α <sub>xx</sub> α <sub>yy</sub> α <sub>zz</sub> [95], [113], [115], [116]	4.95	4.6	0.073±0.0059
3	1004	12A <sub>1</sub> α <sub>xx</sub> α <sub>yy</sub> α <sub>zz</sub> [113], [95], [115]	2.50	2.5	0.030±0.0005
4	1034	18aA <sub>1</sub> α <sub>xx</sub> α <sub>yy</sub> α <sub>zz</sub> [95], [113]–[115], [117]	3.47	3.4	0.040±0.0008
5	1165	15 B <sub>2</sub> α <sub>yz</sub> [95], [113]– [115], [117]	1.97	2.6	0.020±0.0030
6	1195	13A <sub>1</sub> α <sub>xx</sub> α <sub>yy</sub> α <sub>zz</sub> [95], [113]–[115]	2.05	2.0	0.021±0.0021
7	1456	19b B <sub>2</sub> α <sub>yz</sub> [95], [113], [115], [117] and δ(CH <sub>2</sub> ) [113]–[115], [117]	0.82	1.0	0.007±0.0011
8	1606	8a A <sub>1</sub> α <sub>xx</sub> α <sub>yy</sub> α <sub>zz</sub> [95], [113]–[115]	3.50	3.5	0.027±0.0006

<sup>a</sup> dv/dP from experimental data.

<sup>b</sup> see reference [113].

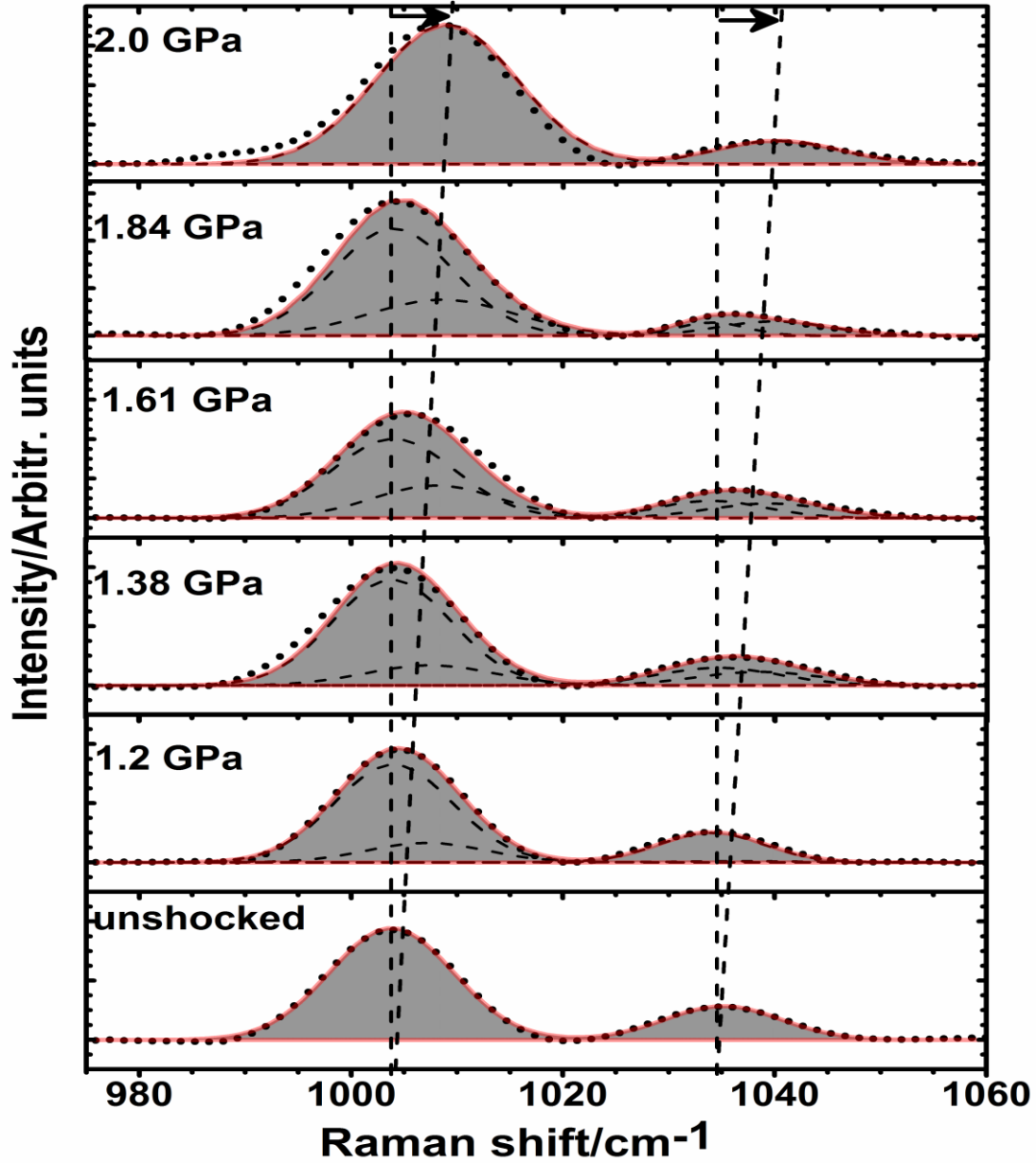


Figure 4. 5. Raman blue shift of  $1004$  and  $1034\text{ cm}^{-1}$  modes, under dynamic shock compression with the unshocked Raman spectrum as a reference for peak shift under pressure. The dots in the figure 4.5 are the original experimental data, and the dashed lines are the fitted Gaussian function. The dashed vertical line measures Raman peak shift under shock compression.

All of these Raman peaks are blue shifted monotonically and linearly with pressure [118]. The fitted results are shown by the solid lines in figure 4.6. These results also show that the experimental data under shock compression is in good agreement with hydrostatic compression experiments. This signifies that all the changes in the Raman peaks are mainly because of shock pressure with hardly any temperature effects. The reason behind this may be that the temperature increase in the sample because of shock propagation is not much under the present experimental shock compression conditions.

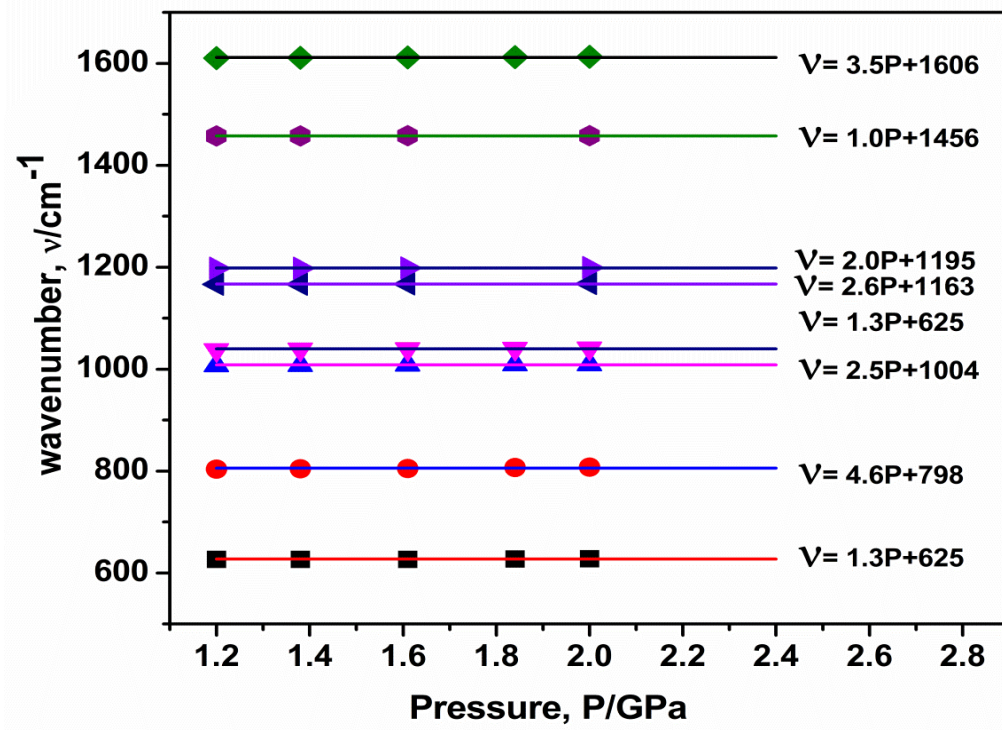


Figure 4. 6. Pressure-dependent behaviors of observed Raman modes of polystyrene. The symbols show experimental data, and solid lines show the linear fit to the data under hydrostatic compression taken from reference [118]. Here error bars are comparable to the size of the symbols.

From table 4.2, it can also be noticed that shift of the vibrational peak at  $798\text{ cm}^{-1}$  ( $4.95\text{cm}^{-1}/\text{GPa}$ ) is more sensitive to the pressure than other vibrational modes. Unlike  $798\text{ cm}^{-1}$  mode, the bending mode of  $\text{CH}_2$  at  $1456\text{ cm}^{-1}$  showed much smaller change over the pressure range studied. This implies that the  $\text{CH}_2$  bending mode is not much deformed or remains much more intact than the other modes below 2 GPa. There is no evidence for any change in the slopes of the pressure–wavenumber plots [ $d\nu/dP$  ( $\text{cm}^{-1}/\text{GPa}$ )] under the present shock compression conditions. From the observed monotonic changes of all observed vibrational modes with pressure, it can be concluded that aPS does not undergo any conformational changes under shock compression up to 2 GPa.

#### 4.5.1.2. Pressure dependent Raman line width

The shock compression effect on full width at half maximum for some observed Raman peaks is shown in figure 4.7, and average change over 0 to 2.0 GPa is summarized in table 4.3. Straight lines have been drawn as guides for the eye. The changes in the FWHM of Raman peaks are mainly caused by pressure dependence of Raman modes and because of increased molecular interaction. This increased molecular interaction can lead to the deformation of molecular structure.

**Table 4. 3.** Changes in Raman line width under shock compression

$\nu_0$ ( $\text{cm}^{-1}$ )	$\Delta\nu_{FWHM}$ ( $\text{cm}^{-1}$ ) at ambient pressure	$\Delta\nu_{FWHM}$ ( $\text{cm}^{-1}$ ) at 2.0 GPa
625	19.58	24.22
798	15.42	9.33
1004	12.38	14.28
1034	8.998	13.93
1165	9.85	11.17

1195	10.26	12.77
1456	17.59	12.32
1606	8.94	9.77

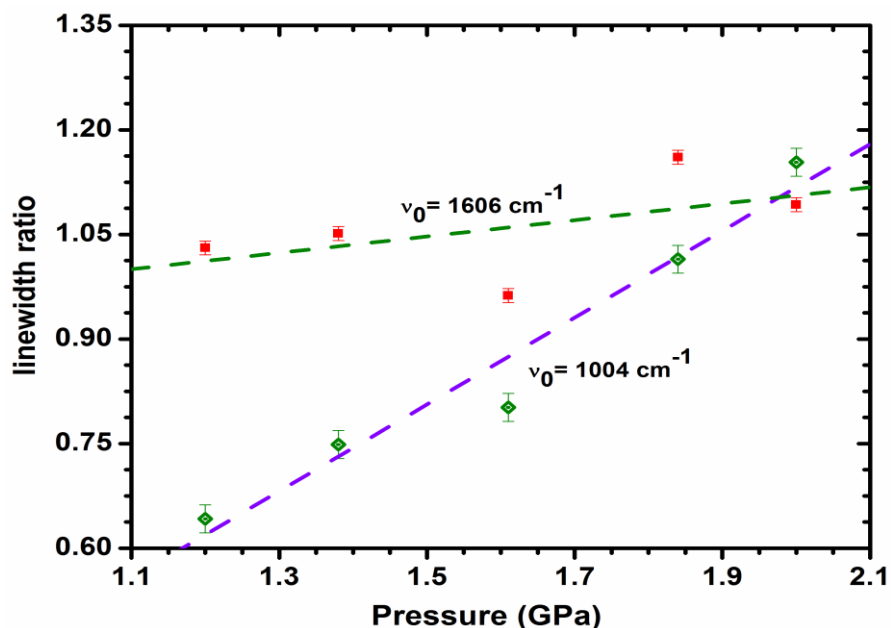


Figure 4. 7. Changes in Raman line widths ( $I_{\text{shocked}}/I_{\text{unshocked}}$ ) under shock compression for two fundamental modes of aPS.

#### 4.5.2. Spectroscopic analysis of PVT under shock compression

Liang and Krimm [115] have previously denoted the  $1001 \text{ cm}^{-1}$  mode as the  $\nu_1$  totally symmetric stretching (ring stretching) mode for polystyrene. In their study of large group mono-substituted benzenes, Katritzky [119] reported that the wavenumber corresponding to  $\nu_{8a}$  (C-C ring stretching) vibrations are  $1604 \pm 3 \text{ cm}^{-1}$ . For polystyrene  $\nu_1$  corresponds to  $1004 \text{ cm}^{-1}$ , while  $\nu_{8a}$  corresponds to  $1606 \text{ cm}^{-1}$  fundamental vibrational modes. The Raman scattered light from the shocked PVT is collected to the Raman spectrometer in confocal geometry. Raman spectra for PVT at various static and shock pressure are recorded with the ambient or unshocked spectrum

as a reference for peak shift and are shown in figure 4.8 (a) and (b). All observed mode shows inhomogeneous broadening, shift to higher wave number and decrease in intensity as the shock pressure is increased. The Raman signal of modes at 1031 and 1602  $\text{cm}^{-1}$  are merged with the noise and difficult to measure at higher shock pressures ( $> 2$  GPa).

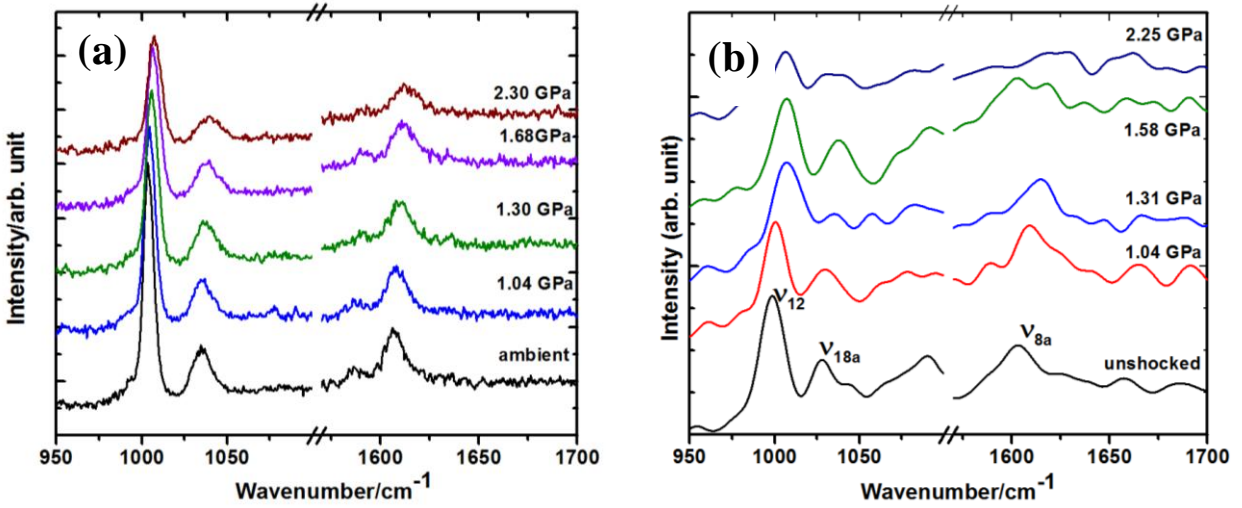


Figure 4. 8. Raman Spectrum of fundamental modes of PVT (a) under static compression for the range 950-1700  $\text{cm}^{-1}$  (b) under shock compression for the range 950-1700  $\text{cm}^{-1}$ .

Figure 4.9 shows the Raman spectrum of  $\nu_{12}$  mode at 1001  $\text{cm}^{-1}$  as a function of shock pressure with unshocked spectrum as a reference for peak shift. As the shock front moves into the sample, the Raman peaks starts broadened because of overlap of Raman peaks from shocked and unshocked regions. To obtain the peak shift information; spectra under shock compression are analyzed by fitting double Gaussian peaks, using peak analyzer in Origin Pro 9.1 software. The details of the separate peaks under different shock loading for the  $\nu_{12}$  mode at 1001  $\text{cm}^{-1}$  are shown in figure 4.9. The values of  $R^2$  in our case for the peak at 1001  $\text{cm}^{-1}$ , shown in the figure 4.9 at the pressures 1.04, 1.31, 1.58 and 2.25 GPa are 0.997, 0.992, 0.999, and 0.997 respectively. The blue circles in the figure 4.9 are the experimental data points, and the dashed lines are the fitted Gaussian functions. The red curve lines are the cumulative fitting of the data,

and the dashed black lines measure Raman peak shift under shock compression. The similar kind of analysis is performed for the other fundamental Raman modes of PVT.

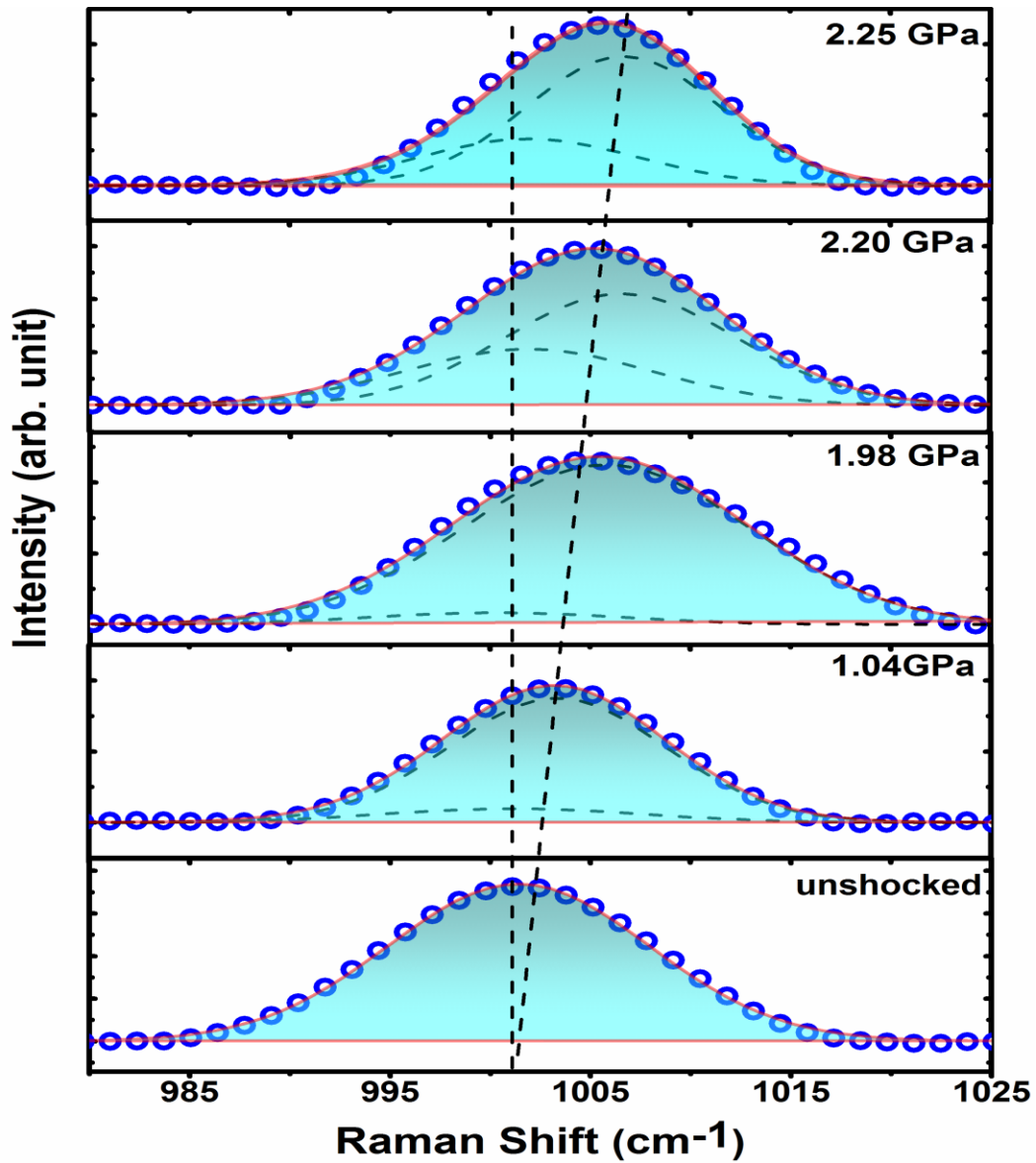


Figure 4. 9. Raman blue shift of  $\nu_{12}$  mode at  $1001 \text{ cm}^{-1}$  under dynamic shock compression. The open circles in the figure 4.9 are the original experimental data and the dashed lines are the fitted Gaussian function. The dashed black line measures Raman peak shift under shock compression.

The Raman modes  $\nu_{12}$  (C-C-C ring bending mode) [115], [120] at  $1001\text{ cm}^{-1}$ ,  $\nu_{18a}$  mode [115][120] at  $1031\text{ cm}^{-1}$  and  $\nu_{8a}$ (C-C ring stretching mode) [115], [121] at  $1602\text{ cm}^{-1}$ , under shock compression and static pressure along with wavenumber shift of PVT are plotted in figure 4.10. All observed modes show a proportional relation with static pressure. The relationship between the static pressure induced peak shift ( $\nu$ ) and pressure ( $P$ ) for  $1001$ ,  $1031$  and  $1602\text{ cm}^{-1}$  modes; are well fitted by linear equations:  $\nu = 1001 + 2.33P$ ,  $\nu = 1031 + 3.08P$  and  $\nu = 1602 + 3.94P$  respectively.

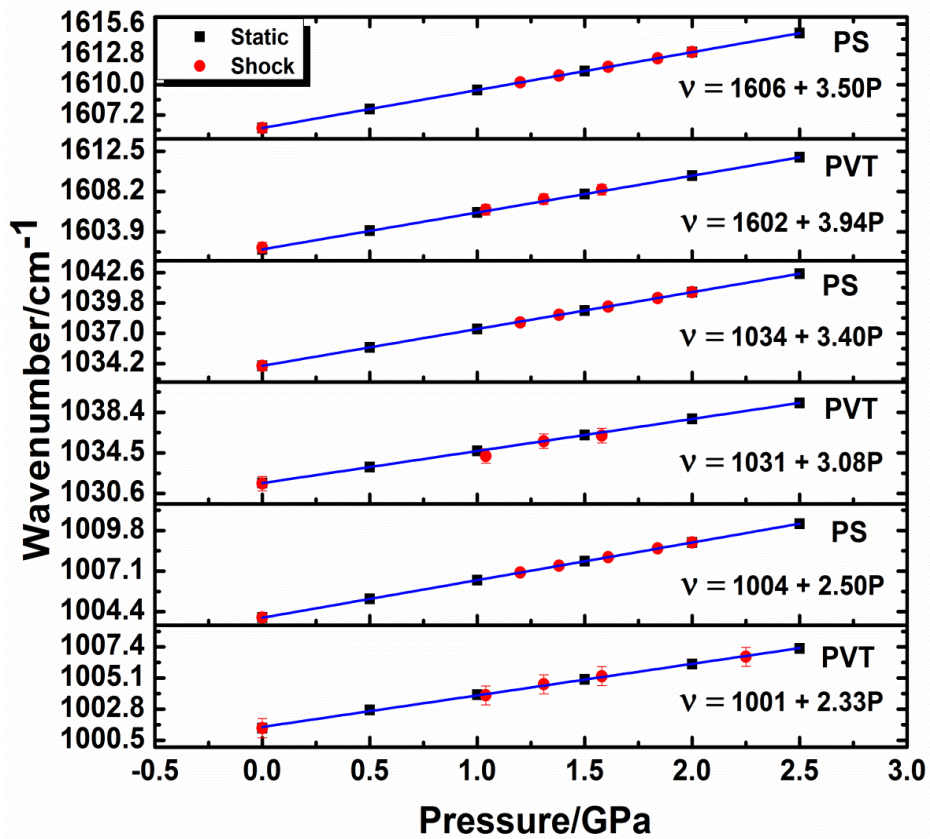


Figure 4. 10. Pressure dependent behavior of PVT and polystyrene (PS) under static and shock wave compression. Where symbols shows the experimental data for Raman wavenumber shift under static and shock compression, and the solid lines show linear fit to the static compression data.

Using these linear equations the shock pressure inside PVT for different laser intensities can also be estimated. From figure 4.10, it is clear that the shift due to shock compression for the modes 1001, 1031 and 1602  $\text{cm}^{-1}$  are following almost the same linear equation as in case of static compression for these modes. The peak shift data of PVT is also compared with the peak shift of similar kind of modes of polystyrene to see if any general trend can be established and is shown in figure 4.10. The observed Raman wavenumber of the corresponding bonds are lower in PVT comparison to polystyrene [47]. This is because of a heavier group  $\text{CH}_3$  is attached with the PVT. Due to which the total reduced mass increases which cause a decrease in the vibrational wavenumber of the corresponding bonds in PVT. The slopes of fits in figure 4.10 for PVT and polystyrene are comparable. However, the intensity of the peaks at 1031 and 1602  $\text{cm}^{-1}$  modes of PVT show drastic decrease at higher laser intensities (under higher shock pressures) and signals are difficult to identify from the noise. The reason behind this may be an increase in the fluorescence at higher laser intensities, which become comparable to the signal level.

There is no evidence observed for changes in the slopes of the wavenumber-pressure plots [ $\text{dv}/\text{dP}$  ( $\text{cm}^{-1}/\text{GPa}$ )] to 2.25GPa, for PVT and polystyrene. This indicates no chemical processes involved in making and/or breaking intramolecular bonds occurred at present experimental conditions. The 1602  $\text{cm}^{-1}$  C-C ring stretching mode of PVT shifted at an average rate of 3.94  $\text{cm}^{-1}/\text{GPa}$ . This is higher than the Raman active mode of polystyrene at 1606  $\text{cm}^{-1}$ , which is shifted by an average of 3.50  $\text{cm}^{-1}/\text{GPa}$  over the same pressure range. The slopes of the plot indicate that the anharmonicity with pressure. Both the polymers are showing higher anharmonicity, for higher frequency modes. But in case of PVT, it is observed that the higher frequency modes are showing greater anharmonicity with the pressure.

### 4.5.3. Density independent Grüneisen parameter and bond anharmonicities analysis

#### 4.5.3.1. Density independent Grüneisen parameters for local modes of polystyrene

The mode independent Grüneisen parameters are estimated for several Raman active modes of polystyrene and are given in table 4.2. It is observed that all the peaks are shifted and inhomogeneously broadened with pressure because of the increased inter-atomic interactions. In the present study the temperature variation due to shock gradient within the sample with shock wave propagation may also contribute to the inhomogeneous peak broadening. The plots of the  $\ln[v_i(P)/v_i(0)]$  vs  $\ln[V(0)/V(P)]$  for several fundamental modes of polystyrene are shown in figure 4.11. The volume of polystyrene as a function of shock compression are taken from Marsh and Bridgeman's data [122], [123]. From equation 4.7, the slopes of the linear fits in figure 4.11 correspond to  $\gamma_i$  for each fundamental mode. The  $\gamma_i$  for the  $798\text{ cm}^{-1}$  mode of polystyrene ( $\gamma_1 = 0.073 \pm 0.0059$ ) is considerably larger than the one for the  $1456\text{ cm}^{-1}$  mode ( $\gamma_2 = 0.007 \pm 0.0011$ ). This difference in  $\gamma_1$  and  $\gamma_2$  indicates either a greater anharmonicity in the potential energy surface for the  $798\text{ cm}^{-1}$  mode or that the local volume compression near this coordinate is greater than for the  $1456\text{ cm}^{-1}$  mode. Generally, vibrational bands decrease in intensity and shift to higher wavenumber as the compression is increased. For a purely harmonic potential, the vibrational frequency is volume independent i.e.  $\gamma = 0$ , so the magnitude of each  $\gamma_i$  is a measure of bond anharmonicities of the particular vibrational mode [109], [124]. The magnitude of  $\gamma_i$  for each observed Raman active modes are summarized in table 4.2. This explains the tendency of force constant  $k$ , and consequent change in corresponding vibrational frequency.

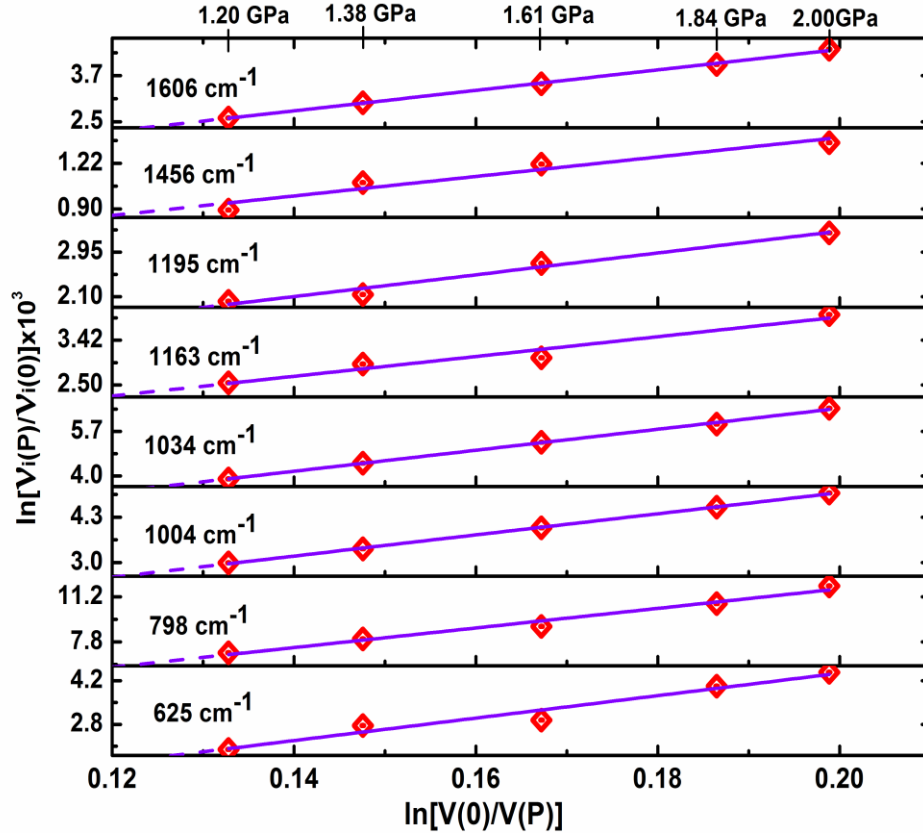


Figure 4. 11. A log-log plot of the  $\nu_i(P)/\nu_i(0)$  vs  $V(0)/V(P)$  for all analyzed peaks of polystyrene. The graph shows the tendency of the vibrational modes to be individual volume independent Grüneisen parameters.

Figure 4.11, clearly shows the volume independence of mode Grüneisen parameters under compression range 1.2 to 2.0 GPa. This can be explained by considering two different regimes (i) low pressure compression (ii) high pressure compression. In the low pressure compression, the compression mainly involves removal of void space within the bulk polymer without significantly compressing the molecular bonds themselves. Whereas, in the high pressure compression the polymer chains are pushed closer together and the bond length start to decrease [16]. All the modes are found to have volume independent Grüneisen parameter above

1.2 GPa and are consistent with the previous measurements done on the various polymers [111], [125] using diamond anvil cell technique.

#### 4.5.3.2. Density independent Grüneisen parameters for local modes of PVT

The value of individual mode Grüneisen parameters provides the information about the intermolecular potentials and nature of the compression. To determine the individual mode Grüneisen parameters, the compression of material as a function of pressure must be known. A one dimensional numerical simulation is performed to determine the fractional compressibility of PVT as a function of pressure below 15 GPa. The simulation data shown in figure 4.12, is fitted by a function

$$\frac{V(0)}{V(P)} = \left[ 1 + \frac{P(\text{GPa})}{0.36(\text{GPa})} \right]^{0.068} \quad (4.8)$$

This formula is used here for the compressibility measurements in this study.

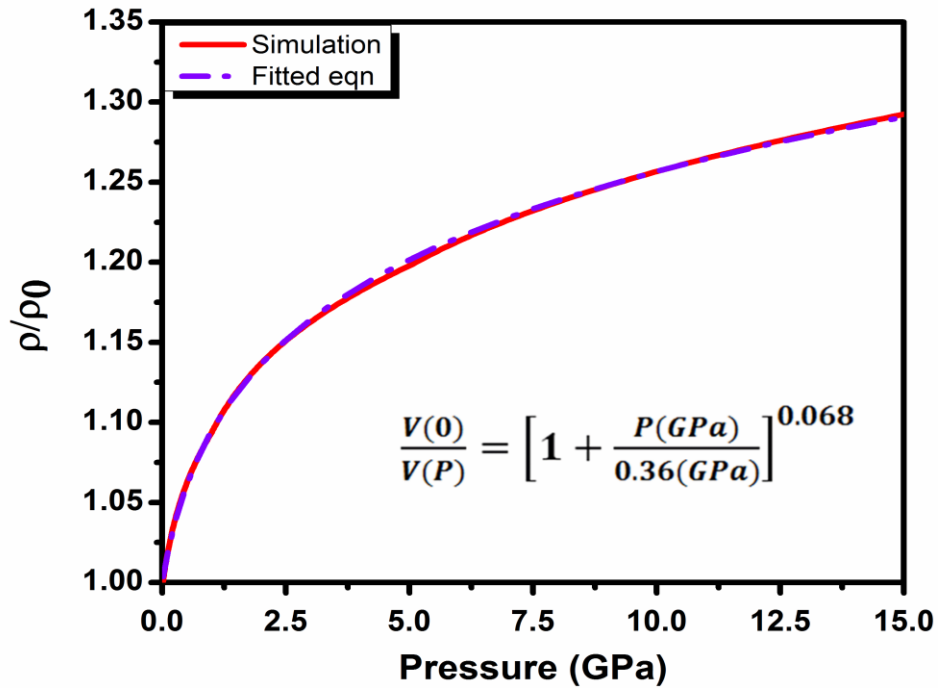


Figure 4. 12. Fractional compressibility ( $\rho/\rho_0$ ) of PVT for pressures below 15 GPa.

Sherman [109], [124] model, involving fairly general potentials, predicts that if the bond lengths decrease by 1%, for typical potentials the vibrational frequencies will increase by an amount of the order of 10%. For the final pressure of 2.5 GPa for the present experiment, the bond frequencies of PVT shifted by an amount of 0.6% to 0.8% from the ambient pressure value. Thus the changes in the bond length are of the order of 0.06-0.08%. In contrast, the changes in volume for the corresponding pressure are  $\approx 15\%$ . This clearly indicates that the primarily volume changes (below 1GPa) are due to free volume and compression of the inter-chain bonds, and not because of changes in intermolecular bond lengths [17], [109], [124]. Data from static and shock compression experimental results are analyzed to determine the individual mode Grüneisen parameters. A log-log plot for observed vibrational modes of PVT with fractional change in volume is shown in figure 4.13. All the vibrational modes are found to have volume independent Grüneisen parameter for the present experimental pressure range and are consistent with the earlier reported measurements on various polymers [17][16]. The calculated mode independent Grüneisen parameters for each observed Raman active modes are listed in table 4.4.

**Table 4. 4.** Table of Volume independent Gruneisen parameters,  $\gamma_i$

Observed Modes	$\Delta\nu/\Delta P$ (cm <sup>-1</sup> /GPa)	$\gamma_i$
$\nu_{12}$	2.33	0.0655
$\nu_{18a}$	3.08	0.0860
$\nu_{8a}$	3.94	0.0710

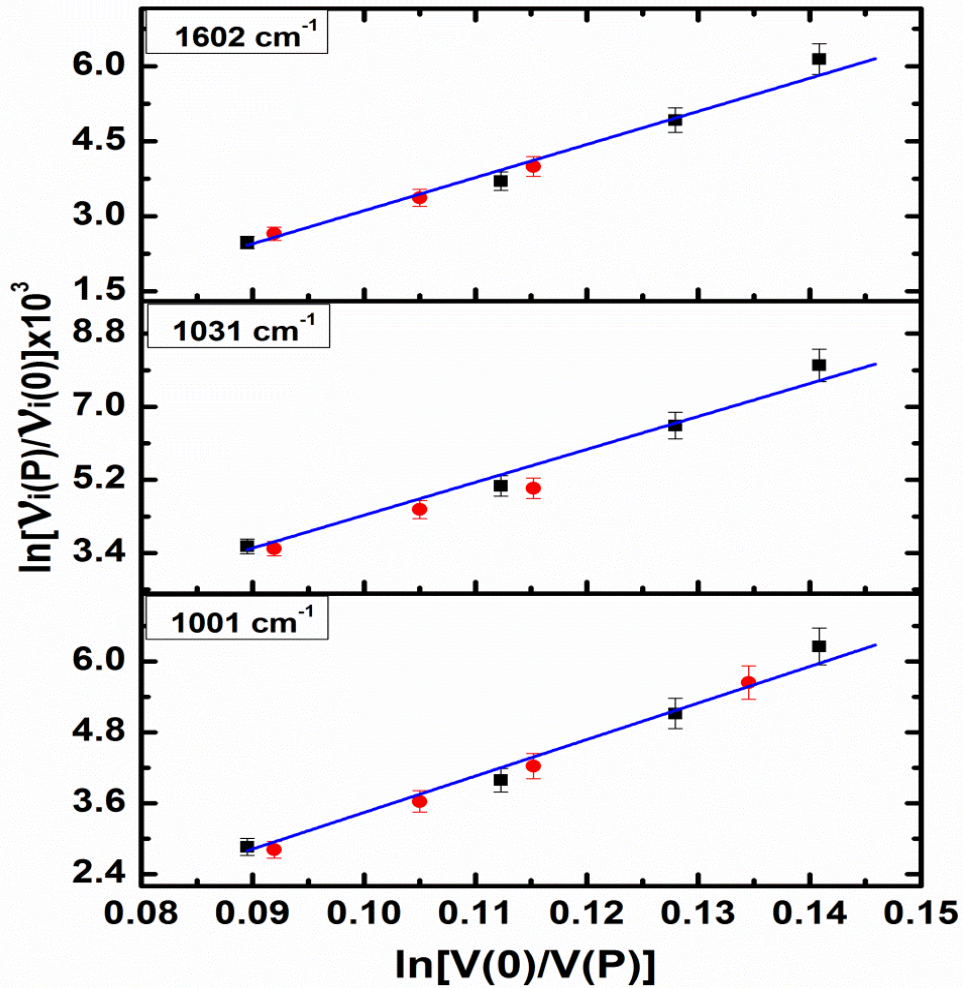


Figure 4. 13. A log-log plot of the  $\nu_i(P)/\nu_i(0)$  vs  $V(0)/V(P)$  for observed peaks of PVT under static and shock compression. The graph shows the tendency of the vibrational modes to be individual volume independent Grüneisen parameters.

#### 4.5.4. Time resolved studies of polystyrene and PVT under Shock compression

##### 4.5.4.1. Time resolved studies of polystyrene under Shock compression

The Raman spectra of polystyrene under shock pressure of 2 GPa for various delay times between pump and probe beams are recorded and are shown in figure 4.14. The observed peak at 625, 798, 1034 and 1456  $\text{cm}^{-1}$  are assigned to  $\nu_{6b}$  a radial ring stretching mode,  $\nu_1$  totally symmetric ring stretching mode,  $\nu_{18a}$  tangential C-H bending mode and  $\nu_{19b}$  or  $\delta(\text{CH}_2)$

respectively [95], [113]–[115]. While the strong peaks at  $1004$  and  $1606\text{ cm}^{-1}$  are assigned to  $\nu_{12}$  C-C-C ring bending mode and C-C ring stretching mode respectively [113], [115][95]. The peaks at  $1165$  and  $1195\text{ cm}^{-1}$  are also observed and may be assigned as  $\nu_{15}$  and  $\nu_{13}$  modes [95] [113], [114]. The identification of the peaks is taken from reference [115]. For the more detail analysis two most intense Raman modes at  $1004$  and  $1606\text{ cm}^{-1}$  are chosen.

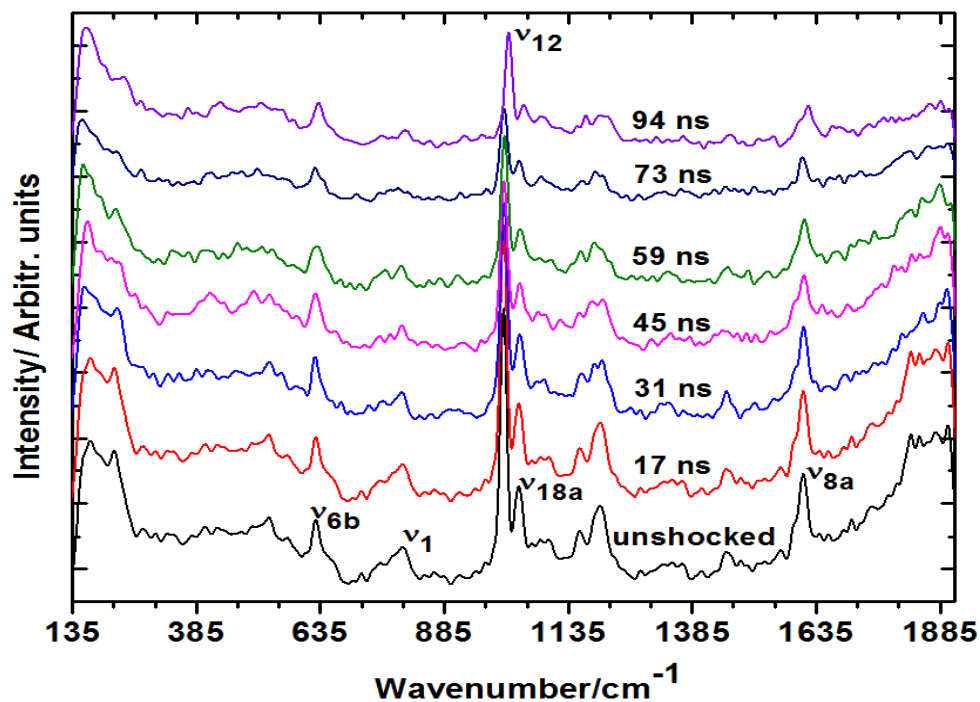
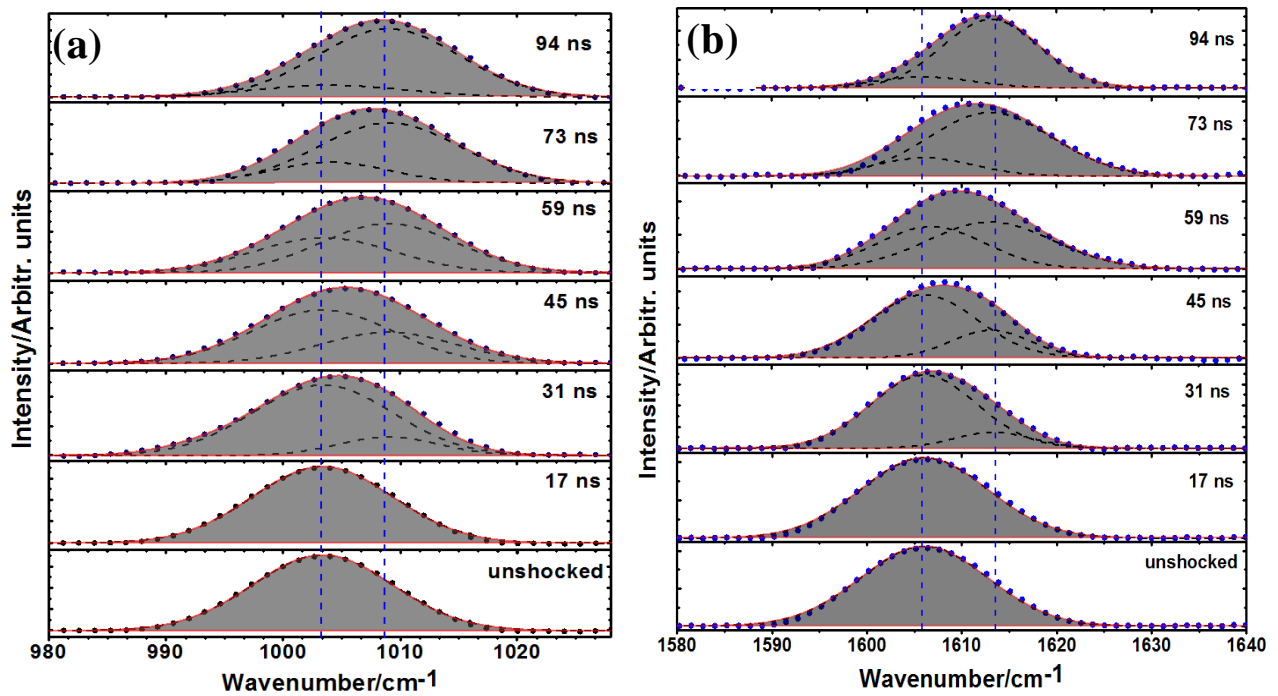


Figure 4. 14. Raman spectra of polystyrene as a function of shock delay times for the range  $135$ – $1885\text{ cm}^{-1}$ , with unshocked Raman spectrum as a reference for peak shift.

The time resolved Raman spectra of the two strong fundamental modes, C–C–C ring bending mode  $\nu_{12}$  at  $1004\text{ cm}^{-1}$  and C–C ring stretching mode  $\nu_{8a}$  at  $1606\text{ cm}^{-1}$  of the shocked Polystyrene at the delay times of  $0$ ,  $17$ ,  $31$ ,  $45$ ,  $59$ ,  $73$  and  $94\text{ ns}$  are analyzed in more detail and are shown in figure 4.15 (a) and (b) respectively. The probed signals consisted overlap intensities from shocked and unshocked volume. The recorded obtained Raman spectra are analyzed by fitting double Gaussian peaks (shown as dashed curves) in the figure 4.15 (a) and (b). The delay

time 0 ns denote the arrival of the pump beam (shock driver) on the glass–Aluminum interface. To verify experimental observations hydrodynamic simulation for shock wave travelling inside the sample up to 94 ns is performed. It is observed from the numerical simulation that, the total shock build-up and propagation time inside the 50  $\mu\text{m}$  thick aluminum foil is 22.5 ns. It can be seen from the figure 4.15 (c) that shock wave is just about to reach the Al-Polystyrene interface at 20 ns. Same can be seen from the experimental data. Figure 4.15 (a) and (b) shows that at 17 ns delay, there is no change in the Raman peak and at a delay time of 31 ns, the recorded peaks are slightly broadened due to formation of a new small peak at the higher frequency side (blue shift), for both modes. This small amplitude of the new peak is attributed to the small distance travelled by the shock wave inside the target at delay time of 31 ns.



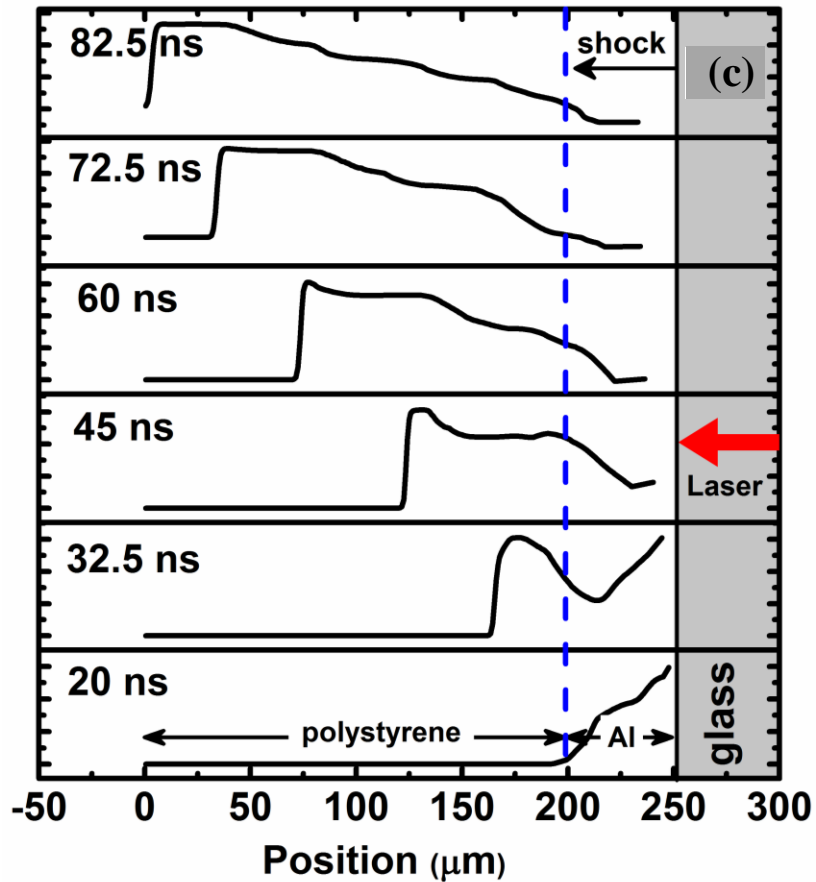


Figure 4. 15. (a) and (b) show time resolved Raman spectra of  $1004$  and  $1606\text{ cm}^{-1}$  mode at various delay times (c) Shock wave propagation inside Polystyrene at different delay times. The blue dashed line at  $200\text{ }\mu\text{m}$  shows the Polystyrene-Aluminium interface. These simulations are done by using 2D radiation hydrodynamic code.

The intensities of these new peaks increase with the increase in delay time i.e., larger distance covered by the shock wave and hence greater shock effected volume. The left Raman peaks centered at  $1004$  and  $1606\text{ cm}^{-1}$  represent the unshocked region while the right peaks at  $1009$  and  $1613\text{ cm}^{-1}$  show the shocked region [47]. The simulated spatial profile of shock wave at different time delays is shown in the figure 4.15 (c). From the simulation, it is clear that the shock wave reaches the end of the sample in  $\sim 82.5\text{ ns}$ . It can be seen from experimental results

that, at 73 ns, signal from the unshocked region is there and figure 4.15 (c) also shows that the shock wave is still inside the sample. This may go down to zero at 82.5 ns when shock wave completely arrives at the back side of the sample. A small signal is observed at 94 ns delay time which it is not following the same trend as other delays. Here, the peak intensities ratio for shocked and unshocked region starts decreasing and can be clearly seen from figure 4.16. This may be because of small contribution of reflected shock wave from the polystyrene-glass interface after the shock wave reached to the interface at 82.5 ns.

#### 4.5.4.2. Shock Velocity calculation inside Polystyrene

The shock velocity inside the sample is calculated by taking the ratios of the intensities of the shocked and total regions at different delay times. The ratio of the shocked Raman peak intensity to the total intensity vs delay time graph is plotted in figure 4.16. Here, the total intensity refers to the sum of peak intensity of the shocked and unshocked region at that delay time. In figure 4.16, filled squares and open circles in the graph show the intensity ratio variation for 1004 and 1606  $\text{cm}^{-1}$ , modes with the delay time respectively. The dotted and solid lines show the expected variation in the intensity ratio based on 1D and 2D simulations. Both the results are in very good agreement with each other and with the experimental results. It shows that the 2D effect in these experiment is negligible. By using time evolution of Raman peak intensity ratios, the shock wave velocity inside the Polystyrene sample is estimated [126] by the following equation:  $U_s = r \cdot t$ , where  $U_s$  is the shock wave velocity,  $r$  is the rate of change of Raman intensity ratio and  $t$  is the thickness of the Polystyrene. Rate of Raman intensity ratio is calculated by  $r = \frac{d}{dt} [I_s / (I_0 + I_s)]$ , where  $I_s$  is the intensity of the blue shifted peak and  $I_0$  is the intensity of the original peak. According to the above data, the fitted value of  $r$  is,  $(0.0147 \pm 0.0006) \times 10^9 \text{ s}^{-1}$ . Hence the calculated shock velocity inside the Polystyrene is  $\sim 2.9 \pm$

0.12 km/s, which is in agreement with the simulation result (3.0 km/sec). It can also be seen from figure 4.16 that, the experimental results at 94 ns show lower values, which may be due to interaction of reflected shock with rarefaction wave.

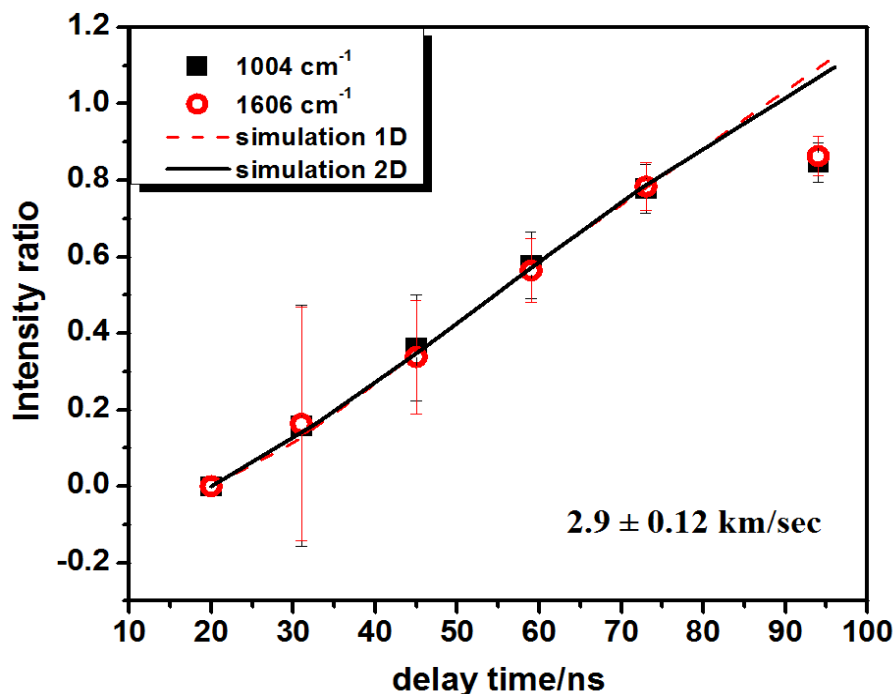


Figure 4. 16. Relative intensity ratio for the shocked to whole region of the sample vs delays time.

#### 4.5.4.3. Time resolved studies of PVT under Shock compression

The time dependent Raman spectra of  $\nu_{12}$  mode at  $1001 \text{ cm}^{-1}$  of PVT at various delay times for a fixed pressure of 2.25 GPa, is shown in figure 4.17a. It can be seen from the figure 4.17 (a) that the  $\nu_{12}$  mode at  $1001 \text{ cm}^{-1}$  of PVT show an increase in intensity in shock induced Raman peak with increase in delay time, as shock get longer time to propagate in the sample. In figure 4.17 (a), left centered peak at  $1001 \text{ cm}^{-1}$  represents the unshocked volume while peak at  $1006.6 \text{ cm}^{-1}$  represents shocked volume. The observed peak is a superposition of the Raman peaks from both shocked and unshocked volumes. Hence, the observed Raman peaks

are analyzed by double Gaussian peak fitting. The volume proportionality of Raman intensity on shocked and unshocked regions are compared with the shock wave propagation in the sample using 1D radiation hydrodynamic code shown in the figure 4.17 (b). From figure 4.17 (b) one can observe that at a delay time 17.5 ns, the shock front just reaches the Al-PVT interface. After a delay time of 24.5 ns, the shock front enters in the PVT sheet but a small portion of PVT is under shock compression. Therefore, in broadened Raman peak only a small contribution of shocked volume is seen and most of the peak intensity is because of unshocked volume. This can be seen from figure 4.17 (a).

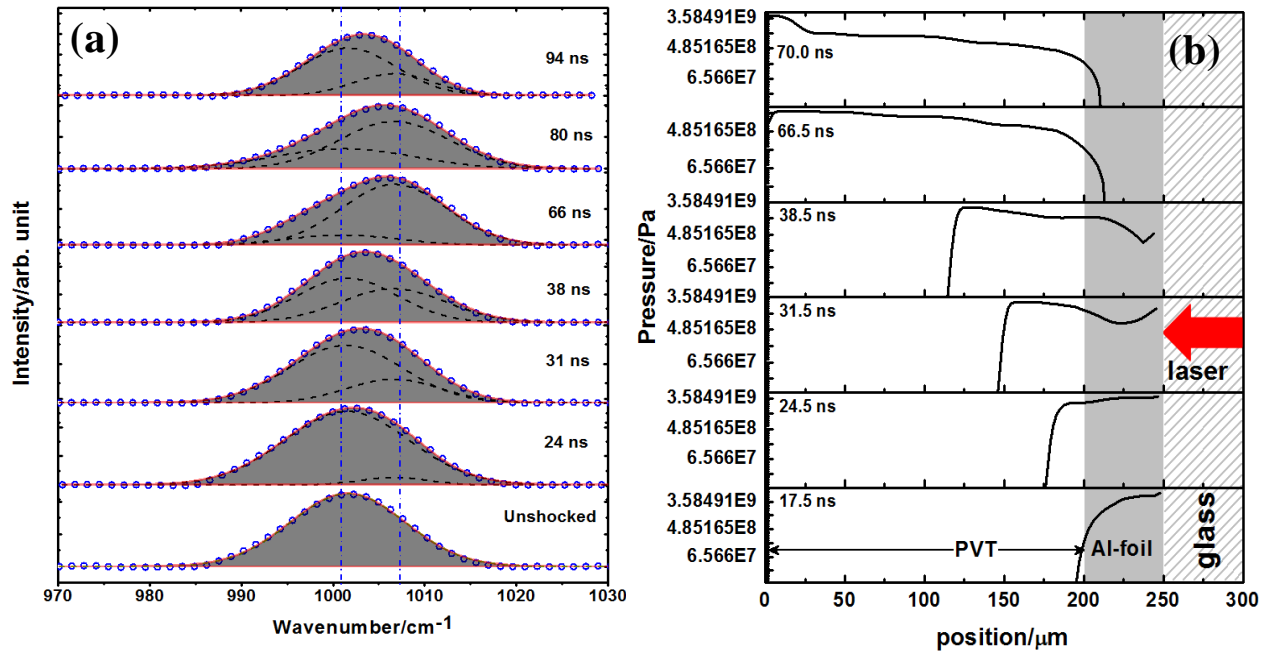


Figure 4. 17. (a) Show time resolved Raman spectra of  $\nu_{12}$  mode at  $1001 \text{ cm}^{-1}$  mode at various delay times (b) Shock wave propagation inside polystyrene at different delay times. The simulations are done by using 1D radiation hydrodynamic code.

At 38.5 ns, the shock travels around half of the sample. So, the intensity due to shocked volume is comparable to the unshocked volume. At delay time of 66 ns, it can be seen that the signal from shocked volume is much more than the signal from unshocked volume. Same can be

seen from the simulation results at 66.5 ns delay that the shock has reached almost up to the end of the sample and it completely passes the sample at  $\sim 70$  ns time delay. In the experimental data shown in figure 4.17 (a) for delay 80 ns and 94 ns, the intensities of shocked volume is decreasing while from unshocked volume is increasing. This indicates that the behavior of the mode at  $1001\text{ cm}^{-1}$  is reversible up to 2.25 GPa.

The shock velocity inside PVT can be calculated by plotting the ratio of shocked signal to the total with respect to delay time. At delay times of 24, 31, 38 and 66 ns, the Raman intensity ratio belonging to the shocked volume are 0.053, 0.256, 0.446 and 0.852 respectively. By using equation [127]:  $U_s = r \cdot t$ ; where  $U_s$  is the shock velocity,  $r$  is the intensity ratio and  $t$  is the thickness of the PVT sheet, the calculated shock wave velocity is 3.6 km/s. This is in good agreement with the shock velocity deduced from the hydrodynamic simulation within experimental error (4.3 km/s). The detail procedure of shock velocity measurement is discussed in previous section.

#### 4.6. Conclusions

The shock pressure induced shifts of the vibrational modes common to both aromatic systems are almost similar. The changes in vibrational frequencies of fundamental Raman peaks have been observed with respect to shock wave propagation. The fundamental modes of both polymers show a linear relation with static pressure. The relationship for polystyrene and PVT between the pressure induced peak shift ( $\nu$ ) with pressure ( $P$ ) for the similar kind of modes are found as,  $\nu = 1004 + 2.50P$ ;  $\nu = 1034 + 3.40P$ ;  $\nu = 1606 + 3.50P$  and  $\nu = 1001 + 2.33P$ ,  $\nu = 1031 + 3.08P$  and  $\nu = 1602 + 3.94P$  respectively [128]. There is no evidence observed for changes in the slopes of the peak shift–pressure plots [ $d\nu/dP$  ( $\text{cm}^{-1}/\text{GPa}$ )] up to  $\sim 2$  GPa, for PVT and polystyrene under shock compression. This indicates, there are no

chemical processes involved for the generation and/or breaking of intra-molecular bonds in present experimental conditions. The  $1602\text{ cm}^{-1}$ ,  $\nu_{8a}$  mode of PVT shifted at an average rate of  $3.94\text{ cm}^{-1}/\text{GPa}$ . This is higher than the shift in the Raman active mode of polystyrene at  $1606\text{ cm}^{-1}$ , which is shifted by an average of  $3.50\text{ cm}^{-1}/\text{GPa}$  over the same pressure range. This indicates that the higher energy modes of PVT are showing relatively higher anharmonicity compared to Polystyrene with increase of pressure. For the final pressure of 2.25 GPa for the present experiment, the bond frequencies of PVT shifted by an amount of 0.6% to 0.8% from the ambient pressure value. Thus the changes in the bond length are of the order of 0.06-0.08% [128]. In contrast, the changes in volume for the corresponding pressure are  $\approx 15\%$ . This clearly indicates that the primarily volume changes (below 1GPa) are due to free volume and compression of the inter-chain bonds, and not because of changes in intermolecular bond lengths. The individual mode Grüneisen Parameters are calculated for each Raman modes. All the observed results shows both aromatic polymers are stable under shock loading and are reversible up to 2 GPa.

## Chapter 5. High pressure and time resolve Raman spectroscopy of polytetra- fluoroethylene (PTFE/Teflon)

### 5.1. Introduction

In this chapter, we report Raman spectroscopic investigation on polytetrafluoroethylene (PTFE) (commonly known by its trade name Teflon), under dynamic shock loading. PTFE is one of the most widely employed fluoropolymer for engineering applications such as aerospace, defense and automotive industries. In addition, PTFE also has potential applications as an energetic material. Dlott and group [129] had studied shock initiation of nano-Al+PTFE macro particles composition and found that this is an extraordinary energetic material which can release energy  $15\text{--}20\text{ kJ/cm}^3$  (2–3 times more than TNT), reacting at 3300K. PTFE is a linear polymer that can be highly crystalline (up to 98%) at low temperatures [130] and mostly famous for its low coefficient of friction. The structure of the PTFE chains gives it unique properties. Unlike polyethylene, PTFE adopts a non-planar structure under ambient conditions. Because of the large size and Vander Waals repulsion between fluorine atoms attached to alternate carbon atoms, a planar conformation has a large amount of steric strain [32]. Consequently, the polymer chains are twisted slightly into a helical conformation in order to relieve some of this strain. This helical polymer chains act like a cylinder with fluorine atoms completely surrounding a carbon backbone. These cylinders are able to slip past each other relatively easily, leading to a low coefficient of friction. In addition, PTFE has a significant amount of creep, i.e., a time-dependent strain in response to a constant stress [131], [132].

PTFE is an exciting polymer for investigating structural changes under extreme conditions, because four solid phases have been reported with static compression below 1GPa [133], [134]. The phase diagram of PTFE is shown in figure 5.1. There are three different phases

that are present near room temperature at atmospheric pressure [32], [33]. Below 19°C, the chains have 13 CF<sub>2</sub> units per 180° twist, in a triclinic phase. Above 19°C, the chains untwist somewhat in a manner that there are 15 CF<sub>2</sub> units per 180° twist. Above 30°C, another phase change occurs where there is conformational disorder in the chains. In addition, there is a high-pressure phase, where the chains untwist into an all-trans configuration. The high pressure phase, phase III is reported to have a monoclinic structure with two molecules per unit cell [135], [136]. PTFE phase III has been reported to be 2% denser than phase II and is quickly reverses on decompression.

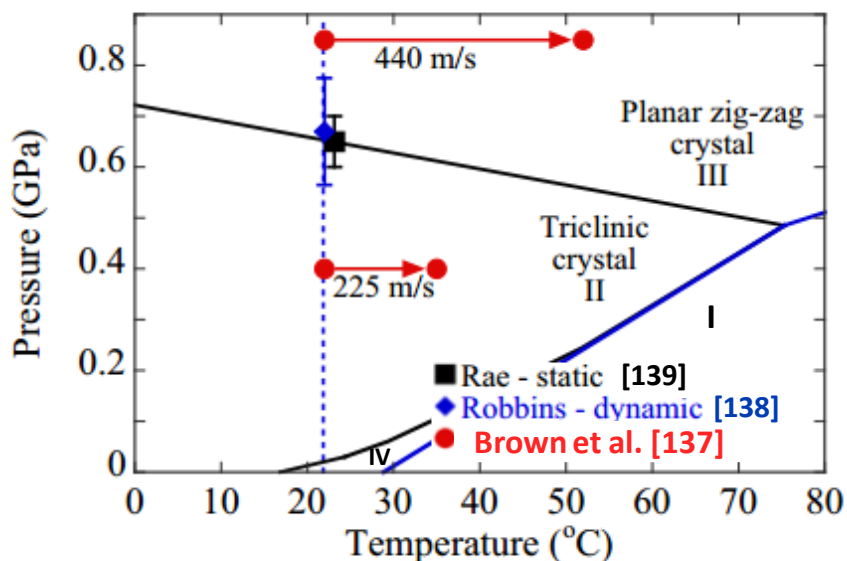


Figure 5. 1. Phase diagram of PTFE. The graph is adopted from Brown et al [137].

The high-pressure phase transition in PTFE was first observed by Bridgman [123] in compressibility measurements and which occurs at approximately 6.5 kbar. Weir [140], and Beecroft and Swenson [141] also performed additional compressibility measurements and observed the high-pressure transition. Flack [142] studied this transition using high-pressure X-ray diffraction of a sample in a DAC, and was able to determine the structure. This phase

change has also been studied using high-pressure infrared and Raman spectroscopy [143]–[145]. Transient Raman spectroscopy has been used as an ultrafast in situ diagnostic of PTFE undergoing shock compression [14], [134]. In the work of Nagao et al. [134] the II–III phase transition was observed to occur on a timescale of  $\sim 10$  ns at 1 GPa. Champion [146], [147] and Robbins and Sheffield [148] studied shock compression of PTFE using techniques like quartz and magnetic particle velocity gauges and electrical resistivity measurements, and found evidence for the high-pressure phase transition  $0.5 \pm 0.2$  GPa with an associated volume change of  $2.2 \pm 0.2\%$ . The work described in this chapter is published by Rastogi et al. in journal of Applied Spectroscopy [149].

## 5.2. Shock Pressure calculation

The peak pressure in Aluminum induced by laser irradiation for glass confinement is calculated by using relation 2.1 [45]. Using the data from SESAME library [27] the principal Hugoniot for Al and Teflon can be written as –

$$\text{For Aluminium} \quad U_s = 5.160 + 1.25u_p \quad (5.1)$$

$$\text{For PTFE/Teflon} \quad U_s = 1.682 + 1.819u_p \quad (5.2)$$

The amount of instantaneous pressures in PTFE as a function of incident laser intensity can be calculated from the Hugoniot of the standard by utilizing the impedance mismatch technique, and is illustrated in figure 5.2 (a). The Hugoniot plots are done by taking the EOS data from SEASME and QEOS. Figure 5.2 (a) shows the plot between pressure and particle velocity for Al and PTFE at a laser intensity of  $2.2 \text{ GW/cm}^2$ . Similar calculations are done for all laser intensities. The calculated pressure values using impedance mismatch technique are compared (figure 5.2 (b)) with average pressure values of 1D hydrodynamic simulation and are found in good agreement for the same laser irradiance.

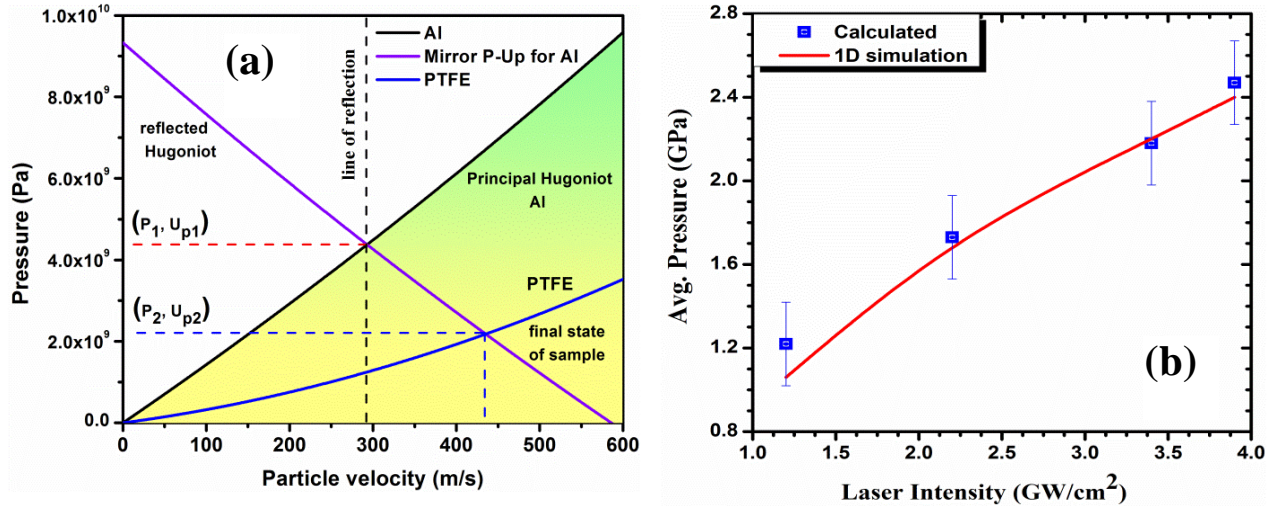


Figure 5. 2. (a) Calculated instantaneous pressure in Al and PTFE behind the shock front using the impedance matching technique with the known sample Hugoniot; (b) shows impedance mismatch and simulation pressure variation with laser intensity.

### 5.3. Results

A typical Raman spectrum of PTFE, under ambient conditions is shown in figure 5.3. The observed fundamental peaks at  $287$  and  $380 \text{ cm}^{-1}$  are assigned to  $\text{CF}_2$  twisting and  $\text{CF}_2$  bending modes respectively. While the strong polarized and sharp fundamental bands at  $729$  and  $1380 \text{ cm}^{-1}$  are assigned to symmetric stretching mode of  $\text{CF}_2$  and C–C respectively. The broad peaks at  $550$  and  $1100 \text{ cm}^{-1}$  are mainly due to glass substrate [136], [150]. Peak at  $1295 \text{ cm}^{-1}$  is also observed and assigned as overtone or combination vibrational mode of PTFE [150].

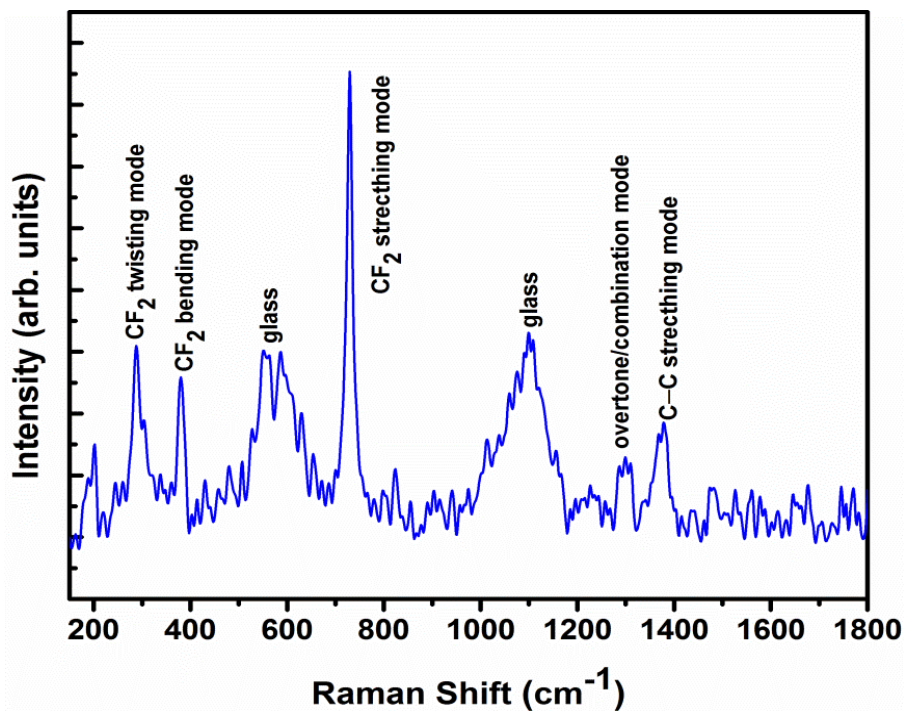


Figure 5. 3. Raman spectra of PTFE at ambient conditions after baseline correction. The broad peaks at 550 and 1100  $\text{cm}^{-1}$  are due to glass substrate.

### 5.3.1. Spectroscopic analysis of PTFE under static compression

The static high pressure Raman measurements are carried out using a triple stage Raman spectrograph (Jobin–Yvon T64000) equipped with a liquid  $\text{N}_2$  cooled open electrode CCD detector. The Raman scattering is excited with 532 nm diode pumped solid state laser and the sample is pressurized using in house developed diamond anvil cell. The sample along with a tiny chip of ruby for pressure calibration is loaded in a hole of  $\sim 100 \mu\text{m}$  diameter drilled in a pre-indented tungsten gasket of thickness  $50 \mu\text{m}$ . No pressure transmitting medium is used here, which make the system less hydrostatic. However sample like PTFE are very soft so the errors in the measured pressure and corresponding peak shift will be very less. Typical relative error in measurements of pressure in hydrostatic environments using our system is about 0.01 GPa. Figure 5.4 shows Raman spectrum of PTFE for the range  $150\text{--}1000 \text{ cm}^{-1}$  under static

compression. Here ambient spectrum is taken for the reference of peak shift. It has been observed from figure 5.4 (a)–(e) that at 1.2 GPa, the CF<sub>2</sub> twisting mode at 287 cm<sup>-1</sup>, shows a red shift of 4 cm<sup>-1</sup> and this red shift start decreasing with pressure. While at higher pressures, the peaks at 380 and 729 cm<sup>-1</sup> show blue shifts.

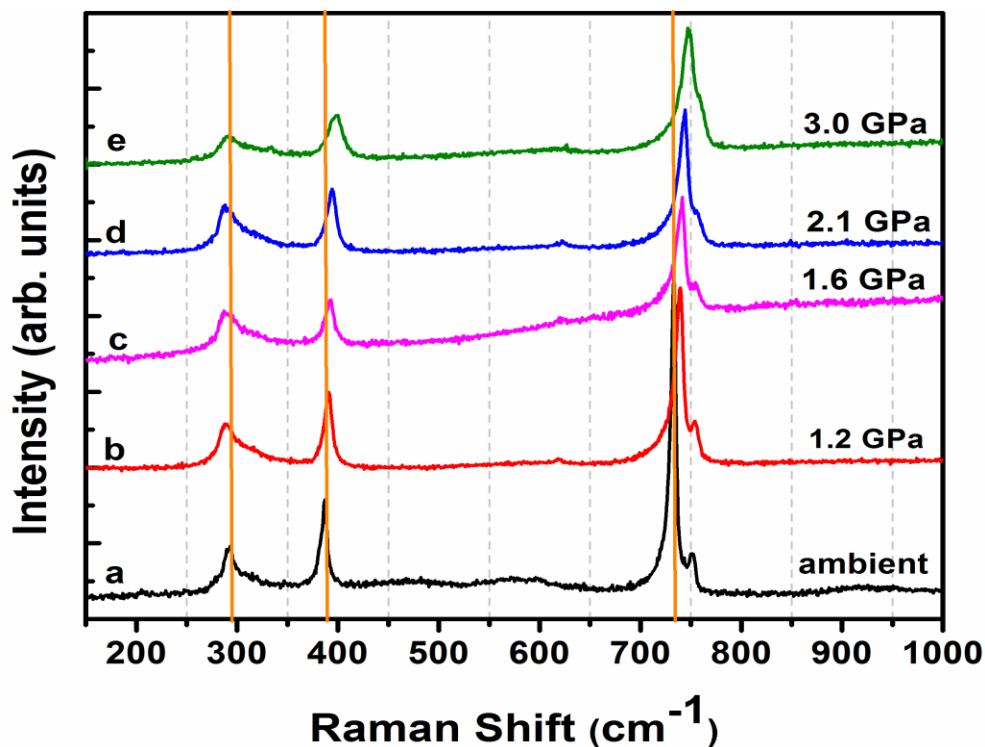


Figure 5. 4. Raman spectra of PTFE at ambient and static high pressure conditions.

The peak shift increases with increasing pressure. It has been reported in earlier publications that PTFE has a high pressure phase (phase III) and shows a pressure induced phase transition (II–III) at 0.72 GPa [136]. Therefore, at present experimental conditions (<1 GPa), the PTFE can be considered in phase III. A shoulder peak is also observed with 729 cm<sup>-1</sup> peak, which also shows some broadening with pressure in each case (figure 5.4). However, the amplitude of this shoulder decreases very sharply with pressure and vanishes at 3 GPa. This suggests that either vibrational mode corresponding to this shoulder is deformed or destroyed.

### 5.3.2. Spectroscopic analysis of PTFE under shock compression

In order to investigate the effect of high dynamic compression on the molecular structure of PTFE, Raman spectra of PTFE at different pressures are recorded. In this study Raman peaks at 287, 380 and 729  $\text{cm}^{-1}$  with respect to the shock pressure is analyzed. The width of the Raman peak increases with the pressure due to contribution of the signal from shocked and unshocked volumes of the sample. The obtained spectra under shock compression are analyzed by fitting double Gaussian peaks, shown as dashed curves in the figure 5.5 for  $\text{CF}_2$  symmetric stretching mode at 729  $\text{cm}^{-1}$ . All of these Raman peaks are blue shifted monotonically and linearly with pressure except for  $\text{CF}_2$  twisting mode at 287  $\text{cm}^{-1}$  (figure 5.6 (a)), which shows a red shift.

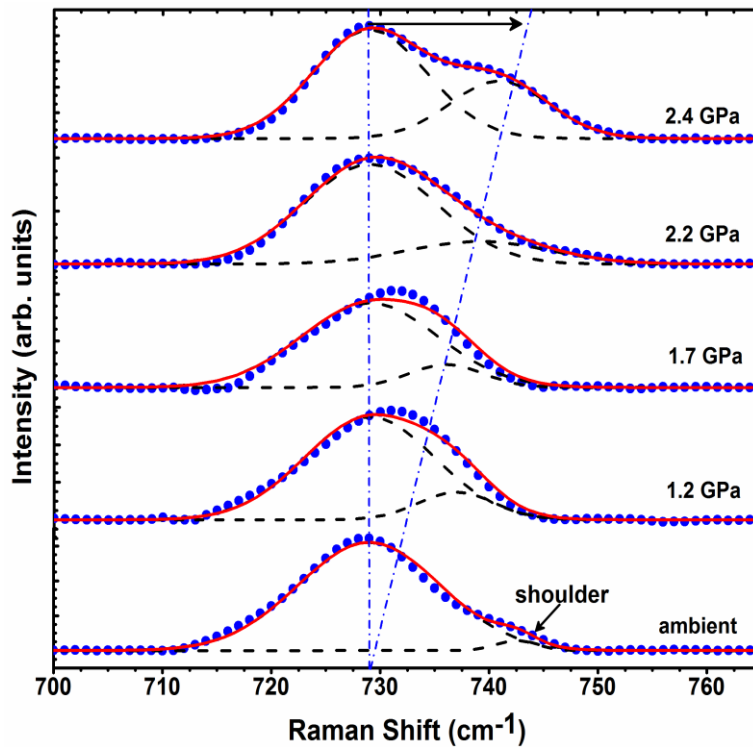


Figure 5. 5. Shows Raman blue shift under dynamic shock compression. The dots in the figure 5.5 are the original experimental data and the dashed lines are the fitted Gaussian

function respectively. The blue dashed line denotes the Raman peak shift under shock compression.

The CF<sub>2</sub> twisting mode first shows decrease in shift for 1.2 GPa and then linearly increases with pressure. This could be a signature of phase transition in PTFE. The fitted results for all observed peaks are shown by the solid lines in figure 5.6 (a). The left Raman peak centered at 729 cm<sup>-1</sup> represents the unshocked region while the right peaks show shocked region. It is observed that a maximum blue shift of 12 cm<sup>-1</sup> taking place for CF<sub>2</sub> symmetric stretching mode under shock compression at 2.4 GPa. The results are compared with pressure induced Raman peak shift under static compression (figure 5.6 (b)). Based on the static compression experimental data, a relationship between pressure induced shift  $\nu$  (cm<sup>-1</sup>) and applied pressure  $P$  (GPa) is established, given as  $\nu = 5.08P$ . According to this relation, the shift 12 cm<sup>-1</sup> corresponds to a pressure of 2.4 GPa inside PTFE, which is in good agreement with pressure values under dynamic compression. Figure 5.6 (b) shows the variation of measured Raman shift of symmetric stretching mode of CF<sub>2</sub> (729 cm<sup>-1</sup>) for the shock (open square) and static compression (fill square) cases. The error bar in the case of shock compression shows the limitation on the time resolution which is approximately 3 ns in this experiment.

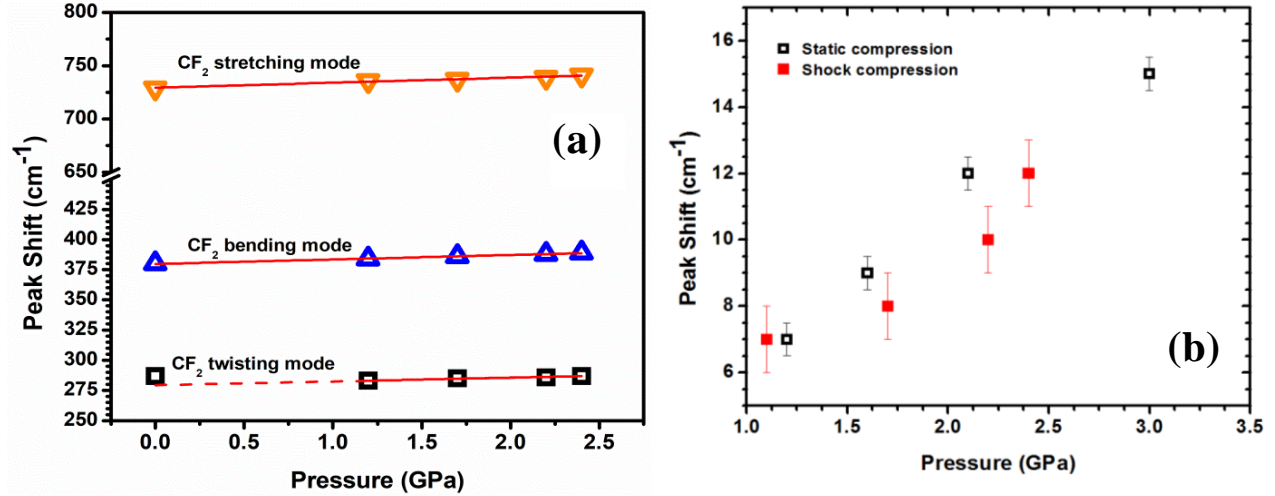


Figure 5. 6. (a) Pressure-dependent behaviors of observed Raman modes of PTFE. The symbols show experimental data, and solid lines show the linear fit to the data (b) Pressure vs peak shift under hydrostatic and shock compression for symmetric stretching mode of CF<sub>2</sub> at 729 cm<sup>-1</sup>. Representative error bars are shown, indicating the estimated uncertainties in the peak shift.

A small deviation in peak shift at lower side for the dynamic compression case may be mainly due to two reasons. First, the noise in the dynamic compression measurements are large as the time taken for the data recording is very small (i.e.,  $300 \times 3$  ns) compared to static compression experiments where data are recorded for several minutes to hour. These fluctuations (noise) constitute the main uncertainty in fitting the shifted peaks. Another reason may be due to the fact that the static compression is isotherm and quasi-hydrostatic. However, the shock compression is Hugoniot which is always lower due to temperature effects.

Along with the frequency shift, the Raman peaks also showed changes in amplitude, total integrated intensity (area under the Raman peak) and the full width half maximum (FWHM) of Raman modes. Figure 5.7 (a) shows the ratios of the amplitude and intensity of the symmetric stretching mode of CF<sub>2</sub> at 729 cm<sup>-1</sup> scattered from the shocked and unshocked region of the targets as a function of applied pressure. It is clear from the figure 5.7 (a) that the amplitude and

total integrated intensity of shifted peak generated under application of pressure increases monotonically. This monotonic increase in total integrated intensity suggests that no bond dissociation or decomposition occurred at the present pressure-temperature conditions of our experiment and time scale considered here, as the bond dissociation would have caused the integrated intensity ratio to decrease. Figure 5.7 (b) shows the effect of shock pressure on full width at half maxima (FWHM). This increase in the FWHM of symmetric stretch mode is mainly caused by increased molecular interactions, which can lead to deformation of molecular structure.

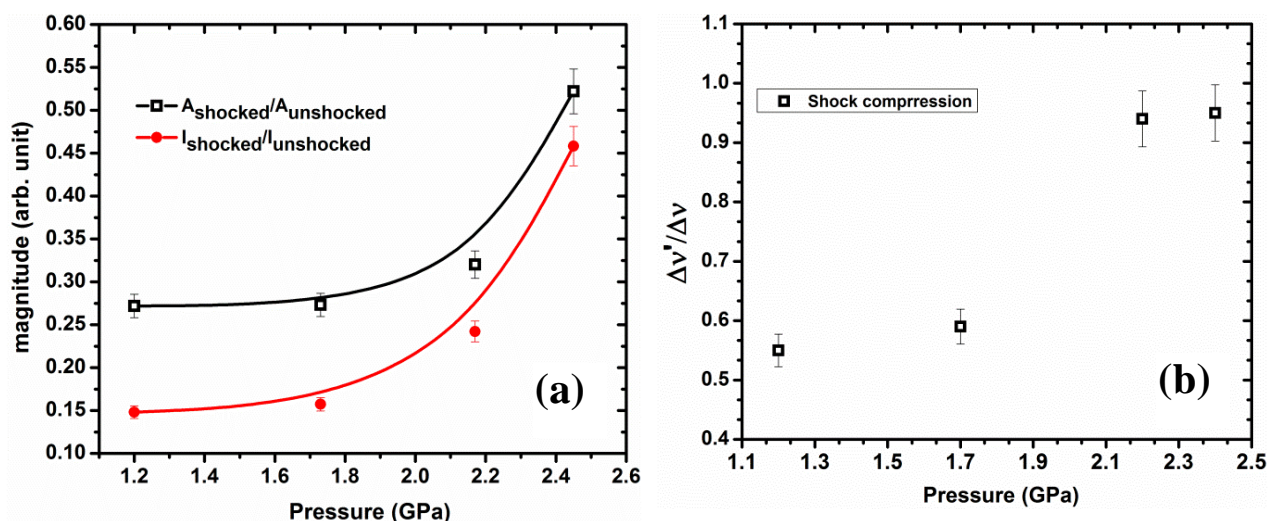


Figure 5. 7. (a) The shocked to unshocked ratios for the  $\text{CF}_2$  symmetric stretching mode; the amplitude and the integrated intensity (area under the Raman peak), (b) the full width at half maximum (FWHM) under shock compression. Representative error bars are shown, indicating the estimated uncertainties in the peak amplitude and FWHM measurement.

### 5.3.3. Time resolved Raman measurement of $\text{CF}_2$ twisting and $\text{CF}_2$ stretching modes under shock compression

Time dependent Raman spectra and decomposition of Raman peaks ( $287$  and  $729\text{ cm}^{-1}$ ) at  $1.7\text{ GPa}$  and at various delay times is shown in figure 5.8 (a) and (b). The simulated results of

shock propagation in PTFE using 1D hydrodynamic code at the same pressure i.e. 1.7 GPa is shown in figure 5.8 (c). The observed Raman peak broadening is mainly because of overlapped Raman peaks of shocked and unshocked regions. Here the time  $t = 0$  ns denote the arrival of pump beam on the aluminum foil surface. At a delay time of  $t = 17$  ns, no change is observed in the Raman peak of the sample. This can also be seen from the simulated results where after 15.8 ns, the shock front just touches the PTFE foil. After a delay time of 31 ns, the shock front is inside the PTFE film but a small portion of PTFE is under shock compression. So the intensity of Raman peak because of unshocked region is much more compared to Raman peak because of shocked region. The intensities of the Raman peaks from the shocked and unshocked volume is almost equal at a delay of 60 ns, means shock has traveled approximately half of the sample thickness. At a delay time of 80 ns, the shock travels more than 90  $\mu\text{m}$  (i.e., 3/4 of the sample thickness) and so the intensity from the unshocked region (i.e., 1/4 of the sample thickness) is much lower than the shocked region. The Raman intensity ratios are dependent on the proportion of the shocked volume verses unshocked volume and the peak positions are dependent on shock pressure. This can also be explained in terms of the shock wave propagation because the whole volume of the sample contributes to Raman scattering. So the observed peak is a superposition of the scattering from both shocked and unshocked volumes. The relative peak intensity variation with delay time is shown in figure 5.9.

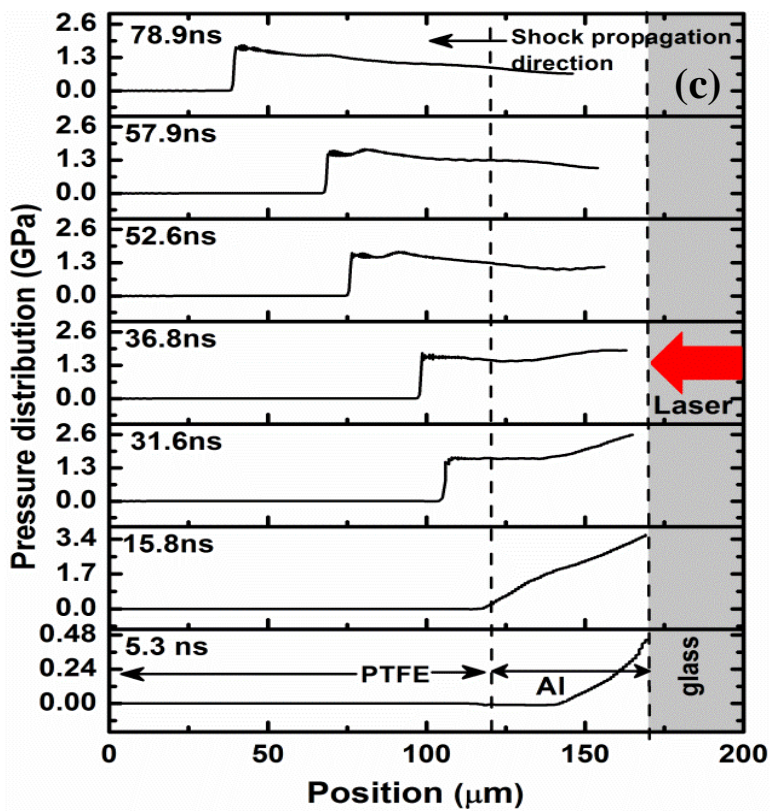
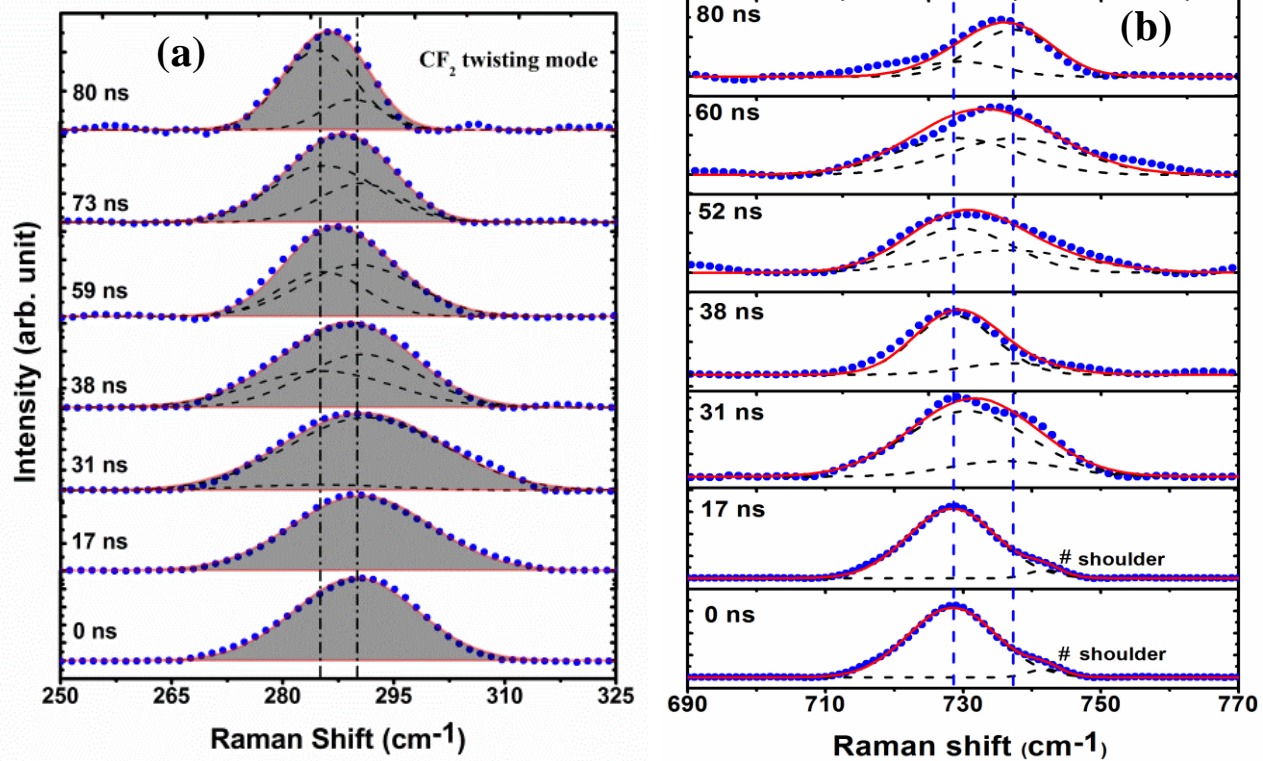


Figure 5. 8. (a) and (b) Time resolved Raman spectra of twisting and symmetric stretching mode of  $\text{CF}_2$ . The time zero denotes the arrival of pump beam at the Aluminum foil. The different times are the time delays between pump and probe pulses. (c) Shock wave profile inside PTFE at different delay times generated by 1D radiation hydrodynamic code MULTI-fs.

#### 5.3.4. Shock velocity calculation inside PTFE using 287 and 729 $\text{cm}^{-1}$ modes

The shock velocity can be estimated by time evolution of the Raman intensity ratios [126], using a relation  $U_s = r \cdot t$ , where  $U_s$  is the shock velocity,  $r$  is the change of the ratios of the signal intensities from the shocked region to total region, and  $t$  is the total thickness of the sample. At delay times, 38, 52, 60 and 80 ns, the Raman intensity ratios belonging to the shocked area for 729  $\text{cm}^{-1}$  are 0.23, 0.72, 1.04, and 2.2 respectively and are shown in figure 5.9. According to the above intensity ratio data, the fitted value of  $r$  is,  $(0.014 \pm 0.001) \times 10^9 \text{ s}^{-1}$ . Hence, the approximate calculated shock velocity inside the PTFE is  $1.68 \pm 0.12 \text{ km/s}$  at a pressure of  $\sim 1.7 \text{ GPa}$ . This is in good agreement with the shock velocity calculated using 1D radiation hydrodynamic simulations. Similar calculations are done for all other fundamental peaks and the calculated shock velocity varies within the  $\pm 5\%$ .

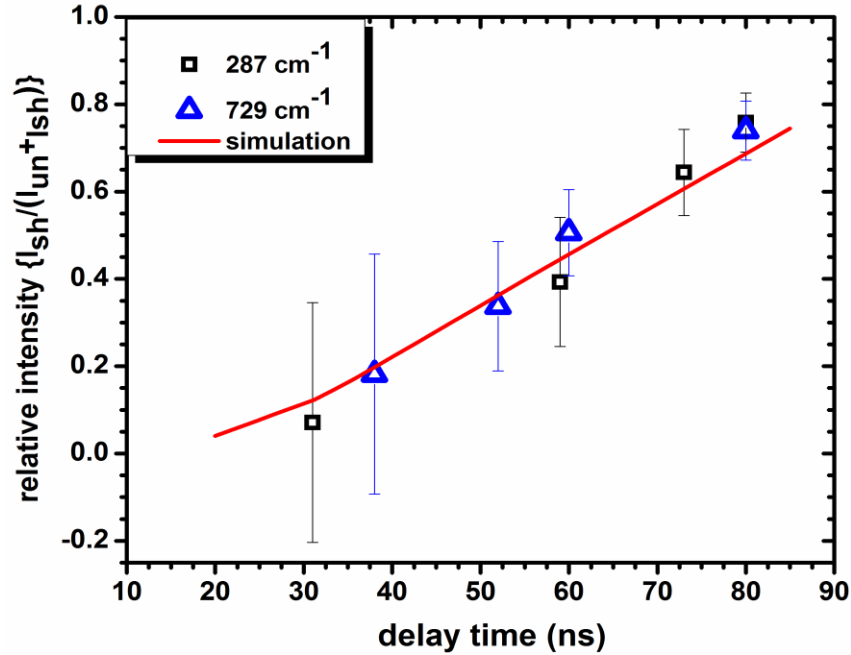


Figure 5. 9. Ratio of the intensities of Raman peaks from the shocked and the total region for the peak 287 and 729  $\text{cm}^{-1}$  verses delay time. Representative error bars indicate the estimated uncertainties in the calculated relative amplitudes.

#### 5.4. Discussion

The behavior of polymers under high pressure, especially under shock compression is of fundamental interest and received attention in several studies [25], [26], [147], [151]–[153]. There have been several different studies of polytetrafluoroethylene under high pressure. Wu et al. [143] had reported the pressure induced shift for symmetric stretching mode of  $\text{CF}_2$  at 729  $\text{cm}^{-1}$  in their hydrostatic compression experiments. They proposed a relation between pressure induced shift ( $\nu \text{ cm}^{-1}$ ) and the pressure ( $P \text{ GPa}$ ) with a well fitted linear equation by  $\nu = 6.97P + 1.93$ . Using this linear equation, Nakamura et al. [23] estimated the pressure for their nanosecond time resolved Raman spectroscopy of PTFE under laser driven shock compression. They found an 18  $\text{cm}^{-1}$  peak shift of symmetric stretching mode of  $\text{CF}_2$  at 729  $\text{cm}^{-1}$ . For present

shift of  $18\text{ cm}^{-1}$  they estimated a pressure of 2.3 GPa for laser intensity of  $4.0\text{ GW/cm}^2$ , which they found is comparable with the ablation pressure calculated by using impedance mismatch technique. In contrast Wu et al. [136] results for symmetric stretching mode of  $\text{CF}_2$  at  $729\text{ cm}^{-1}$ , our static compression results shows a peak shift of  $12\text{ cm}^{-1}$ , with a fitted linear equation between pressure induced peak shifts and the pressure:  $\nu = 5.08P$ . According to this linear equation obtained from static compression experiment peak shift of symmetric stretching mode of  $\text{CF}_2$  corresponds to a shock pressure of 2.4 GPa for our laser driven shock results. This is in good agreement with the pressure value calculated from hydrodynamic simulations within experimental errors.

In other study, Wakabayashi et al. found a new vibrational peak at  $1895\text{ cm}^{-1}$  at about 2.3 GP under laser driven shock compression using time resolved Raman spectroscopy and observed the intensity of this new peak increases gradually with delay time. They attributed this new peak as symmetric stretching mode of a  $\text{C}_2\text{F}_4$  monomer produced by depolymerization under shock compression. For this experiment they used a confinement geometry target assembly which consist a backup glass ( $100\times 100\times 5\text{ mm}^3$ ), an aluminum foil ( $25\text{ }\mu\text{m}$  thick), a PTFE film ( $80\text{ }\mu\text{m}$  thick) and a cover glass ( $2\text{ mm}$  thick). In contrast to their results we have not observed any new peak under laser driven shock compression up to 2.4 GPa using the confinement geometry target assembly with  $50\text{ }\mu\text{m}$  thick aluminum foil. In their work Nakamura et al. has performed nanosecond time resolved Raman spectroscopy on PTFE under laser shock compression at laser power density  $4\text{ GW/cm}^2$ . They observed that the most intense vibrational peak of PTFE, the symmetric stretching mode at  $729\text{ cm}^{-1}$  showed a higher shift of  $18\text{ cm}^{-1}$  at delay time of 9.3 ns because of shock compression. They compare their result with hydrostatic compression result of Wu and Nicol et al. [136] and estimate approximate shock pressure in PTFE as 2.3 GPa, which

matched with their calculated value using impedance matching technique. They also reported a new vibrational line at  $1900\text{ cm}^{-1}$  under shock compression and assigned this as C=C stretching in transient species such as  $\text{C}_2\text{F}_4$  monomer produced by shock induced bond scission. They found that the intensity of the new line increases with increasing delay time along propagation of shock compression. In order to assign this new peak they have performed ab-initio calculations. They calculated the frequency after the full geometry optimization. From the calculated frequencies they guessed the Raman line at  $1900\text{ cm}^{-1}$  is due to the  $\text{C}_2\text{F}_4$  monomer transiently generated by shock induced bond scission. Wakabayashi et al., [15] have measured time resolved Raman spectroscopy of PTFE and reported formation of a new vibrational line at  $1895\text{ cm}^{-1}$  under shock compression, which they attributed to the symmetric stretching mode of a  $\text{C}_2\text{F}_4$  monomer produced by depolymerization, appears under the shock compression, and its intensity increases with time. Appearance of the vibrational line at  $1895\text{ cm}^{-1}$  starts at 5.3 ns after the pump beam irradiation.

Nagao et al., have reported nanosecond time resolved Raman spectroscopy of laser shocked PTFE under 1GPa shock compression. They observed a blue shift of  $8\text{ cm}^{-1}$  in the C–C stretching mode and a red shift of  $8\text{ cm}^{-1}$  in  $\text{CF}_2$  twisting mode because of high pressure phase of PTFE. They suggest that the high pressure phase transition to phase III of PTFE occurred within 10 ns. In this paper they also reported that they are using 50 micron thick Aluminum foil in order to avoid direct laser irradiation on the PTFE. When they used 50 micron Al foil in confinement target assembly, no new peak was observed but when they use 25 micron Al foil a through hole formed and a new peak at around  $1900\text{ cm}^{-1}$  was observed. In our experiments we also observed the same results for C–C stretching and  $\text{CF}_2$  twisting modes of PTFE with a time resolution of 7 ns. The high pressure phase transitions are also verified by the static compression experiments.

All the results are found in good agreement. Like our experiments Nagao et al. also do not observed or reported any new peak in PTFE by using 50 micron thick Aluminum foil in the target assembly. So it is unclear that this new peak occurred only due to depolarization of PTFE under shock compression. This might be because of decomposition of PTFE film due direct laser irradiation. To validate these results, a 1D hydrodynamic simulation is performed. From the simulation results it is observed that the shock build up time is about 11 ns and once it build up, it takes around 4.8 ns to cross 25  $\mu\text{m}$  thickness (i.e. total time 15.8 ns) and 9 ns to cross 50  $\mu\text{m}$  (i.e., total 20 ns). Hence, it is unlikely to get shock wave in the PTFE sample and formation of a new peak under shock loading after 5.3 ns pump beam irradiation like the case in Wakabayashi et al. [15].

## 5.5. Conclusions

The time resolved Raman spectroscopy is used to observe the pressure induced molecular and physical changes on nanosecond time scale. Raman spectra are measured as a function of shock pressure in the 1.2–2.5 GPa range. A signature of possible phase transition for PTFE below 1.2 GPa has been observed. Furthermore, the vibrational mode at  $729\text{ cm}^{-1}$ , attributed to symmetric stretching mode of  $\text{CF}_2$  is compared to corresponding static high pressure measurements carried in a diamond anvil cell. Observed changes in  $729\text{ cm}^{-1}$ , Raman spectra line width (FWHM) indicates that the shock pressure gradient is responsible for Raman peak broadening rather than shock induced temperature in PTFE film. A relationship between pressure induced shift ( $\nu\text{ cm}^{-1}$ ) and applied pressure ( $P\text{ GPa}$ ) for static compression is given by the linear equation  $\nu = 5.08P$ . According to this relation, the shift  $12\text{ cm}^{-1}$ ; corresponds to a pressure of 2.4 GPa inside PTFE, which is in good agreement with pressure values under dynamic compression. By using time evolution of Raman intensity ratios, the shock velocity is estimated

to be  $1.68 \pm 0.12$  km/s. This is in good agreement with the calculated shock velocity using 1D radiation hydrodynamic simulations.

## Chapter 6. Raman Spectroscopy of Poly (Methyl Methacrylate) under laser shock compression

### 6.1. Introduction

In this chapter, we report our Raman spectroscopic investigation on thermoplastic polymer, poly (methyl methacrylate) (PMMA) under shock compression. PMMA is a thermoplastic acrylic polymer made from methyl methacrylate monomers and commonly known as Plexi glass or Lucite. This polymer is a widely used material and valued for the high degree of transparency in the atactic amorphous form. PMMA is probably the most studied polymeric material in shock compression experiments. Its purpose in these experiments is to maintain a high pressure on the surface of an adjacent sample of interest, while still allowing optical probes to penetrate to the surface [154]. In particular, PMMA has been used as a backing window material in shock compression experiments. The most common of these optical probes is VISAR (Velocity Interferometry System for Any Reflector). In addition, experimental studies of shock compression and laser ablation of PMMA have revealed important information in such areas as ablation induced chemistry [155], [156].

In this chapter, the effect of shock induced physical changes in the fundamental modes of PMMA under shock compression is examined. The individual mode Grüneisen parameters are also calculated under the assumption that they are volume independent. The experiments are performed on confined geometry target assembly by pump and probe technique using high power pulsed laser. The target assembly consists of a cover glass ( $100 \times 100 \times 5 \text{ mm}^3$ ), an Al foil ( $50 \mu\text{m}$  thick), a PMMA film sheet ( $200 \mu\text{m}$  thick), and a back-up glass ( $100 \times 100 \times 5 \text{ mm}^3$ ). The fundamental laser pulse having power density  $\sim 10^9 \text{ W/cm}^2$ , is focused on the Al foil with a spot diameter of 2 mm to generate shock wave in Al, and the second harmonic radiation

(~4mJ/pulse) with a focused diameter of 500  $\mu\text{m}$  on the rear side of the sample. The PMMA is purchased as sheet with thickness and size of 200  $\mu\text{m}$  and 100 $\times$ 100  $\text{mm}^2$  respectively.

## 6.2. Previous studies on PMMA under static and shock compression

There have been several studies are performed on PMMA under high pressures, both static and dynamic compressions. Flores and Chronister [157] investigated PMMA in a DAC at pressures up to 3.5 GPa using Raman spectroscopy. They measured the pressure-induced frequency shift of two fundamental modes and used the EOS data of Bridgman [156] to obtain individual mode Grüneisen parameters. They used different models to determine the volume dependency of the mode Grüneisen parameters. These measurements are used in several shock compression experiments, where ultrafast in-situ Raman spectroscopy was used to study PMMA [151]–[153]. In one study, Hare et al. [153] used coherent anti-Stokes Raman spectroscopy (CARS), to measure time-resolved spectrum of PMMA with 2 ns resolution. The laser ablation was also studied [151], [152], and decomposition of PMMA with monomer formation is observed due to rapid pressure and temperature increase. In their other study, Hare et al. [151] performed picoseconds (ps) CARS to study the dynamics of PMMA and measure dynamic frequency shifts compressed by a laser driven shock wave. Emmons et al. [158] performed high-pressure infrared absorption spectroscopy of PMMA using diamond anvil cell up to 8 GPa. They analyzed all fundamental vibrational modes of PMMA using both volume independent and dependent Grüneisen parameters models. They found that the observed vibrational frequency shifts as a function of pressure in PMMA are consistent with similar types of bonds in other molecules.

Relevant to the discussion of free volume in PMMA, Skorodumov and Godovskii [159] studied the dependence of glass transition temperature on pressure up to 0.7 GPa, having an

ambient glass transition temperature of  $\sim 378$  K. At pressures below 0.5 GPa, it was found that the glass transition temperature start increasing with a rate of  $\sim 20$  K/kbar and above 0.5 GPa, the glass transition temperature asymptotically leveled off to  $\sim 485$  K. Skorodumov and Godovskii observation was found in agreement with the Gibbs–Dimarzio theory of glass transition temperature dependence on pressure and in disagreement with the free volume theory [36], [131].

### 6.3. Shock pressure determination

The peak pressure in Al foil induced by laser irradiation for glass confinement is calculated by using equation 2.1 [45]. The instantaneous pressure in PMMA as a function of incident laser intensity is calculated by utilizing the impedance matching technique [134]. The parameters used for pressure calculation are given in table 6.1 and plotted Hugoniot at  $3.98$   $\text{GW}/\text{cm}^2$ , is shown in figure 6.1 (a). Similar calculations are done for all other laser intensities. The estimated pressure values calculated here using impedance mismatch technique are compared with the average pressure values of 1D hydrodynamic simulations for the same laser intensity. The results are shown in figure 6.1 (b) and are found in good agreement with each other.

**Table 6. 1.** Parameters used for Hugoniot and shock pressure calculations, where  $C_0$  (sound velocity in the bulk) and  $S$  (shock parameter) are materials specific parameters [27]

Material	Density $\rho_0$ ( $\text{gcm}^{-3}$ )	$C_0$ ( $\text{kms}^{-1}$ )	$S$
Al- foil	2.70	5.160	1.25
PMMA	1.18	2.260	1.82

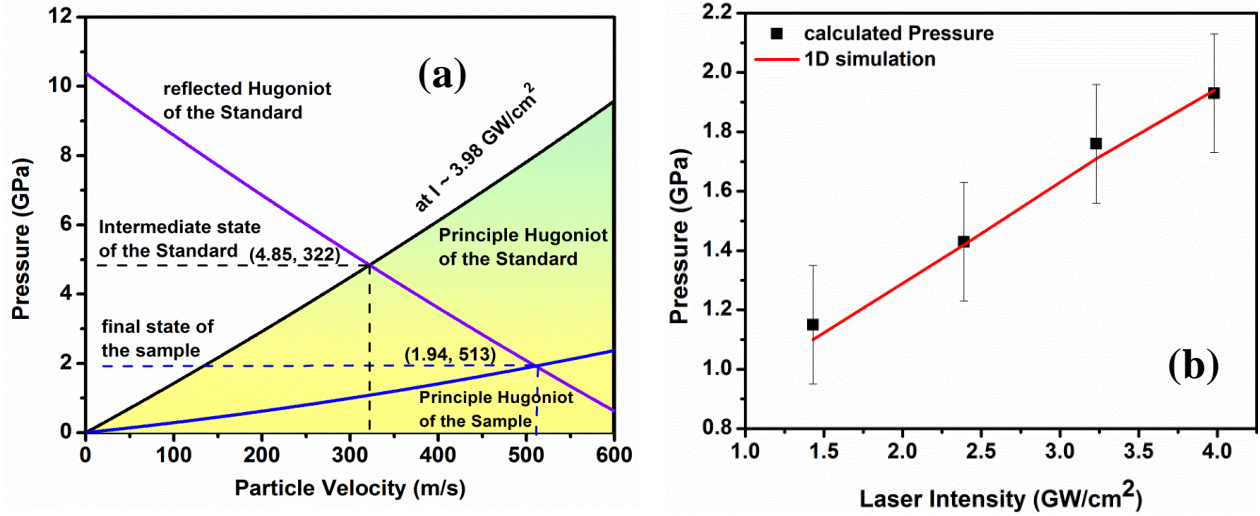


Figure 6. 1. (a) shock pressure calculation in Al and PMMA using principle Hugoniot data and impedance mismatch technique (b) represents variation of pressure with laser intensity.

#### 6.4. Shock velocity calculation in PMMA

The time dependent Raman spectra of  $\nu_s(\text{C-O-C})$  mode at  $813 \text{ cm}^{-1}$  of PMMA at various delay times for a fixed pressure of 1.94 GPa, is shown in figure 6.2 (a). It can be seen from the figure 6.2 (a) that the  $\nu_s(\text{C-O-C})$  mode at  $813 \text{ cm}^{-1}$  of PMMA show an increase in intensity in shock induced Raman peak with increase in delay time, as shock get longer time and hence longer duration to propagate in the sample. The left centered peak at  $813 \text{ cm}^{-1}$  represents the unshocked volume while peak at  $820.7 \text{ cm}^{-1}$  represents shocked volume. The observed peak is a superposition of the Raman peaks from both shocked and unshocked volumes. This volume proportionality of Raman intensity on shocked and unshocked regions are compared with the shock wave propagation in the sample using 1D radiation hydrodynamic code, shown in the figure 6.2 (b). From figure 6.2 (b) one can observe that at a delay time 20 ns, the shock front is about to reach the Al-PMMA interface. After a delay time of  $\sim 24$  ns, the shock front enters in the PMMA sheet but a small portion of PMMA is under shock compression. Therefore, in broadened Raman peak only a small contribution of shocked volume is seen and most of the

peak intensity is because of unshocked volume. This can be seen from figure 6.2 (a). At 50 ns, the shock travels around half of the sample. So, the intensity due to shocked volume is comparable to the unshocked volume. At delay time of 66 ns, it can be seen that the signal from shocked volume is much more than the signal from unshocked volume. Same can be seen from the simulation results at 70 ns delay that the shock has reached almost up to the end of the sample and it completely passes the sample after 70 ns time delay. In the experimental data shown in figure 6.2 (a) for delay 80 ns, the intensities of shocked volume is decreasing while from unshocked volume is increasing. This indicates that the behavior of the mode at  $813\text{ cm}^{-1}$  is reversible up to 1.94 GPa.

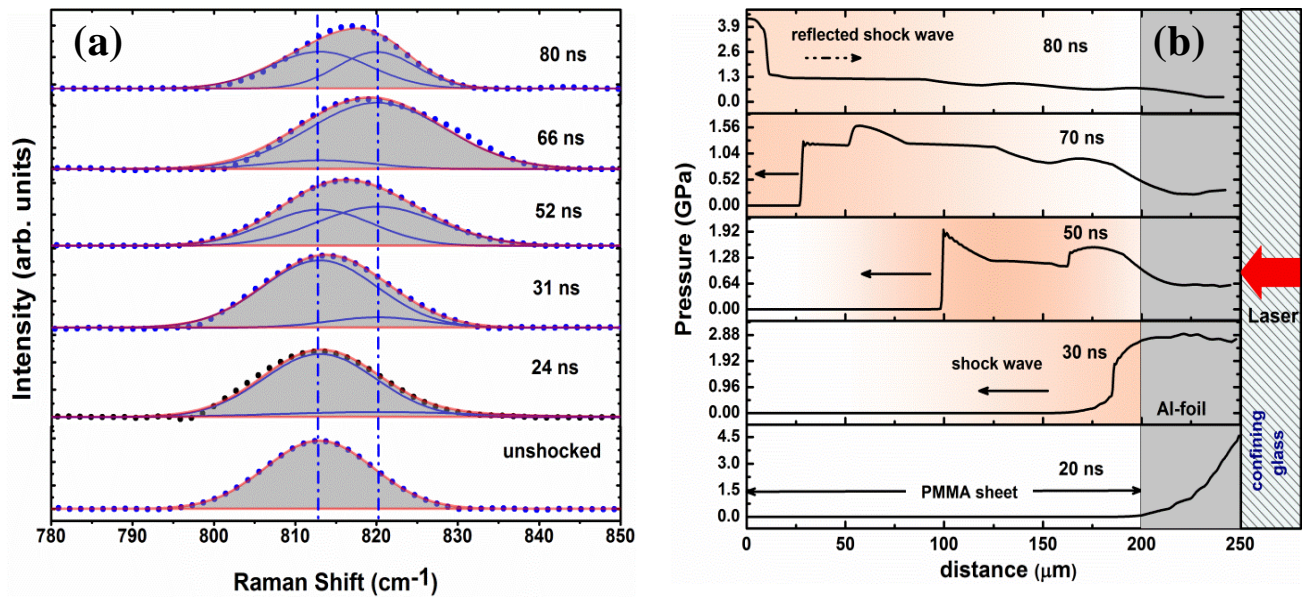


Figure 6. 2. (a) Show time resolved Raman spectra of  $813\text{ cm}^{-1}$  mode at various delay times. The vertical dashed blue lines denote the Raman peak location at ambient and under shock compression (b) Shock wave propagation inside PMMA at different delay times. The simulations are done by using 1D radiation hydrodynamic code.

The shock velocity inside PMMA can be calculated by plotting the ratio of shocked signal to the total signal with respect to delay time. At delay times of 24, 31, 52 and 66 ns, the

Raman intensity ratio belonging to the shocked volume are 0.12, 0.13, 0.55 and 0.91 respectively. By using relation [127], [160]:  $U_s = r \cdot t$ ; the calculated shock wave velocity is  $3.8 \pm 0.40$  km/s. This is found in good agreement with the shock velocity deduced from the hydrodynamic simulation within experimental error.

### 6.5. Raman Spectrum of PMMA under ambient conditions

Figure 6.3 shows the monomeric structure of PMMA. PMMA is a vinylidene type polymer. The most commonly used type of PMMA for technical applications is atactic and consequently completely amorphous. The  $\text{CH}_2$  group is termed as methylene group, while the  $\text{CH}_3$  groups attached to carbon backbone and the singly bonded oxygen atom are denoted as  $\alpha$ -methyl and ester methyl, respectively [158]. The  $\text{C}=\text{O}$  group attached with carbon backbone is a carbonyl group. The bulky side groups make crystallization of the atactic form prohibitively difficult. However, the stereoregular PMMA can be crystallized and synthesized [161]. Also, conventionally prepared PMMA tends to have a tendency towards syndiotacticity [161], [162]. Because of complete lack of symmetry in amorphous PMMA, all the normal modes are allowed in both the infrared and Raman spectra. However, typically a mode is stronger in one type of spectrum than the other. Instead of taking a group theoretical approach, the concept of characteristic group frequencies is used to analyze the spectra. This is based on the idea that the same types of bonds in different molecules will have similar electronic structures, and consequently, similar vibrational frequencies [158]. The adjacent bonds will only have a perturbing effect on the electronic structure and vibrational frequency of these bonds. In general, one would expect that since a vibrational normal mode of a molecule must be considered as a vibration of the molecule as a whole, the normal mode frequencies should vary significantly from those of an isolated bond. However, when either the frequencies of two isolated bonds are

very different, or the masses of the particles involved vary significantly, a vibration can be considered as isolated to a certain piece of a molecule [163].

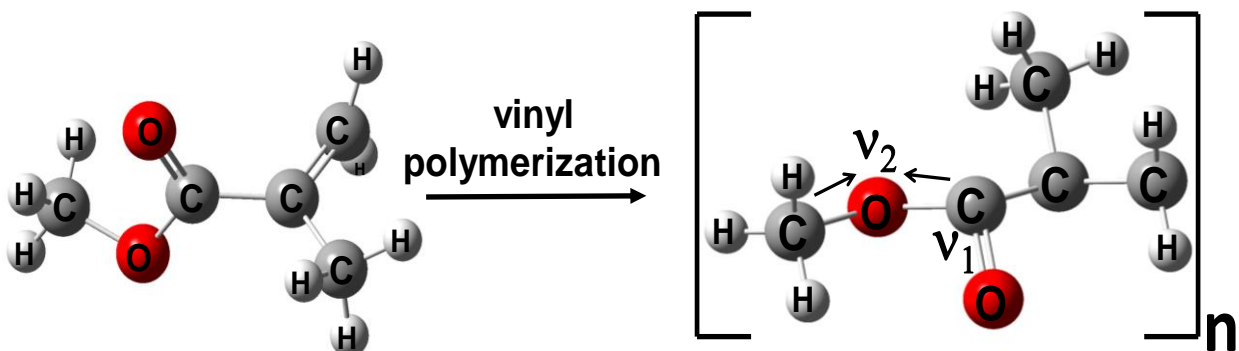


Figure 6. 3. (a) Molecular structure of Methyl methacrylate (b) PMMA repeating monomer unit. The labeled mode  $\nu_1$  represents the (C–C–O) stretching mode and  $\nu_2$  represents symmetric/anti-symmetric stretching modes of (C–O–C) respectively.

The Raman spectrum of PMMA for the range  $200\text{--}3300\text{ cm}^{-1}$  at ambient conditions is shown in figure 6.4. Several Raman active modes are observed and list of mode frequencies with their descriptions are given in table 6.2. However, some of the modes are found very weak in the Raman spectrum. For PMMA,  $\nu_1$  and  $\nu_2$  corresponds to the C–C–O symmetric stretching mode at  $599\text{ cm}^{-1}$  and C–O–CH<sub>3</sub> stretching mode at  $813\text{ cm}^{-1}$ , and fundamental mode at  $1728\text{ cm}^{-1}$  is assigned as carbonyl (C=O) stretching vibrational mode respectively [164]. The observed peaks at  $1453$  and  $2957\text{ cm}^{-1}$  are assigned to bending and stretching modes of C–H respectively. The Raman peaks at  $1125$ ,  $1161$  and  $1188\text{ cm}^{-1}$  due to C–C skeleton mode and  $\nu_a(\text{C–O–C})$  are mixed with the broad peak observed at  $1100\text{ cm}^{-1}$  (mainly due to glass substrate) and cannot be resolved [134].

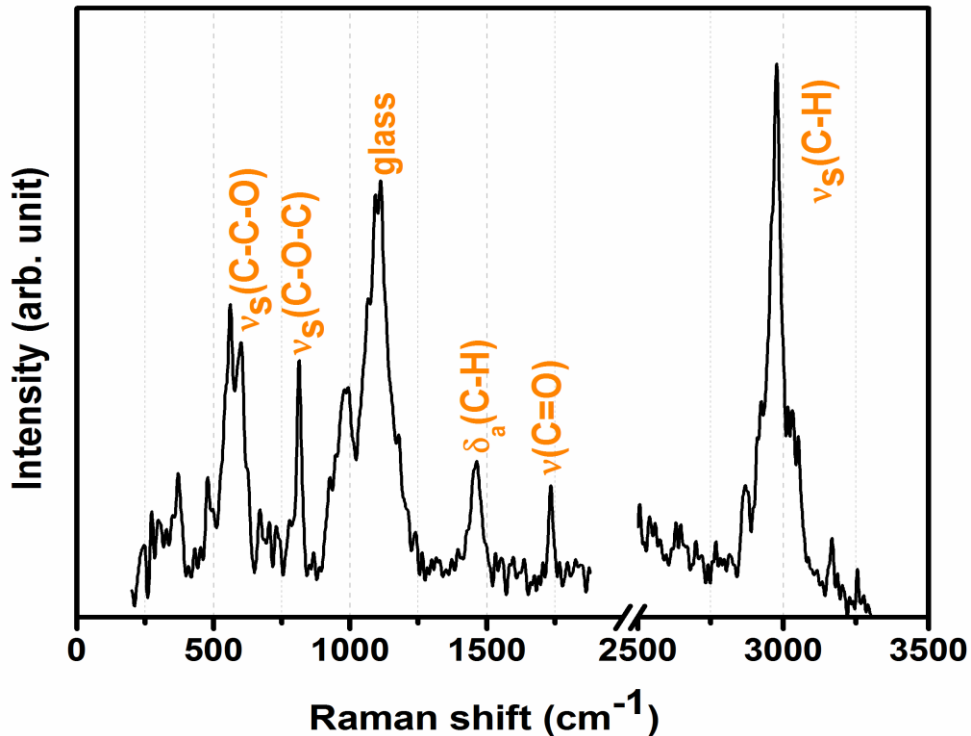


Figure 6. 4. Normalized Raman spectrum of PMMA for the range 200–3300  $\text{cm}^{-1}$ , using 532 nm excitation.

## 6.6. Results and Discussion

### 6.6.1. Raman measurement of PMMA under shock compression

The Raman spectrum of PMMA for the range 200–3300  $\text{cm}^{-1}$  as a function of pressure is shown in figure 6.5. The mode assignment for band frequencies are taken from Willis et al. [165]. All of the vibrational modes are showing pressure induced broadening and are shifted to higher wavenumber (blue shift) with the pressure. All these changes are found reversible up to  $\sim 2$  GPa. The decrease in Raman intensity of vibrational modes with pressure depends on the strength of polarizability of molecule for those modes. The polarizability changes specific to the chosen vibrational mode as a function of pressure. By increasing the pressure the polarizability of the specific mode decreases. However, for the better visibility of the signals

broadening and shift in the graph (because of low signal), all shocked and unshocked signal are normalized and is shown in figure 6.5.

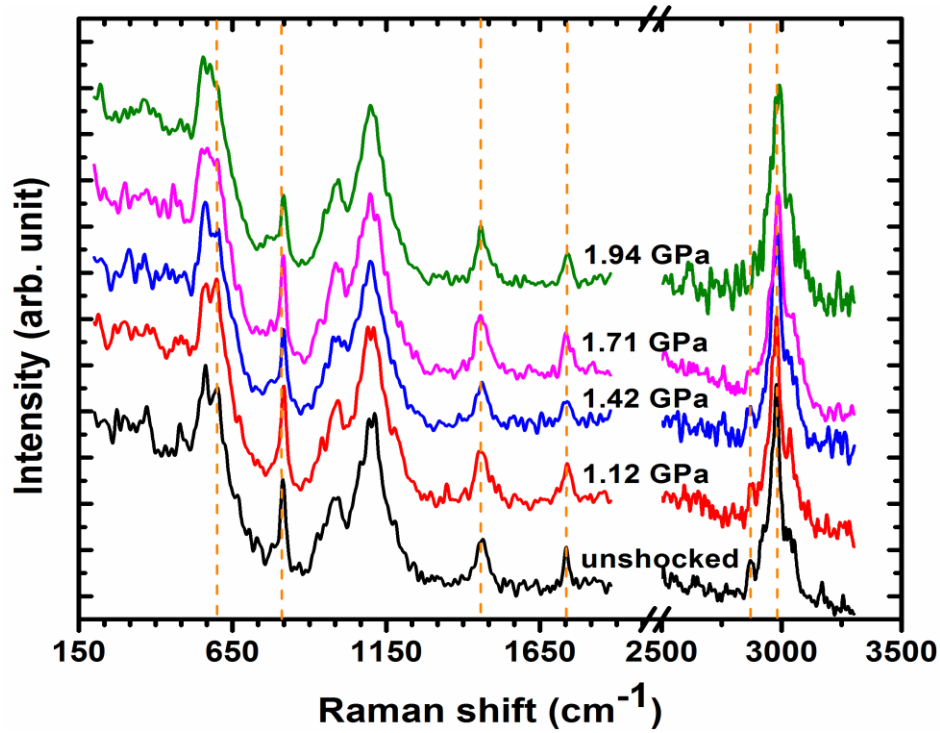


Figure 6. 5. Normalized, spontaneous Raman spectrum of PMMA as a function of shock compression for the range 200- 3300  $\text{cm}^{-1}$ .

**Table 6. 2.** Raman active modes under ambient conditions

Wilis frequency ( $\text{cm}^{-1}$ ) and their polarization		Current frequency ( $\text{cm}^{-1}$ )	Mode Assignment
487m	dp	484	out of plane deformation
604s	p	599 <sup>a</sup>	$\nu_s(\text{C}-\text{C}-\text{O})$
818vs	sp	813 <sup>a</sup>	$\nu_s(\text{C}-\text{O}-\text{C})$
833vw	?	857	$\text{CH}_2$ rock
970 ms	dp	972	$\alpha-\text{CH}_3$ rock
991ms	p	986	$\text{O}-\text{CH}_3$ rock
1125mw	?	-	$\nu(\text{C}-\text{C})$ skeletal mode

1161w	?	-	$v_a(\text{C-O-C})$
1188mw	?	-	
1456 ms	dp	1453	$\delta_a(\text{C-H})$ of $\alpha$ -CH <sub>3</sub> $\delta_a(\text{C-H})$ of O-CH <sub>3</sub>
1490w	?	1494	$\delta(\text{CH}_2)$
1736mw	p	1728	carbonyl $\nu(\text{C=O})$
2849vw	?	2846	combination band involving O-CH <sub>3</sub>
2957m	?	2957	$\nu_s(\text{C-H})$ Of O-CH <sub>3</sub> with $\nu_s(\text{C-H})$ of $\alpha$ -CH <sub>3</sub> and $\nu_a(\text{CH}_2)$

Abbreviations: vs = very strong; s = strong; m = medium; w = weak; ms = medium strong; vw = very weak; sh = shoulder; p = polarized; dp = depolarized; sp = strongly polarized; ? = polarization doubtful.

<sup>a</sup>The two Raman active modes previously measured and discussed by Flores and Chronister [166].

The peak position of the amorphous PMMA for several characteristic peaks in order to get a further insight into the pressure dependence of each Raman peak are plotted against pressure in figure 6.6 (a) and (b). The weak Raman modes in present case are difficult to identify and are smeared out as the pressure increases. So the peak position cannot be identified correctly and hence are not shown in the figure 6.6 (a) and (b). The Raman shift increases proportionally with the pressure and the position are fit by linear least square method to obtain information about sensitivity of particular Raman modes on pressure.

### 6.6.2. Bond associated with C–CO–O–CH<sub>3</sub> group

The effect of shock loading on 813 cm<sup>-1</sup>, assigned as symmetric stretching vibrations of C–O–C is shown in figure 6.6. The details of the peak fitting are given in the figure 6.6. The symmetric stretching mode  $\nu_s(\text{C–O–C})$  at 813 cm<sup>-1</sup> shifted at an average of 2.65 cm<sup>-1</sup>/GPa between 1.12–1.94 GPa. Similarly, the peak fitting for other modes are also done. It is observed that the mode  $\nu_s(\text{C–C–O})$  at 599 cm<sup>-1</sup> shifted by an average of 3.09 cm<sup>-1</sup>/GPa. The larger shift for C–C–O mode indicates the greater anharmonicity in the potential energy surface of this mode or the local volume compression near this coordinate is larger than for the C–O–C mode. Since the C–O–C mode is more extended from the polymer backbone relative to C–C–O mode, this suggest that the smaller shift is due to smaller intrinsic anharmonicity for this vibrational mode [166]. The frequency shift of these stretching modes of PMMA can be compared with similar modes examined by Schoonover et al. [167] PMMA can be most directly compared to a homopolymer which contains only the ester segments, poly (butylene adipate). The three ester  $\nu(\text{C–O–C})$  vibrations are examined. These  $\nu(\text{C–O–C})$  vibrations showed pressure shifts covering the range of 1–6 cm<sup>-1</sup>/GPa, somewhat larger than those observed in PMMA. The other vibrational mode,  $\nu(\text{C=O})$  carbonyl stretching mode at 1728 cm<sup>-1</sup>, shifts by an average of 2.0 cm<sup>-1</sup>/GPa between 1.12–1.94 GPa. Schoonover et al. [167] had measured an average shift of 2 cm<sup>-1</sup>/GPa for the same mode in Estane and poly (butylene adipate). A larger vibrational shift of 3 cm<sup>-1</sup>/GPa was measured for a hydrolytically degraded Estane. The shift of this  $\nu(\text{C=O})$  mode in PMMA can also be compared with the C=O vibration in polycarbonate [16], which show shift by a value of 2.1 cm<sup>-1</sup>/GPa. The comparison between the shifts of this  $\nu(\text{C=O})$  group for three diverse types of polymers suggest that the pressure induced shifts of groups may be relatively dependent on the exact nature of the sample. This relative dependence

in case of PMMA may be because of strong intermolecular hydrogen bonding of the C=O group have effect on the pressure shift [167].

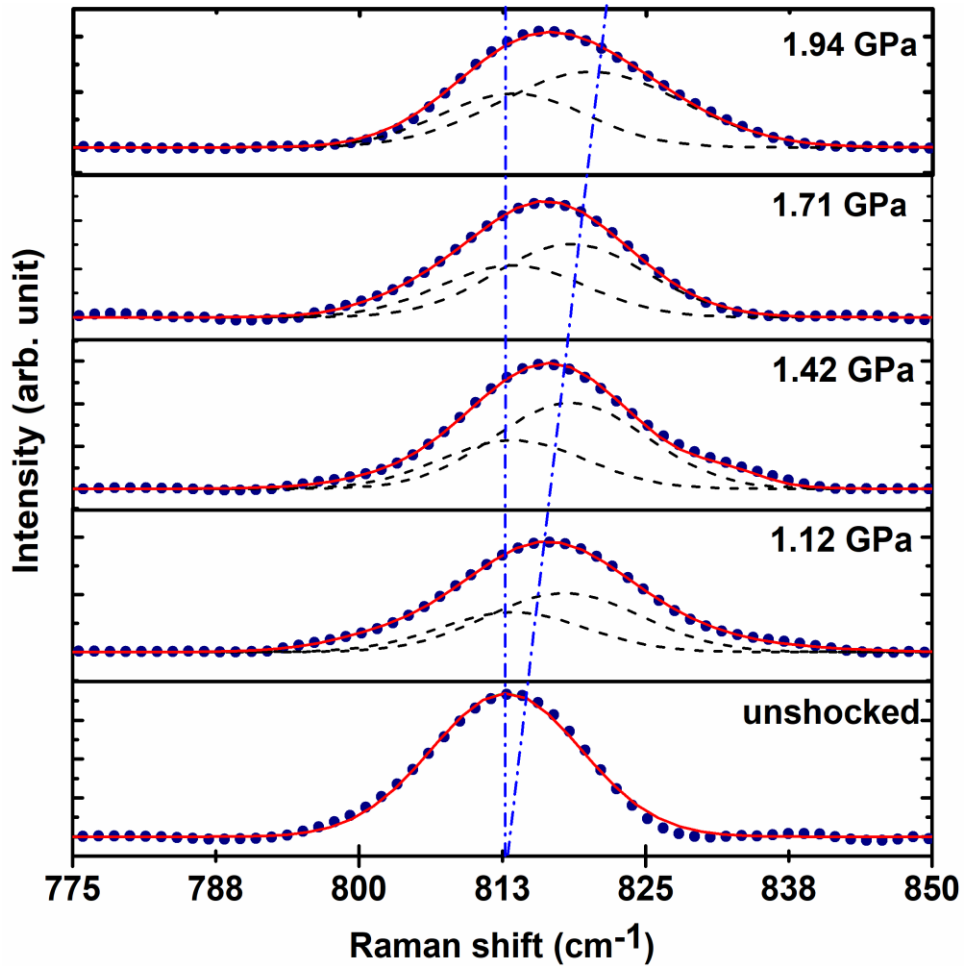


Figure 6. 6. Shows Raman blue shift of  $813\text{ cm}^{-1}$  mode under dynamic shock compression, where the unshocked spectrum is taken as reference for peak shift under shock compression.

The peak position of the amorphous PMMA for several characteristic peaks in order to get a further insight into the pressure dependence of each Raman peak are plotted against pressure in figure 6.7 (a) and (b). Various weak Raman modes in present case are difficult to identify and are smeared out as the pressure increases and hence are not shown in these figure 6.7. The Raman shift increases proportionally with the pressure and the position are fit by linear

least square method to obtain information about sensitivity of particular Raman modes on pressure. From figure 6.7 (a) it can be observed that the carbonyl (C=O) stretching vibrational mode at  $599\text{ cm}^{-1}$  is remarkably sensitive to the pressure with a slope of  $3.09\text{ cm}^{-1}/\text{GPa}$  and other modes at  $813\text{ cm}^{-1}$ ,  $1483\text{ cm}^{-1}$  and  $1728\text{ cm}^{-1}$  also shows a strong dependence on pressure with a slope of  $2.65\text{ cm}^{-1}/\text{GPa}$ ,  $1.6\text{ cm}^{-1}/\text{GPa}$ , and  $2.0\text{ cm}^{-1}/\text{GPa}$  respectively.

### 6.6.3. Bond associated with C–H deformation modes

The observed Raman spectrum also shows a prominent band at  $1453$  (depolarized),  $2846$ ,  $2957\text{ cm}^{-1}$  and assigned as  $\delta_a(\text{C–H})$  of  $\text{O–CH}_3$ , stretching mode of  $\text{C–H}$  respectively. From figure 6.7 (b) it is clear that the  $\text{C–H}$  stretch mode changes slower than the  $\delta_a(\text{C–H})$  mode with pressure. The  $1453\text{ cm}^{-1}$   $\delta_a(\text{C–H})$  of  $\text{O–CH}_3$  bending vibration in PMMA shifts by  $1.6\text{ cm}^{-1}/\text{GPa}$  between  $1.12$  and  $1.94\text{ GPa}$ , while the  $2957\text{ cm}^{-1}$   $\text{C–H}$  stretching combination mode shifts by about  $5.79\text{ cm}^{-1}/\text{GPa}$  under shock compression. The  $2957\text{ cm}^{-1}$  mode shock compression-induced shift is typical of that measured for  $\text{C–H}$  stretching modes in molecules. The vibrational peak shift is close to that of the  $2956\text{ cm}^{-1}$   $\text{C–H}$  stretching mode of poly (butylene adipate) under static pressure, which was measured by Schoonover et al. to increase at a rate of  $6\text{ cm}^{-1}/\text{GPa}$  [167]. In their study of PMMA under static pressure using infrared absorption spectroscopy, Emmons et al. [4] chose four different data sets using different concentrations ranging from  $11\text{--}30\%$ . They have found that the  $2951\text{ cm}^{-1}$   $\text{C–H}$  stretch combination mode shifts by  $6.1\text{ cm}^{-1}/\text{GPa}$ , between  $0$  to  $8\text{ GPa}$  under static pressure. The similar trend we also observed in our static and dynamic compression data. In figure 6.7 (b), combination band involving  $\text{O–CH}_3$  and  $\text{C–H}$  stretching mode of  $\text{O–CH}_3$  at  $2846\text{ cm}^{-1}$  and  $2957\text{ cm}^{-1}$  shows the Raman shift with pressure in both the cases dynamic and static compression.

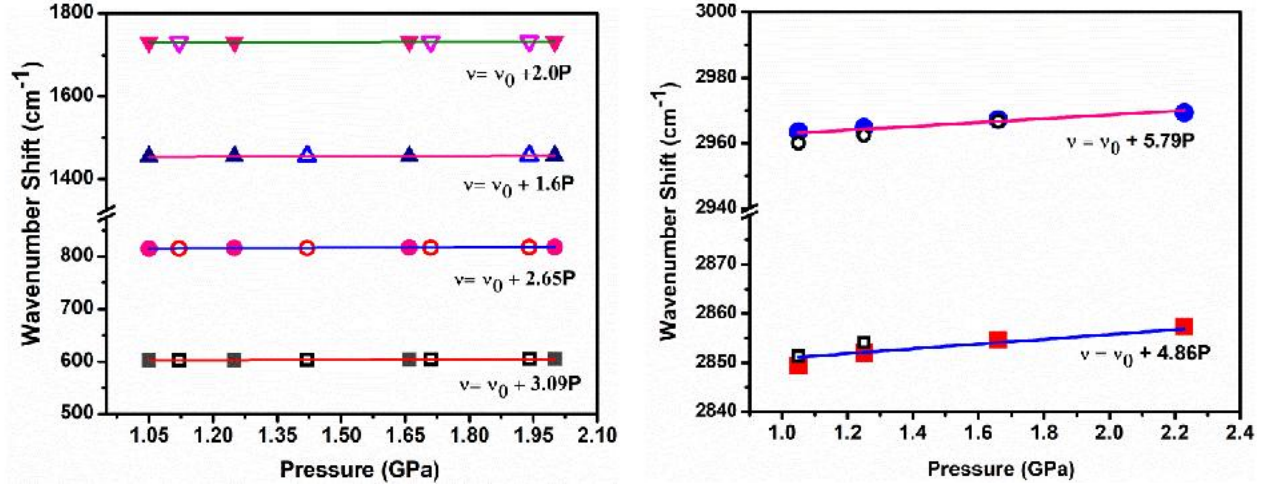


Figure 6. 7. (a) and (b) shows pressure-dependent behaviors of observed Raman modes of PMMA under shock compression. The symbols (open- shock data; filled- static data) show experimental data, and solid lines show the linear fit to the data under static compression [158].

#### 6.6.4. Volume independent Grüneisen Parameter for PMMA

To determine the individual mode Grüneisen parameters, the compression of material as a function of pressure must be known. Bridgman [20] had measured the PV data of PMMA up to 4 GPa. Here, under shock compression the fractional compressibility of PMMA as a function of pressure is determine by performing a 1D numerical simulation. The simulation data below 8 GPa is shown in figure 6.8 and is fitted by a function

$$\frac{V(0)}{V(P)} = \left[ 1 + \frac{P(\text{GPa})}{0.40} \right]^{1/14.20} \quad (6.2)$$

This formula is used here for the compressibility measurements in this study.

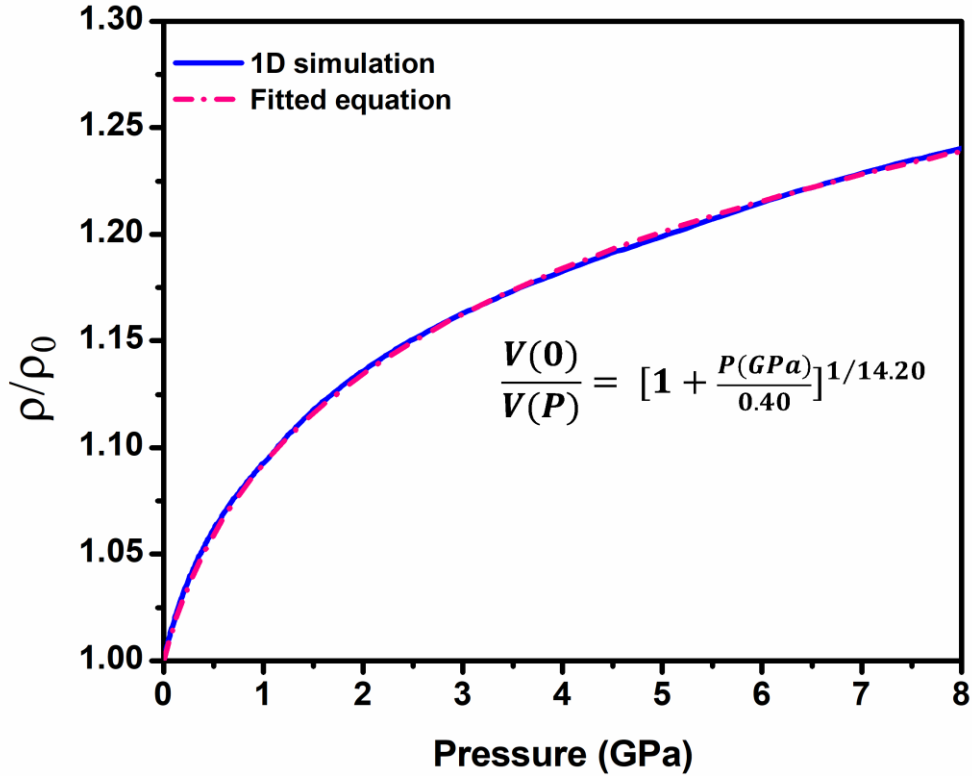


Figure 6. 6. Fractional compressibility ( $\rho/\rho_0$ ) of PMMA for pressures below 8 GPa.

The PMMA data are analyzed using similar techniques as by Flores and Chronister [157] and Dattelbaum et al. [168] to determine the individual mode Grüneisen parameters. Dattelbaum et al. [168] in their technique assumes two different regimes during the compression. During compression under low pressures, the main effect is to decrease the amount of free volume present in the sample. After most of the free volume is removed, compression mainly serves to decrease the distance between the polymer chains. The pressure at which most of the free volume removed is known as the “crush-up” pressure. At pressures measured in the current experiment ( $< 2$  GPa), the compression of the intra-molecular bonds is found quite small. Sherman et al. [109], [124] in his model predicted that if the bond lengths decrease by 1%, for typical potentials the vibrational frequencies will increase by an amount of the order of 10%. For the final pressure of 1.94 GPa for the present experiment, the bond frequencies of PMMA shifted by an amount of

$\sim 0.8\text{--}1.4\%$  from the ambient pressure value. Thus the changes in the bond length are of the order of  $0.08\text{--}0.14\%$ . In contrast, the changes in volume for the corresponding pressure are  $\approx 15\%$ . This indicates that the primarily volume changes ( $< 1\text{GPa}$ ) in polymers are due to free volume and compression of the inter-chain bonds.

The mode independent Grüneisen parameters  $\gamma_i$  are estimated for several Raman active modes of PMMA. A linear fit is used to fit the  $\ln[\nu_i(P)/\nu_i(0)]$  vs  $\ln[V(0)/V(P)]$  data. The plots of the  $\ln[\nu_i(P)/\nu_i(0)]$  vs  $\ln[V(0)/V(P)]$  for several fundamental modes of PMMA are shown in figure 6.9. The slopes in figure 6.9 give the value of mode individual Grüneisen parameters. The magnitude of  $\gamma_i$  for the  $1728\text{ cm}^{-1}$  mode of PMMA ( $\gamma_i = 0.0236 \pm 0.005$ ) is found lower than the other modes. These differences in individual mode Grüneisen parameter's  $\gamma_i$  indicates about anharmonicity in the potential energy surface for the particular vibrational mode or that the local volume compression near that coordinate. All the vibrational modes of PMMA are found to have volume independent Grüneisen parameter  $\gamma_i$  under present experimental pressure range and are found comparable with the earlier reported measurements on various polymers [158].

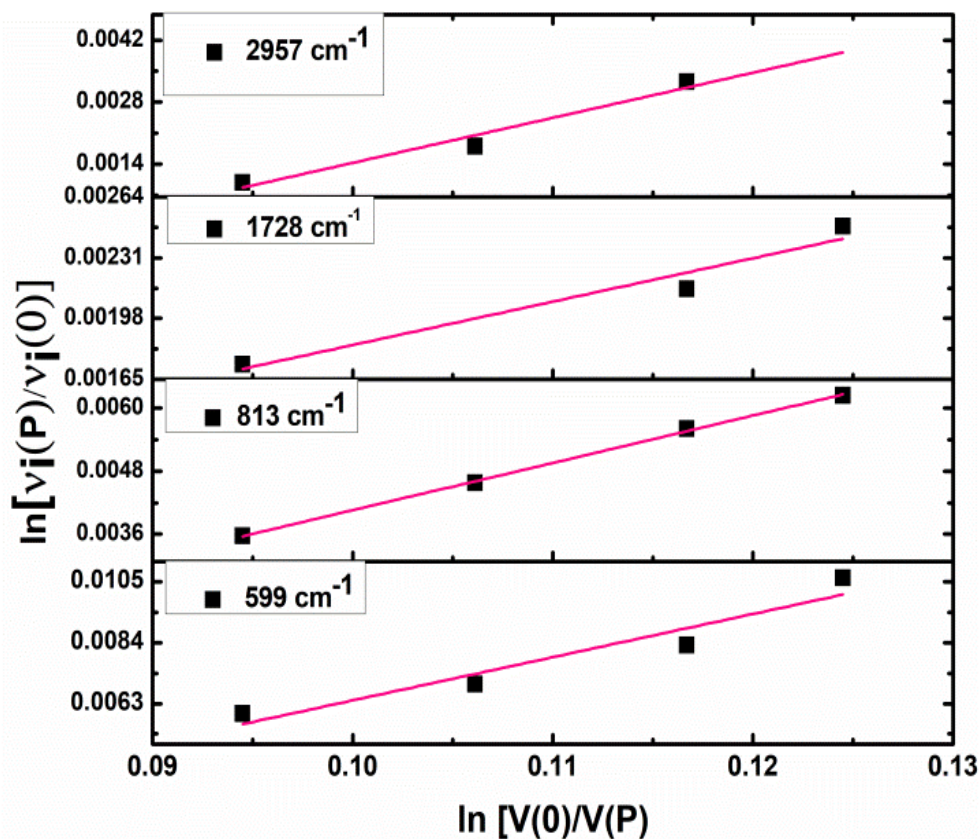


Figure 6. 7. A log-log plot for  $\ln [V(0)/V(P)]$  versus  $\ln [\nu_i(P)/\nu_i(0)]$  for analyzed peaks of PMMA. The solid lines are linear fits to the exact Grüneisen parameters.

### 6.7. Conclusion

The positions of the observed fundamental modes of PMMA are measured as a function of shock pressure. All of the vibrational modes are showing pressure induced broadening and are shifted to higher wavenumber with the pressure. The pressure induced peak shift ( $\nu$ ) for 599, 813, 1453 and 1728  $\text{cm}^{-1}$  Raman modes are found varying linearly with pressure (P) as;  $\nu = 599 + 3.09P$ ,  $\nu = 813 + 2.65P$ ,  $\nu = 1453 + 1.6P$  and  $\nu = 1728 + 2.0P$  respectively. The shift in Raman mode C=O at 1728  $\text{cm}^{-1}$ , is found higher than other modes. The higher shift and mode Grüneisen parameters value for carbonyl group (C=O mode) at 1728  $\text{cm}^{-1}$ , indicates the greater anharmonicity in the potential energy surface of this mode or the local volume

compression near this coordinate is larger than the other modes. The larger shift of C–C–O mode at  $599\text{ cm}^{-1}$  than the C–O–C mode at  $813\text{ cm}^{-1}$ , is because C–O–C mode is of more extended from the polymer backbone relative to C–C–O mode, this suggests that the smaller shift is due to smaller intrinsic anharmonicity for this vibrational mode.

## Chapter 7. Summary and Conclusions

This dissertation describes the development of time resolved Raman spectroscopy experimental facility at Laser Shock Laboratory, BARC to investigate and understand the structural dynamics, physical and chemical properties of different types of polymers under different shock conditions. The three different types of polymers (aromatic scintillating, semi-crystalline and thermoplastic) are studied. These materials differ in their degree of crystallinity, molecular weight, and amount of branching and crosslinking. The time resolved Raman spectroscopy has been used as a main technique to characterize these polymeric systems. These polymers are used in a variety of applications where they experience extreme conditions, such as shock compression experiments, as binders in high explosives, and for manufacturing bullet-proof glass and vests. The results are also compared with other polymers under high pressure and shock compression experiments to see if any general trend can be established.

The thesis consists of seven chapters including this chapter on summary and conclusions of thesis. The chapter 1 gives an introduction to the shock waves, impedance mismatch technique, physical properties of polymers and their fundamental science under extreme conditions. The interest in polymers, their usefulness under extreme conditions and objective of thesis is also discussed in chapter 1. The experimental facilities and techniques used to study the polymers of interest under shock loading are described in chapter 2. The chapter 2 also gives brief description about in-house developed time resolved Raman spectroscopy facility. The chapter 2 starts with a brief description of the nanosecond laser system used in present research work. The characterization of the parameters of the driving laser system namely: pulse duration, spatial spectral and temporal profiles, spectral width of the laser beam, reproducibility or

fluctuation of laser energy with shot numbers etc. are outlined in chapter 2. Most of the work of this thesis is carried out using this in-house developed time resolved Raman spectroscopy facility under extreme conditions. The temporal and spectral resolutions of system in best condition achieved are 1.2 ns and  $3 \text{ cm}^{-1}$  respectively. The experimental arrangement is based on the pump-probe based technique. The pump and probe beams on target and ICCD camera gate pulse are synchronized with the help of delay generator to get optimized signal. The delay between pump and probe beams is generated for more than hundred of nanoseconds, by using two large size mirrors with maximum reflection at zero degree angle of incidence. For best resolution and higher Raman signal, the set up is optimized using  $\text{CCl}_4$ , as the Raman signal from the  $\text{CCl}_4$  is very large. Later,  $\text{CCl}_4$  is replaced by the sample of interest. The experimental description for confinement geometry targets assembly used for the enhancement of shock pressure inside the sample, detection and data acquisition system, static high pressure measurement, experimental arrangement are also explained in detail in chapter 2.

The main results of the thesis are reported in chapter 3 to 6. The laser induced damage mechanism in borosilicate glass (used for making confinement geometry targets), its characterization and dependency on laser parameters is presented in chapter 3. These laser induced damage width, geometries and microstructure changes are analyzed with optical microscope, scanning electron microscope and Raman spectroscopy. The results show that at low laser intensities symmetrical damages are found and these damage width increases nonlinearly with incident laser intensity. The damage threshold energy depends on laser pulse duration as  $t_p^\alpha$ . The value of  $\alpha$  for BK7 glass is estimated as  $\sim 0.2$  and  $\sim 0.3$  for front and rear surface respectively. It is observed that the rear side of the optical glass being used for the confinement of plasma can sustain the threshold fluence of about  $75 \text{ J/cm}^2$  and  $31 \text{ J/cm}^2$  at the fundamental

wavelength for nanosecond and sub–nanosecond laser pulses respectively [66]. Below these laser fluences; laser will interact directly to the Al foil without damaging the optical glass. This Al foil is being used as a shock wave generator. It is found that the samples display higher damage threshold energy when irradiated with long pulse in comparison to short laser pulse. The estimated average temperature and density for nanosecond produced plasma from the optical emission spectrum is around 0.94 eV and  $10^{17} \text{ cm}^{-3}$  [66]. The SEM record of the damage spot due to nanosecond and sub–nanosecond laser pulses shows that in case of long pulse, the tensile stress exceeds the dynamic strength of the material which causes the cracks and fracture. However, for short pulse laser, laser ablation is accompanied by the electron heat conduction and melting processes are dominated. It is observed that for the longer pulse duration, the thermal diffusion length is longer and temperature gradient is also higher which causes larger damage area. The parameters obtained from this experiment are later used to design confinement geometry target assembly for the amplification of shock pressure and duration in laser shock experiments.

The effect of shock wave on molecular structure on different polymers is discussed in chapter 4–6. Chapter 4 describes the Raman spectroscopy analysis for aromatic scintillating polymers (Polystyrene and PVT) that reveals the behavior of these aromatic polymers under shock compression. The Hugoniot relation for Al and polystyrene are taken as  $U_s = 5.16 + 1.25u_p$  and  $U_s = 2.494 + 1.47u_p$  for shock pressure calculations [160]. It is observed that the shock pressure induced shifts of the vibrational modes common to both systems (Polystyrene and PVT) are almost similar. The changes in vibrational frequencies of fundamental Raman peaks ( $\nu_{12}$  and  $\nu_{8a}$  mode) have been observed with respect to shock wave propagation. A maximum vibrational frequency shift caused by shock compression is found to be  $5 \text{ cm}^{-1}$  for polystyrene

$\nu_{12}$  mode. For PVT, all observed modes show a linear relation with static pressure. The relationship between the static pressure induced peak shift ( $\nu$ ) and pressure (P) for 1001, 1031 and 1602  $\text{cm}^{-1}$  modes; are  $\nu = 1001 + 2.33P$ ,  $\nu = 1031 + 3.08P$  and  $\nu = 1602 + 3.94P$  respectively [160]. There is no evidence observed for changes in the slopes of the peak shift–pressure plots [ $d\nu / dP$  ( $\text{cm}^{-1}/\text{GPa}$ )] up to  $\sim 2$  GPa, for PVT and polystyrene under shock compression. This indicates, there are no chemical processes involved for the generation and/or breaking of intra-molecular bonds at present experimental conditions. The 1602  $\text{cm}^{-1}$ ,  $\nu_{8a}$  mode of PVT shifted at an average rate of 3.94  $\text{cm}^{-1}/\text{GPa}$ . This is higher than the shift in the Raman active mode of polystyrene at 1606  $\text{cm}^{-1}$ , which is shifted by an average of 3.50  $\text{cm}^{-1}/\text{GPa}$  over the same pressure range. The slope of the plot defines the extent of the anharmonicity. However, higher energy modes of PVT are showing relatively higher anharmonicity compared to Polystyrene with increase of pressure. For the final pressure of 2.25 GPa for the present experiment, the bond frequencies of PVT shifted by an amount of 0.6% to 0.8% from the ambient pressure value. Thus the changes in the bond length are of the order of 0.06–0.08% [128]. In contrast, the changes in volume for the corresponding pressure are  $\approx 15\%$ . This clearly indicates that the primarily volume changes ( $< 1\text{GPa}$ ) are due to free volume and compression of the inter-chain bonds, and not because of changes in intermolecular bond lengths. The individual mode Grüneisen parameters are calculated for each Raman modes. All the observed results shows both aromatic polymers are stable under shock loading and are reversible up to 2 GPa.

Chapter 5 describes the shock wave induced high pressure and nanosecond time resolved spontaneous Raman spectroscopic studies to examine the dynamic response of fluoro polymer, PTFE. Raman spectra are measured as a function of shock pressure in the 1.2–2.5 GPa range. Furthermore, the vibrational mode at 729  $\text{cm}^{-1}$ , attributed to symmetric stretching mode of  $\text{CF}_2$  is

compared to corresponding static high pressure measurements carried in a diamond anvil cell. Observed changes in  $729\text{ cm}^{-1}$ , Raman spectra line width (FWHM) indicates that the shock pressure gradient is responsible for Raman peak broadening rather than shock induced temperature in PTFE film. A relationship between pressure induced shift ( $\nu\text{ cm}^{-1}$ ) and applied pressure ( $P\text{ GPa}$ ) for static compression is given by the linear equation  $\nu = 5.08P$ . According to this relation, the shift  $12\text{ cm}^{-1}$ ; corresponds to a pressure of  $2.4\text{ GPa}$  inside PTFE, which is in good agreement with pressure values under dynamic compression. By using time evolution of Raman intensity ratios the shock velocity inside PTFE are calculated. At the delay time 38, 52, 60 and 80 ns, the Raman intensity ratios belonging to the shocked area are 0.23, 0.72, 1.04, and 2.2, respectively. According to the above intensity ratio data the fitted value of  $r$  is,  $(0.014 \pm 0.001) \times 10^9\text{ s}^{-1}$ . Hence the approximate shock velocity inside the PTFE calculated to be  $1.68 \pm 0.12\text{ km/s}$  [100]. This is in good agreement with the calculated shock velocity using 1D radiation hydrodynamic simulations.

Chapter 6 describes the in situ spontaneous Raman spectroscopy studies of shock response of thermoplastic polymer, PMMA. The magnitude of shock pressures in PMMA as a function of incident laser intensity is calculated from the Hugoniot of the standard (in this case Al), taking the EOS data from SESAME and QEOS and utilizing the impedance matching technique.

The positions of the observed fundamental modes of PMMA are measured as a function of shock pressure. All of the vibrational modes are showing pressure induced broadening and are shifted to higher wavenumber with the pressure. The pressure induced peak shift ( $\nu$ ) for 599, 813, 1453 and  $1728\text{ cm}^{-1}$  Raman modes are found varying linearly with pressure ( $P$ ) as;  $\nu = 599 + 3.09P$ ,  $\nu = 813 + 2.65P$ ,  $\nu = 1453 + 1.6P$  and  $\nu = 1728 + 2.0P$  respectively. The

shift in Raman mode C=O at  $1728\text{ cm}^{-1}$ , is found higher than other modes. The higher shift for C=O mode at  $1728\text{ cm}^{-1}$ , indicates the greater anharmonicity in the potential energy surface of this mode or the local volume compression near this coordinate is larger than the other modes. The larger shift of C–C–O mode at  $599\text{ cm}^{-1}$  than the C–O–C mode at  $813\text{ cm}^{-1}$ , is because C–O–C mode is of more extended from the polymer backbone relative to C–C–O mode, this suggests that the smaller shift is due to smaller intrinsic anharmonicity for this vibrational mode. Observed peak shift and line width data are used to determine mode Grüneisen parameters and bond anharmonicities [171]. These shock compressed states are also compared with the static compression data, to see if any general trend can be established.

To conclude, this thesis presents a study of different polymeric materials in confinement geometry target assembly using in-house developed time resolved Raman spectroscopy under laser-driven shock compression. Three different types of polymers are studied. These polymers differ in their weight, degree of crystallinity, and amount of branching and cross-linking. Several different aspects of polymer physics are examined by performing studies under shock loading. Vibrational spectroscopy under shock compressions reveals the effects of extreme conditions at the level of chemical bonds. How the vibrational modes shift with shock pressure reveals information about the anharmonicity of the intra-molecular potentials. When combined with an equation of state, individual mode Grüneisen parameters are obtained. In addition to obtaining information about the molecular bonds, information about the arrangement of the polymer chains can also be obtained. In amorphous polymers, compression of the material removes void space in the polymer. In semi-crystalline polymers, compression may lead to changes in chain conformations and the lattice structure. Information such as this on the molecular level is related to the macroscopic mechanical and thermodynamic properties. The

time resolved Raman spectroscopy shows signatures of these phase transitions and shows its importance under shock loading for such studies.

### **7.1. Future Directions**

The study of polymers under dynamic shock loading is a field that is still only in its early years. Systematic studies of additional polymers under shock loading would be valuable. Polymers also have never been subjected to the ultra-high pressures. Under ultra high pressures, the covalent bonds within a chain molecule are compressed to a significant extent. This may lead to interesting chemical and structural effects. Experiments in such an unexplored regime may reveal new behavior. Use of other experimental techniques would be valuable as well. The x-ray diffraction studies of polymers under dynamic shock loading are also very valuable for obtaining equation-of-state and phase transition information. As phase transitions in polymers have also received very little attention. A systematic study of different semi-crystalline polymers would definitely be of importance. The studies will also be very interesting in terms of kinetic effects in high pressure transformations. It has been shown recently that the pressure increasing rate can have a pronounced effect on the phases formed in the course of pressure induced phase transitions in some organic crystals. So, it would be interesting to study the effect of dynamic compression on the organic crystals.

Overall, the behavior of polymers under shock compression has been experiencing an increased level of interest in recent years, especially due to technical applications where polymers experience extreme conditions, such as during high amplitude shock compression. Since till date so little work in this area has been performed, much fruitful results remains to be discovered. In this regard, it will be important to relate the microscopic and macroscopic properties of the polymers under shock loading would also be valuable in polymer science.



## References

- [1] G. I. Pangilinan and Y. M. Gupta, *J. Appl. Phys.*, vol. 81, no. 10, p. 6662, 1997.
- [2] T. Kobayashi and T. Sekine, *Phys. Rev. B*, vol. 62, no. 9, pp. 5281–5284, 2000.
- [3] M. A. Xue, J. H. Wu, S. Ye, D. Hu, X. D. Yang, Y. P. Wang, W. J. Zhu, and C. B. Li, *J. Phys. D: Appl. Phys.*, vol. 41, p. 45501, 2008.
- [4] N. C. Holmes and R. Chau, *J. Chem. Phys.*, vol. 119, p. 3316, 2003.
- [5] D. Chelazzi, M. Ceppatelli, M. Santoro, R. Bini, and V. Schettino, *Nat. Mater.*, vol. 3, pp. 470–5, 2004.
- [6] C. Murli and Y. Song, *J. Phys. Chem. B*, vol. 114, pp. 9744–9750, 2010.
- [7] W. M. Trott and A. M. Renlund, *Appl. Opt.*, vol. 24, p. 1520, 1985.
- [8] P. Hebert, V. Bouyer, M. Doucet, J. Rideau, and L. P. Terzulli, *AIP Conference Proceedings*, 2012, vol. 1426, pp. 1585–1588.
- [9] D. E. Hare, J. Franken, D. D. Dlott, E. L. Chronister, and J. J. Flores, *Appl. Phys. Lett.*, vol. 65, p. 3051, Dec. 1994.
- [10] D. D. Dlott and M. D. Fayer, *J. Chem. Phys.*, vol. 92, p. 3798, 1990.
- [11] X. Zheng, A. D. Curtis, W. L. Shaw, and D. D. Dlott, *J. Phys. Chem. C*, vol. 117, pp. 4866–4875, 2013.
- [12] G. Tas, J. Franken, S. Hambir, D. Hare, and D. Dlott, *Phys. Rev. Lett.*, vol. 78, pp. 4585–4588, 1997.
- [13] D. E. Hare, J. Franken, D. D. Dlott, E. L. Chronister, and J. J. Flores, *Appl. Phys. Lett.*, vol. 65, pp. 3051–3053, 1994.
- [14] K. G. Nakamura, *AIP Conf. Proc.*, vol. 620, pp. 1259–1262, 2002.
- [15] K. Wakabayashi, K. G. Nakamura, K. Kondo, and M. Yoshida, *Appl. Phys. Lett.*, vol. 75,

- p. 947, 1999.
- [16] R. G. Kraus, E. D. Emmons, J. S. Thompson, and A. M. Covington, *J. Polym. Sci. Part B Polym. Phys.*, vol. 46, pp. 734–742, 2008.
- [17] E. D. Emmons, R. G. Kraus, S. S. Duvvuri, J. S. Thompson, and A. M. Covington, *J. Polym. Sci. Part B Polym. Phys.*, vol. 45, pp. 358–367, 2007.
- [18] G. Saini, Spectroscopic Observation of Materials under Dynamic Conditions, *PhD thesis, MIT, September 2010*.
- [19] J. W. Forbes, Shock wave compression of condensed matter : a primer, *Springer, 2012*.
- [20] D. D. Dlott, *Annu. Rev. Phys. Chem.*, vol. 50, pp. 251–278, 1999.
- [21] S. Gallivan and Y. Gupta, *J. Appl. Phys.*, vol. 78, pp. 1557, 1995.
- [22] A. Matsuda, K. Nakamura, and K. Kondo, *Phys. Rev. B*, vol. 65, pp. 174116, 2002.
- [23] K. G. Nakamura, *AIP Conference Proceedings*, vol. 620, pp. 1259–1262, 2002.
- [24] G. Tas, S. Hambir, J. Franken, and D. Hare, “Coherent Raman spectroscopy of nanoshocks,” *J. Appl.*, vol. 82, pp. 1080, 1997.
- [25] A. Lagutchev, J. Patterson, and W. Huang, *J. Phys.*, vol. 105, pp. 5033, 2005.
- [26] J. Franken, S. Hambir, and D. Dlott, *J. Appl. Phys.*, vol. 85, pp. 2068, 1999.
- [27] S. P. Marsh, *LASL shock hugoniot data*. University of California Press, 1980.
- [28] D. I. Bower and W. F. Maddams, *The vibrational spectroscopy of polymers. Cambridge University Press, 1992*.
- [29] A. L. Kovarskiĭ, *High-pressure chemistry and physics of polymers*. CRC Press, 1994.
- [30] J. Cowie and V. Arrighi, *Polymers: chemistry and physics of modern materials*. 2007.
- [31] D. Bower and W. Maddams, *The vibrational spectroscopy of polymers*. 1992.
- [32] B. Wunderlich, *Macromolecular physics*. vol. 2, 2012.

- [33] H. Tadokoro, *Structure of Crystalline Polymers*. New York: Wiley, 1979.
- [34] W. Perger, S. Vutukuri, Z. Dreger, and Y. Gupta, *Chem. Phys.*, vol. 422, pp. 397, 2006.
- [35] E. D. Emmons, *Vibrational Spectroscopy of Polymers at High Pressure*, PhD Thesis, University of Nevada, Reno, 2007.
- [36] L. H. Sperling, *Introduction to Physical Polymer Science*, 4th ed. Wiley, Hoboken, New Jersey, 2006.
- [37] A. F. Goncharov, *Int. J. Spectrosc.*, vol. 2012, pp. 1–16, 2012.
- [38] K. Nagayama and Y. Mori, *J. Appl. Phys.*, vol. 84, p. 6592, 1998.
- [39] Y. Song, X. Zheng, G. Yu, J. Zhao, L. Jiang, Y. Liu, and Y. Yang, vol. 2010, 2010, pp. 345–348, 2011.
- [40] L. Zhao, B. J. Baer, and E. L. Chronister, *J. Phys. Chem. A*, vol. 103, pp. 1728–1733, 1999.
- [41] *The Raman Effect: A Unified Treatment of the Theory of Raman Scattering by Molecules*, By D. A. Long, John Wiley & Sons Ltd., 2002.
- [42] H. Kuzmany, *Solid-State Spectrosc. An Introd.*, Springer, 2009.
- [43] S. Chaurasia, V. Rastogi, U. Rao, C. D. Sijoy, V. Mishra and M. N. Deo, *Journal of Instrumentation*, 12(11), P11008, 2017.
- [44] N. C. Anderholm, *Appl. Phys. Lett.*, vol. 16, p. 113, 1970.
- [45] D. Devaux, R. Fabbro, L. Tollier, and E. Bartnicki, *J. Appl. Phys.*, vol. 74, pp. 2268–2273, 1993.
- [46] R. Fabbro, P. Peyre, L. Berthe, and X. Scherpereel, vol. 10, 1998.
- [47] V. Rastogi, S. Chaurasia, and U. Rao, *J. Raman*, vol. 48, pp. 458-464, 2017.
- [48] V. Rastogi, U. Rao, S. Chaurasia, and A. Mishra, *AIP Conf.*, 1731, 2016.

- [49] T. Chakraborty and A. . Verma, *Spectrochim. Acta Part A Mol. Biomol. Spectrosc.*, vol. 58, pp. 1013–1023, 2002.
- [50] P. McMillan, *Am. Mineral.*, vol. 69, pp. 622–644, 1984.
- [51] N. Bloembergen, *IEEE J. Quantum Electron.*, vol. 10, pp. 375–386, 1974.
- [52] C. Carr, H. Radousky, and S. Demos, *Phys. Rev. Lett.*, vol. 91, p. 127402, 2003.
- [53] R. R. Gattass and E. Mazur, *Nat. Photonics*, vol. 2, pp. 219–225, 2008.
- [54] Z. Xia, D. Li, Y. Zhao, and Y. Wu, *Opt. Laser Technol.*, vol. 46, pp. 77–80, 2013.
- [55] K. Sugioka and Y. Cheng, *Light Sci. Appl.*, vol. 3, p. e149, 2014.
- [56] D.W. Bäuerle, *Laser processing and chemistry*, Springer, 2011.
- [57] L. D. Merkle, N. Koumvakalis, and M. Bass, *J. Appl. Phys.*, vol. 55, p. 772, 1984.
- [58] C. Carr, H. Radousky, and S. Demos, *Phys. Rev. Lett.*, vol. 91, 127402, 2003.
- [59] <http://nvlpubs.nist.gov/nistpubs/Legacy/SP/nbsspecialpublication746.pdf>.
- [60] J. Chan, T. Huser, S. Risbud and D. M. Krol, *Optics Letters*, vol. 26, 1726-1728, 2001.
- [61] Y. T. Chen, K. J. Ma, A. A. Tseng and P. H. Chen, *Opt. Laser Technol.*, vol. 37, pp. 271–280, 2005.
- [62] Maini, *Lasers and Optoelectronics: Fundamentals, Devices and Applications*. John Wiley & Sons, 2013.
- [63] M. C. Downer, R. L. Fork, and C. V. Shank, *J. Opt. Soc. Am. B*, vol. 2, p. 595, 1985.
- [64] A. C. Tam, J. L. Brand, D. C. Cheng, and W. Zapka, *Appl. Phys. Lett.*, vol. 55, p. 2045, 1989.
- [65] M. R. Kasaai, V. Kacham, F. Theberge, and S. L. Chin, *J. Non. Cryst. Solids*, vol. 319, pp. 129–135, 2003.
- [66] V. Rastogi, S. Chaurasia, and D. S. Munda, *J. Non. Cryst. Solids*, vol. 463, pp. 138–147,

- 2017.
- [67] R. Uyak, An investigation of laser induced surface damage in glass. *Diss.* 1985.
- [68] S. N. Luo, D. C. Swift, T. E. Tierney, D. L. Paisley, G. A. Kyrala, R. P. Johnson, A. A. Hauer, O. Tschauner, and P. D. Asimow, *High Press. Res.*, vol. 24, pp. 409–422, 2004.
- [69] K. Yoshida, M. Yamanaka, M. Nakatsuka, T. Sasaki, and S. Nakai, *Laser-Induced Damage in Optical Materials*: pp. 2–10, 1997.
- [70] M. Koldunov, A. Manenkov, and I. Pokotilo, *Quantum Electron.*, vol. 32, pp. 335, 2002.
- [71] M. Koldunov, A. Manenkov, and I. Pokotilo, *Quantum Electron.*, ol. 32, pp. 335, 2002.
- [72] L. Zhigilei and B. Garrison, *Laser-tissue*, vol. 3254, pp. 135, 1998.
- [73] I. Mirza, N. Bulgakova, J. Tomáščík, and V. Michálek, *Scientific report*, vol. 6, pp. 39133, 2016.
- [74] L. Merkle and D. Kitriotis, *Phys. Rev. B*, vol. 38, pp. 1473, 1988.
- [75] J. L. Brand and A. C. Tam, “*Appl. Phys. Lett.*”, vol. 56, p. 883, 1990.
- [76] D. Manara, A. Grandjean, and D. R. Neuville, *J. Non. Cryst. Solids*, vol. 355, pp. 2528–2531, 2009.
- [77] D. J. Little, M. Ams, S. Gross, P. Dekker, C. T. Miese, A. Fuerbach, and M. J. Withford, *J. Raman Spectrosc.*, vol. 42, pp. 715–718, 2011.
- [78] Q. Liu, B. F. Johnston, S. Gross, M. J. Withford, and M. J. Steel, *Opt. Mater. Express*, vol. 3, p. 2096, 2013.
- [79] H. R. Griem, “*Plasma Spectroscopy*,” vol. 35, pp. 34–130, 1966.
- [80] A. M. El Sherbini, *World J. Nano Sci. Eng.*, vol. 2, pp. 206–212, 2012.
- [81] D. Nishijima and R. Doerner, *J. Phys. D. Appl. Phys.*, vol. 48, 325201, 2015.
- [82] T. Labutin, S. Zaytsev, and A. Popov, *Anal. Chem.*, vol. 85, pp. 1985, 2013.

- [83] I. Gornushkin, A. Kazakov, and N. Omenetto, *Acta Part B At.* vol. 60, pp. 215, 2005.
- [84] H. Kusch and K. Schröder, *Astron. Astrophys.*, vol. 116, pp. 255, 1982.
- [85] C. Parigger, D. Surmick, and G. Gautam, *Opt. Lett.*, vol. 40, pp. 3436, 2015.
- [86] A. El Sherbini and A. Al Aamer, *World J. Nano Sci.*, vol. 2, pp. 206, 2012.
- [87] V. González and J. Aparicio, *Astron.*, vol. 363, pp. 1177, 2000.
- [88] <https://www.nist.gov/pml/atomic-spectra-database>.
- [89] M. Capitelli, A. Casavola, G. Colonna, and A. De Giacomo, *Spectrochim. Acta Part B At. Spectrosc.*, vol. 59, pp. 271–289, 2004.
- [90] N. Konjević and M. Dimitrijević, *Chem. Ref. data*, 1984.
- [91] M. Dimitrijević and S. Sahal–Bréchet, *Astron. Astrophys.*, vol. 140, pp. 193-196, 1999.
- [92] D. Cremers and L. J. Radziemski, *Handbook of Laser-Induced Breakdown Spectroscopy*, John Willey & Sons, 2006.
- [93] M. Milan and J. Laserna, *Spectrochim. Acta Part B At. Spectrosc.*, vol. 56, pp. 275-288, 2001.
- [94] V. Natta, F. Danusso, and G. Moraglio, *Die Makromol.*, vol. 28, p. 166, 1958.
- [95] W. M. Sears, *J. Chem. Phys.*, vol. 75, p. 1589, 1981.
- [96] P. C. Painter and J. L. Koenig, *J. Polym. Sci. Polym. Phys. Ed.*, vol. 15, pp. 1885–1903, 1977.
- [97] G. Guerra and V. Vitagliano, *Polymer*, 33, 1423-1428, 1992.
- [98] W. M. Sears, *J. Chem. Phys.*, vol. 77, p. 1639, 1982.
- [99] V. Rastogi, S. Chaurasia, U. Rao, C. D. Sijoy, H. K. Poswal, V. Mishra, M. Kumar, and M. N. Deo, *Raman Spectrosc.*, vol. 48, pp. 1300-1306, 2017.
- [100] V. Rastogi, U. Rao, S. Chaurasia, C. D. Sijoy, V. Mishra, S. Chaturvedi, and M. N. .

- Deo, *J. Raman Spect.* vol 48, 1007-1012, 2017.
- [101] M. Alger, *Polymer Science Dictionary*, vol. 290, pp. 265, 1997.
- [102] S. Marsh, *LASL shock Hugoniot data*. 1980.
- [103] N. Ozaki et al. *Physics of plasmas* vol. 12, 124503, 2005.
- [104] J. P. Romain et al. *Journal of Physics: Condensed Matter* vol. 14, 10793, 2002.
- [105] C. D. Sijoy and S. Chaturvedi, *Comput. Phys. Commun.*, vol. 190, pp. 98–119, 2015.
- [106] J. Curro, *J. Chem. Phys.*, vol. 58, pp 74, 1973.
- [107] T. Barron, *Ann. Phys.* vol. 1, pp. 77, 1957.
- [108] R. B. Jr, *J. Appl. Phys.*, vol. 38, pp. 4234, 1967.
- [109] W. F. Sherman, *J. Phys. C Solid State Phys.*, vol. 15, pp. 9–23, 1982.
- [110] A. Tokmakoff, M. Fayer, and D. Dlott, *J. Phys. Chem.*, vol 97, pp. 1901-1913, 1993.
- [111] J. Flores and E. Chronister, *J. Raman Spectrosc.*, vol. 27, pp. 149-153, 1996.
- [112] K. Nagayama, *AIP Conference Proceedings*, vol. 309, pp. 49–52, 1994.
- [113] J. R. Anema, A. G. Brolo, A. Felten, and C. Bittencourt, *J. Raman Spectrosc.*, vol. 41 pp. 745–751, 2010.
- [114] P. P. Hong, F. J. Boerio, S. J. Clarson, and S. D. Smith, *Macromolecules*, vol. 24, pp. 4770–4776, 1991.
- [115] B. Jasse, R. S. Chao, and J. L. Koenig, *J. Polym. Sci. Polym. Phys. Ed.*, vol. 16, pp. 2157–2169, 1978.
- [116] E. Kellar, C. Galiotis, and E. Andrews, *Macromolecules*, vol, 29, pp. 3515-3520, 1996.
- [117] R. A. Nyquist, C. L. Putzig, M. A. Leugers, R. D. McLachlan, and B. Thill, *Appl. Spectrosc.*, vol. 46, pp. 981–987, 1992.
- [118] Y. Furushima, K. Tazaki, and H. Fujimoto, *Solid State Commun.*, vol. 140, pp. 240–244,

2006.

- [119] A. R. Katritzky, *Quart. Rev.*, vol. 13, p. 353, 1956.
- [120] C. Liang and S. Krimm, *J. Polym. Sci. Part A*, vol. 27, p. 241, 1958.
- [121] A. Katritzky, *Q. Rev. Chem. Soc.*, vol. 13, p. 353, 1959.
- [122] *LASL Shock Hugoniot Data*. Uni. California Press, 1980.
- [123] P. W. Bridgman, *Proc. Am. Acad. Arts Sci.*, vol. 76, p. 71 1948.
- [124] W. F. Sherman, *J. Phys. C Solid State Phys.*, vol. 13, pp. 4601–4613, 1980.
- [125] D. M. Dattelbaum, J. D. Jensen, A. M. Schwendt, E. M. Kober, M. W. Lewis, and R. Menikoff, “*J. Chem. Phys.*”, vol. 122, p. 144903, 2005.
- [126] X. Zheng, Y. Song, J. Zhao, D. Tan, Y. Yang, and C. Liu, *Chem. Phys. Lett.*, vol. 499, pp. 231–235, 2010.
- [127] X. Zheng, Y. Song, J. Zhao, D. Tan, Y. Yang, and C. Liu, *Chem. Phys. Lett.*, vol. 499, pp. 231–235, 2010.
- [128] V. Rastogi, S. Chaurasia, U. Rao, C. D. Sijoy, H. K. Poswal, V. Mishra, M. Kumar, and M. N. Deo, *J. Raman Spectrosc.*, vol. 48, pp. 1300-1306, 2017.
- [129] X. Zheng, A. Curtis, and W. Shaw, *J. Phys.*, vol. 117, p. 4866, 2013.
- [130] M. F. Nicol, J. M. Wiget, and C. K. Wu, *J. Polym. Sci. Polym. Phys. Ed.*, vol. 18, pp. 1087–1102, 1980.
- [131] J. M. G. Cowie, *Polymers: Chemistry and Physics of Modern Materials*, 2nd ed. Chapman & Hall, New York, 1991.
- [132] J. Schiers, Ed., *Modern Fluoropolymers*. Chichester, England: Wiley, 1997.
- [133] J. F. Rabolt, G. Piermarini, and S. Block, *J. Chem. Phys.*, vol. 69, p. 2872, 1978.
- [134] H. Nagao, a Matsuda, K. G. Nakamura, and K. Kondo, “*Appl. Phys. Lett.*”, vol. 83, p. 249,

2003.

- [135] M. F. Nicol, J. M. Wiget, and C. K. Wu, vol. 18, pp. 1087–1102, 1980.
- [136] C. K. Wu and M. Nicol, *Chem. Phys. Lett.*, vol. 21, pp. 153–157, 1973.
- [137] E. Brown et al. *Shock compression of condensed matter*, vol. 47, pp. 7506-7518, 2006.
- [138] D. L. Robbins, *AIP Conference Proceedings*, vol. 706, pp. 675–678, 2004.
- [139] P. J. Rae and D. M. Dattelbaum, vol. 45, pp. 7615–7625, 2004.
- [140] C. Weir, *J. Res. Natl. Bur.*, vol. 50, p. 95, 1953.
- [141] R. Beecroft and C. Swenson, *J. Appl. Phys.*, vol. 30, p. 1753, 1959.
- [142] H. Flack, *J. Polym. Sci. Part B Polym. Phys.*, vol. 10, p. 1799, 1972.
- [143] C. Wu and M. Nicol, *Chem. Phys. Lett.*, vol. 21, p. 153, 1973.
- [144] R. Brown, *J. Chem. Phys.*, vol. 44, p. 2900, 1964.
- [145] M. Nicol, J. Wiget, and C. Wu, *J. Polym. Sci. Part B*, vol. 18, pp. 1087-1102, 1980.
- [146] A. Champion, *J. Appl. Phys.*, vol. 42, p. 5546, 1971.
- [147] A. Champion, *J. Appl. Phys.*, vol. 43, p. 2216, 1972.
- [148] R. R. Alcon, D. L. Robbins, S. A. Sheffield, D. B. Stahl, J. N. Fritz, “Proceedings of the Conference of the American Physical Society Topical Group on Shock Compression of Condensed Matter,” 2003.
- [149] V. Rastogi, U. Rao, S. Chaurasia, C. D. Sijoy, V. Mishra, S. Chaturvedi, and M. N. Deo, *Appl. Spectrosc.*, p. 370281772654, 2017.
- [150] J. L. Koenig, *J. Chem. Phys.*, vol. 50, p. 2823, 1969.
- [151] D. Hare and D. Dlott, *Appl. Phys. Lett.*, vol. 64, p. 715, 1994.
- [152] D. Hare, J. Franken, and D. Dlott, *J. Appl. Phys.*, vol. 77, p. 5950, 1995.
- [153] D. Hare, J. Franken, D. Dlott, and E. Chronister, *Appl. Phys.*, vol. 65, p. 3051, 1994.

- [154] D. C. Swift, et al. *Review of scientific instruments* 76, 093907, 2005.
- [155] D. Moore and S. McGrane, *J. Mol. Struct.*, vol. 561, p. 661, 2003.
- [156] P. Bridgman, *Proc. Am. Acad. Arts & Sci.*, vol. 76, 1948.
- [157] J. Flores and E. Chronister, *J. Raman Spectrosc.*, vol. 27, pp. 149-153, 1996.
- [158] E. Emmons, *Vibrational spectroscopy of polymers at high pressure*. PhD thesis, 2007.
- [159] V. Skorodumov and Y. Godovskii, *Polym. Sci. U.S.S.R.*, vol. 29, pp. 127–133, 1987.
- [160] V. Rastogi et al. *J. Raman Spectrosc.*, vol. 48, pp. 1007–1012, 2017.
- [161] B. Schneider, J. Štokr, P. Schmidt, M. Mihailov, and S. Dirlikov, *Polymer* 20, 705-712, 2005.
- [162] S. Dirlikov and J. Koenig, *Applied Spectroscopy* 33, 555-561, 1979.
- [163] G. Herzberg, *Molecular Spectra and Molecular Structure II. Infrared and Raman Spectra of Polyatomic Molecules*. D. Van Nostrand, New York, 1945.
- [164] B. Wunderlich, *Macromolecular Physics*. Academic Press, New York, 1973.
- [165] H. . Willis, V. J. . Zichy, and P. . Hendra, vol. 10, pp. 737–746, 1969.
- [166] J. J. Flores and E. L. Chronister, vol. 27, pp. 149–153, 1996.
- [167] J. R. Schoonover et al. *Spectrochimica Acta A Mol. Biomol. Spectro.*, vol. 59, pp. 309–319, 2003.
- [168] D. M. Dattelbaum et al. *Journal of chemical physics*, 122, 144903, 2005.
- [169] V. Rastogi, S. Chaurasia, Usha rao, C. D. Sijoy, V. Mishra and M. N. Deo, “Raman Spectroscopy of Poly (Methyl Methacrylate) under laser shock compression,” *Under Prep.*